Title
METASTABILITY AND CRYSTALLIZATION STUDIES IN THE SILICA-ALUMINA SYSTEM

Author
Risbud, Subhash Hanamant.

Publication Date
1976-08-01

LBL-5453

METASTABILITY AND CRYSTALLIZATION STUDIES IN THE SILICA-ALUMINA SYSTEM

Subhash Hanamant Risbud
(Ph. D. thesis)

August 1976

Prepared for the U. S. Energy Research and
Development Administration under Contract W-7405-ENG-48

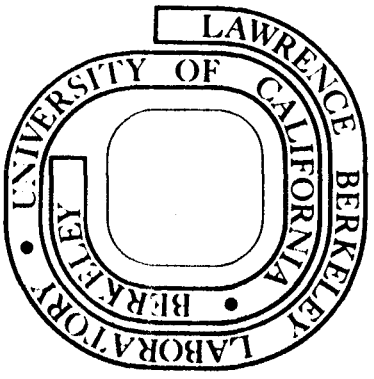

LBL-5453

DISCLAIMER

METASTABILITY AND CRYSTALLIZATION STUDIES IN THE SILICA ALUMINA SYSTEM

Contents

METASTABILITY AND CRYSTALLIZATION STUDIES IN THE SILICA-ALUMINA SYSTEM

Subhash Hanamant Risbud

Materials and Molecular Research Division, Lawrence Berkeley Laboratory
and Department of Materials Science and Engineering,
University of California, Berkeley, California 94720

ABSTRACT

Thermodynamic data on activities, activity coefficients and free energies of mixing in SiO_2-Al_2O_3 solutions was calculated from the phase diagram using regular solution approximations. The calculated data were used to estimate regions of liquid-liquid immiscibility. A metastable liquid miscibility gap with a consolute temperature of ≈1540°C at a critical composition of ≈36 mole% Al_2O_3 was calculated; the gap extended from ≈6.25 to 57 mole% Al_2O_3 at a temperature of ≈800°C.

SiO_2-rich glass compositions were prepared and examined for liquid phase separation by direct transmission electron microscopy. Glass-in-glass immiscibility was realizable in glasses between ≈7.5 and 20 mole% Al_2O_3 but compositions greater than ≈25 mole% Al_2O_3 crystallized very rapidly. The marked positive deviations from ideal mixing in the thermodynamic data calculated from the phase diagram, suggest a tendency for liquid immiscibility in both SiO_2-rich and Al_2O_3-rich compositions.

Crystallization studies were conducted on several selected SiO_2-Al_2O_3 compositions. Melts homogenized at 2090°C (±10°C) were subjected to carefully controlled nucleation and crystallization heat treatments in sealed molybdenum crucibles. Analysis of the microstructures of the crystallized melts by electron beam microprobe and interference contrast microscopy provided data on the morphology, size, and chemical

composition of the phases. Changes in phase compositions with the temperature of heat treatment enabled an estimation of the temperature at which crystallization of the melt commences. The crystallization behavior of the melt is related to prior liquid immiscibility and provided experimental evidence for the calculated phase boundary of the proposed miscibility gap.

Subliquidus reactions in pressed mixtures of SiO_2-Al_2O_3 and cristobalite-corundum were also studied to verify stable and metastable equilibria. Formation of mullite with two different compositions was realized in a single mixture. Mullite with a composition of ≈70.6 wt% Al_2O_3 grew at the firing temperature of 1700°C by solid state reaction between SiO_2 and Al_2O_3. Mullite needles with a higher Al_2O_3 content grew in the same mixture during cooling to room temperature. A metastable SiO_2-Al_2O_3 phase diagram in the absence of mullite obtained by extensions of the SiO_2 and Al_2O_3 liquidi to lower temperatures was proposed to account for formation of glassy phases in subsolidus cristobalite-corundum reactions.

strong tendency for phase separation in the composition range ~10 to 68 wt% (~7 to 55 mol%) Al_2O_3. The temperatures at which this phase separation occurred was not clear from the reported data but a miscibility gap was proposed with an upper consolute temperature of ~1650°C at a critical composition between ~38 to 42 wt% (~25 to 30 mol%) Al_2O_3. Takamori and Roy[16] considered the evidence in favor of the proposed miscibility gap to be inadequate in light of their DTA and TEM observations on splat cooled SiO_2-Al_2O_3 glasses in the composition range (~20 to 95 mol%) Al_2O_3. No evidence for the location of the miscibility gap could be found in their data.

The experimental difficulties in delineating immiscibility regions in the present system are understandable in view of the problems associated with rapid quenching of melts from high temperatures (~2000°C) and also because of the tendency of compositions greater than ~30 mole% Al_2O_3 to crystallize readily.[15]

Being mindful of the experimental problems of assessing immiscibility, an approach utilizing solution thermodynamics has been used in a part of the present work to calculate departures from ideal solution behavior to estimate the approximate composition ranges where immiscibility can be expected to occur. The latter part of this work deals with experimental verification of the calculated immiscibility in high-silica glasses, the influence of the immiscibility dome on crystallization of selected melts, and subliquidus reactions in the SiO_2-Al_2O_3 system.

II. THEORETICAL BACKGROUND

A. Metastable Phases

The move of a materials systems towards it thermodynamically stable equilibrium configuration is often halted for kinetic reasons resulting in a phase assemblage which represents a metastable state. As illustrated schematically in Fig. 2, the metastable phase has a higher free energy content and, given appropriate conditions, would transform to a phase mixture which minimizes the total free energy of the system.

The phase diagrams for most materials attempt to indicate the locations of stable equilibrium boundaries and do not, in general, include data on metastable equilibria. In many situations, especially those involving glass-ceramic materials, kinetic inaccessibility of stable phases makes metastability readily realizable under normal experimental conditions. In recent times the advent of ultra-fast quenching techniques has also given rise to a harvest of metastable phases even in metallic alloys.[17] An understanding of metastable phase diagrams is, therefore, both of theoretical and practical utility.

Consider the relationship of the free energy versus composition diagram and the hypothetical equilibrium diagram as shown in Fig. 3. As illustrated by drawing common tangents to the free energy curves, phases α and β are stable for compositions of component B less than C_1 and greater than C_2 respectively. In the composition range between C_1 and C_2 a mixture of and phases is stable. If we now consider the cooling of a mixture of eutectic composition C_e, a structure consisting of α and β phases formed by nucleation and growth can be expected at a

slow enough cooling rate. Just below the eutectic temperature T_e, this transformation will be limited by an inadequate driving force and at much lower temperatures by low mobility of the diffusing species. Consequently, in some intermediate temperature range the phase transformation will occur at a maximum rate. If in this temperature range the phases β_1 or β_2 (Fig. 3) form at a faster rate because of favorable kinetics, then a metastable, higher free energy state results. The mixture need only be cooled sufficiently rapidly through the above mentioned intermediate range to prevent formation of the equilibrium phases.

In addition to rapid cooling of the melt, the supersaturation necessary to obtain a metastable phase can also be achieved by techniques such as vapor quenching, sputtering, and electro-deposition. In systems with several ceramic oxides metastable phases such as glass form at reasonable cooling rates. Formation of metastable Fe C rather than equilibrium graphite is well-known in the iron-carbon system. Rapid quenching methods utilizing cooling rates of greater than 10^5°K/second are needed to form metastable phases in metallic and some oxide systems.[18]

B. Liquid-Liquid Phase Separation

A homogeneous liquid upon cooling may enter a region in the temperature-composition space where it begins to separate into two liquid phases. This process is often referred to as liquid-liquid phase separation or liquid immiscibility. Because of the effect of immiscibility on the microstructure, a large amount of effort has been made to understand the thermodynamics, kinetics, and morphological aspects of phase separation.

From a thermodynamic standpoint, immiscibility develops when the sum of the free energies of the two separated phases is less than the free energy of the homogeneous solution. The free energy of mixing of two components contains contributions from the heat of mixing and the entropy of mixing. In general, the contribution of the entropy of mixing is negative, and if the heat of mixing is also negative (exothermic), then the free energy of mixing will always be lowered and a homogeneous solution is observed at all temperatures. If, on the other hand, the heat of mixing is positive (endothermic), there will be some temperature at which it will equal the entropic contribution and the free energy of mixing will be zero. If the temperature is lowered further, the free energy cannot be reduced by maintaining a homogeneous solution and thus two liquids will form.

Schematic free energy composition curves and their relation to the liquid immiscibility dome are illustrated in Fig. 4. At any temperature below the consolute point, phase separation will commence. For instance at temperature T_1 two liquids L_1 and L_2 will be at metastable equilibrium, the thermodynamic condition being that the chemical potential of

component A is equal in L_1 and L_2. Similar equilibrium conditions apply to component B.

The spinodal phase boundary shown in Fig. 4 represents the locus of inflection points in the free energy composition curves and represents a region of phase separation where spontaneous decomposition (as opposed to classical nucleation and growth) processes may be operative. A conclusive proof of such spontaneous processes occurring in phase separated glasses is lacking at the present time, and there is a suggestion[19] that interconnected morphologies attributed to spinodal mechanisms may arise by coalescence of small nuclei. Establishing the continuous compositional variability of the separating phases in the early stages of decomposition will constitute direct evidence for spinodal theories.[20]

The origin of immiscibility in oxide glasses has been theoretically modeled by various authors.[21-25] It is believed that silicate melts are ionic solutions containing complex silicate anions, cations, and free oxygen ions. The nature of distribution of these species has been analyzed on the basis of chemical solution theories and physical solution theories (e.g. regular solution models). A recent model[26] proposes the use of a complex multimer of SiO_2 or B_2O_3 as a participant in the regular mixing process with a stoichiometric compound which appears to limit the miscibility gap. Absence of direct thermodynamic data on activities and free energy due to the considerable experimental problems make it difficult to establish the thermodynamic origin of immiscibility. Future availability of such data and better solution models may help resolve the question of liquid phase separation and interaction of the species in glass-ceramic melts.

C. Nucleation and Crystallization in Glasses

Understanding of nucleation and crystallization phenomenon in glasses is important for defining the limits to which glasses can be heated before they crystallize. The subject has also become of increased interest because of the technological development of glass-ceramics.

Crystallization of a liquid occurs, upon cooling below the freezing point, by the formation of composition fluctuations (nuclei), which are large in degree but small in extent.[27] Subsequent diffusion of matter to the nuclei results in growth of the new phase. In certain cases, infinitesimal fluctuations of composition which are small in degree but large in extent may cause the transformation to occur spontaneously (spinodal decomposition).[28] In general, however, nucleation sites such as impurity particles, container walls, or specially introduced dispersed particles act as nucleation catalysts for the crystallization process.

Classical nucleation theory[29] deals with the rates of nucleus formation and growth and attempts a quantitative treatment of the limiting values of these rate processes. For a system free of any heterogeneities, the formation of a nucleus is governed by the balance of the free energy decrease due to nucleus formation and the free energy increase due to the creation of the new crystal-liquid interface. Stable nuclei will thus form when the liquid is sufficiently supercooled so that the free energy decrease due to nucleus formation is larger than the free energy increase due to interface creation. The nucleation rate,

D. Crystal Growth Kinetics

The growth of stable nuclei, once formed by considerations of the previous section, is governed by the rate of diffusion of atoms to the surface of the nuclei and their ability to form new bonds as determined by the crystal structure

The crystal growth rate can either be interface-controlled or diffusion-controlled. Interface-controlled mechanisms are operative when the rate controlling step for crystal growth occurs at the solid-liquid interface and only a short-range molecular rearrangement is necessary. Diffusion controlled growth is accompanied by a large change in composition, and long range diffusion of a species through the bulk liquid is the rate controlling step.

When the rate of crystal growth is interface-controlled, liquid molecules get incorporated into the crystal by molecular attachment and the kinetics of this process determines the interface morphology. In addition to this continuous growth, the crystal may also grow by a two-dimensional nucleation mechanism or by the spiral growth initiating from the step sites of a screw dislocation intersecting the surface. The velocity of crystal growth for interface controlled processes is given by

$$u = fa\nu \exp\left(\frac{\Delta G'}{RT}\right)\left(1 - \exp\left(-\frac{\Delta G}{RT}\right)\right)$$

where f = fraction of sites available for growth

a = molecular diameter

ν = frequency factor for transport at solid-liquid interface

$\Delta G'$ = activation free energy for atom movement across interface

ΔG = free energy change during the liquid-crystal transformation.

Using simplifying assumptions regarding the fraction of sites, f, and approximating the free energy terms it is possible to express the velocity of growth by the expression:

$$u = \frac{fkT}{3\pi a^2 \eta}\left[1 - \exp\left(\frac{-\Delta S_m \Delta T}{RT}\right)\right]$$

where ΔS_m = entropy of fusion

η = viscosity of liquid

ΔT = undercooling of liquid

Several reviews on crystal growth kinetics have pointed to the importance of the entropy of fusion as an important factor for characterization of the crystal-liquid interface. It is theorized that materials with low entropies of fusion ($\Delta S_m < 2R$) will exhibit non-faceted interface morphologies while materials with high entropies of fusion ($\Delta S_m > 4$ to 6 R) exhibit faceted morphologies during growth.

For many high entropy of fusion materials at large undercooling, nucleation of different orientations may occur on or ahead of the interface and such systems exhibit spherulitic crystallization. The kinetics of crystal growth is also strongly affected by impurities and the effect is most pronounced for high entropy of fusion materials. In general, a crystal growth rate which decreases with the square root of time suggests diffusion-controlled growth but a growth rate independent of time can be either due to interface controlled mechanisms or diffusion-controlled growth of certain crystallization morphologies (e.g. fibrillar or spherulitic).

III EXPERIMENTAL METHODS

A. Materials and Sample Preparation

1. SiO_2-Al_2O_3 Glasses for Immiscibility Studies

Several SiO_2 - rich glass compositions were prepared from powders of high purity fused silica* and reactive α- alumina.** The weighed batches (5, 9, 11, 13.5, 23, and 42wt% Al_2O_3) were thoroughly mixed in isopropyl alcohol, wet milled for 24 hours, and the continuously stirred slurry was dried at ≈110°C. The dried mixtures were calcined in platinum crucibles at ≈600°C for 12 hours. Pressed pellets of each composition were placed in molybdenum crucibles (2.5 cms dia. and 3.5 cms height) and heated to ≈1975°C (±10°C) in a tantalum heating furnace# under a vacuum of $\approx 10^{-6}$ torr. After homogenizing at 1975°C for 2 hours, the melts were rapidly quenched at room temperature by allowing helium to flow through the furnace. To ensure homogeneity the glasses were remelted and quenched a second time by the same procedure.

Attempts were also made to obtain Al_2O_3- rich glasses by ultra-fast quenching tehcniques.*** Pressed disks containing 73, 80, and 90 wt% Al_2O_3 were laser melted, the air quenched liquid droplets spinning off the rotating disks were characterized for glass formation. The 80 and 90 wt% compositions yielded opaque crystalline globules. The 73 wt% composition appeared glassy and was characterized by electron microscopy.

---

* -325 mesh Corning 7940
** Alcoa XA-16
\# Richard D. Brew and Co., Concord, NH - Model 41665-4
*** Courtsey of R. A. Happe, North American Rockwell Corp., Downey California.

2. SiO_2-Al_2O_3 Melts for Crystallization Studies

Mixtures containing 42, 60, 73, 80, and 90 wt% Al_2O_3 were prepared from fused silica and reactive α-Al_2O_3 by the procedures described in the previous section (III-A-1). Calcined powdered mixtures were loaded into molybdenum crucibles (≈11 mm diameter x 15 mm height) which were sealed around the lid by electron beam welding and helium leak checked. The sealing and leak checking procedures were necessary to prevent loss of silica by evaporation during the high temperature melting. The sealed crucibles were heat treated in the tantalum resistance furnace under a vacuum of 10^{-6} torr. The crucible assembly and its position relative to the furnace thermocouple are shown in Fig. 6.

The temperature of the furnace chamber was electronically controlled** through the use of a W5Re-W26Re thermocouple (accuracy ±7° at 1800°C). In addition, the temperature of the samples in the furnace was monitored by optical pyrometers (±10°C accuracy at 2000°C) utilizing black body conditions. The pyrometers were calibrated against a NBS secondary standard pyrometer and at the melting point of platinum (1772PC[33] and Al_2O_3(2054°C).[34] All temperatures reported are based on the 1968 International Practical Temperature Scale (IPTS-68).[33]

**Leeds and Northrup Speedomax-H Recorder -Controller.

3. Crystallization Heat Treatments

All melts were homogenized at a temperature of 2090°C (±10°C) for 50 to 60 minutes prior to subsequent heat treatments. Two types of heat treatment schedules were commonly used in the crystallization study. In the first schedule, the homogenized melts were repidly cooled to a predetermined subliquidus temperature, (ranging from 1860°C to a direct quench to room temperature) held at the undercooled temperature for a fixed time, and quenched to room temperature. In the second schedule, homogenized melts were first pre-nucleated by cooling to some subliquidus temperature and reheated to a higher (subliquidus) temperature for the crystallization treatment before quenching to room temperature.

The 42 and 60 wt% Al_2O_3 compositions were selected for greatest scrutiny since the former lies in the center and the latter near the Al_2O_3 - rich phase boundary of the calculated liquid miscibility gap in the present system (see later, Section IV A2). Following the heat treatment, the crucibles were cut on a diamond saw, and the cross-sections were polished for ceramographic examination and phase composition analysis. In order to check for possible melt contamination from the molybdenum crucible polished cross-sections were analyzed for Mo content by the electron beam microprobe. An electron beam image (Fig. 7) showing the distribution of molybdenum in a representative specimen revealed negligible contamination of the melt.

4. Solid State Reaction Experiments

To substantiate the results of metastable and stable phase relationships in the present system,[12] several subliquidus experiments were performed with mixtures containing fused silica plus alumina and

cristobalite plus alumina. The fused silica plus alumina mixtures were prepared as described in a previous section (III A1). The cristobalite in the cristobalite plus alumina mixture was obtained by heating fused silica powder in a platinum crucible at ~1420°C for 7 days. X-ray diffraction confirmed the conversion of the amorphous silica phase to the crystalline state. A 78 wt% cristobalite - 22 wt% Al_2O_3 batch was prepared by dry milling the mixture in a plastic bottle for 72 hours. Pressed pellets of this composition were fired in the temperature range 1100°C to 1300°C in platinum crucibles in air. The size of the pellets before and after firing were measured by a micrometer to obtain the percent shrinkage.

B. Materials Characterization

1. Optical and Scanning Electron Microscopy

Ceramographic polishing procedures consisted of approximately 10 to 15 minutes each on 30, 15 and 6 μm metal-bonded diamond laps, 48-50 hours of vibratory polishing* using 6μ and 1 μm diamond particles, and a final polish for ~48 hours using a 1/4 μm slurry of diamond particles. The highly polished samples were observed in reflected light by interference-contrast micrography.** In some cases a light etch of 10% HF was necessary to observe the microstructure. Specimens for scanning electron microscopy consisted of fracture surfaces of melts and glasses etched in dilute HF. A thin film of gold was generally evaporated on to the sample prior to examination. Some polished sections were also examined in the SEM after prolonged etching in 10% HF.

2. X-ray Diffraction

Samples for phase identification by X-ray diffraction*** were prepared by crushing the material in a mortar and pestle to a size fine enough to pass a -320 mesh sieve. Approximately 10wt% silicon internal standard was added to the crushed sample and the phases identified under the following scanning conditions: 40kv, 20 A, scanning rate 1°/minute, 1°/4°/1° entrance to exit collimation, time constant of 3.0 and range of 1000 cps. All recorded peaks were accurately indexed relative to the standard silicon peaks. Measurements of lattice

---

*FMC Corp., Syntron Div., Homer City, PA.

**Nomarski differential interference-contrast microscope, Zeiss Ultraphot II metallograph, Carl Zeiss, W. Germany.

***Norelco diffractometer, Phillips Electronic Instruments, New York.

†Silicon Standard #640, National Bureau of Standards, Wash., DC.

parameters of the orthorhombic mullite structure were made by locating the reflections corresponding to hkl planes (760), (840) and (422).

3. Electron Beam Microprobe

Samples for chemical composition analysis of the phases present in the microstructure were prepared by depositing a conducting carbon film on the polished sections and by painting the edges of the mounting material with a carbon-ethanol slurry. The samples were loaded into the vacuum chamber of the electron beam microprobe[††] and the primary characteristic X-ray intensities emitted from a specific phase in the microstructure was compared with the emission from an identically coated standard of Al_2O_3 and SiO_2. This method permits a quantitative evaluation of the chemical composition of each phase.

All measurements were made with an accelerating voltage of 15 kv at an X-ray emergence angle of 41°. The AlKα and SiKα intensities were simultaneously recorded on two spectrometers. The analyzers were curved KAP (potassium acid phthalate) crystals bent and ground in the Johansson mode. Intensity counts in 1 μm steps starting with one phase and traversing across the various phases in the microstructure were monitored by logic circuit counters and simultaneously punched on IBM cards for data correction.[35,36] Corrections for dead time, drift, background, absorption and fluorescence were made through a computer program adapted from Frazer et al.[37] for use with the CDC-7600 computer system of this laboratory. Since the difference in atomic numbers of Al and Si is small, no correction for atomic number was made. The output of the

---

[††]Materials Analysis Co., Model 400, Palo Alto, CA.

above program was converted to normalized values of wt% oxides (Al_2O_3 and SiO_2) using additional programs and the data were plotted by incorporation into the Cal-comp plot programs. (Appendix).

4. Transmission Electron Microscopy

Because of the brittle glass samples the normal thinning procedures used in electron microscopy could not be applied. The edges of some specimens were thin enough for transmission studies in the 650 kv electron microscope* but several specimens were prepared following the techniques described by Prebus and Michener.[38] Crushed glasses were carefully placed on a glass slide and gently blown on to the copper grid** which was inserted into the microscope.*** Several particles hanging on to the grid could be observed and a few thin enough for transmission could always be found.

---

*Hitachi(650kv) Electron Microscope, (Japan).

**Pelco Copper Grids, T. Pella Co., Tustin, CA.

***Siemens Elmiskop - 1A, Siemens, W. Germany. (100kv).

IV. RESULTS AND DISCUSSION

A. Metastability

1. Thermodynamic Data from the Phase Diagram

Attempts to model silicate solutions[39,40] consist of the use of chemical solution theories which assume that new chemical species form in the melt. The equilibrium constants corresponding to the ensuing chemical reactions then describe the thermodynamic properties of the mixture. Physical solution theories, on the other hand (e.g. the regular solution models)[41,42] are based on considerations of intermolecular forces which give rise to solution non-ideality. In general, input from both these viewpoints is needed to satisfactorily depict solution behavior.

Models based on the regular solution approximation have been used to calculate thermodynamic data in metal-slag systems,[43] fused salts,[44] and silicates.[45] Adopting a similar approach, Charles described procedures for calculation of activities in alkali-silicates[46] and B_2O_3-SiO_2 solutions[47] and obtained an estimate of the miscibility gaps in these systems. The procedures entail the use of the heat of fusion, assumed to stay constant with temperature, and the position of the liquidus curve on the phase diagram to obtain the activity of the component through the equation:

$$\log_{10} a^L = \frac{\Delta H_m}{4.575} \left[\frac{1}{T_m} - \frac{1}{T_L}\right] = \log_{10} a^S \qquad (1)$$

where a^L = activity of the liquid in the liquidus composition referred to pure liquid standard state.

a^S = activity of solid at the liquidus temperature referred to pure liquid standard state.

ΔH_m = heat of melting, cals/mol.

T_m = melting temperature, °K.

T_L = liquidus temperature, °K.

The data calculated along the liquidus can then be extrapolated to other temperatures by assuming that at a fixed composition the partial heat of solution, ΔH, stays independent of temperature.[46] Thus

$$RT_L \log_{10} \gamma_L = RT \log_{10} \gamma_T \quad (2)$$

where T_L and γ_L = liquidus temperature and activity coefficient at the liquidus, respectively

T and γ_T = temperature and activity coefficient at the chosen temperature T.

R = gas constant = 1.98 cals/mol°K.

The calculated isothermal activity coefficients for one component can then be used in the Gibbs-Duhem equation to obtain data for the other component in the binary system:

$$X_1 \, d \log \gamma_1 + X_2 \, d \log \gamma_2 = 0 \quad (3)$$

where X_1 and X_2 = mole fractions of components 1 and 2.

γ_1 and γ_2 = activity coefficients of components 1 and 2, respectively.

The calculated activities can now be assembled in the following equation to obtaining the free energy of mixing of the liquids, ΔG_m, at a temperature T: $\Delta G_m = RT \left[X_1 \ln a_1 + X_2 \ln a_2 \right]$ (4)

where a_1 and a_2 = activities of component 1 and 2. The variation of the free energy of mixing with composition can be used to locate the width of the miscibility gap at each temperature.

Application of the above procedures to the SiO_2-Al_2O_3 binary system require a well-considered choice of mixing species participating in the regular solution process. For the alkali silicates and borates, Haller et al.[48] proposed the use of a SiO_2 or B_2O_3 multimer and the stoichiometric compound limiting the miscibility gap at the alkali end as the two immiscible liquids. SiO_2 or B_2O_3 multimers were chosen to satisfy the shape of experimentally reported gaps in these systems. On the basis of the various stable and metastable binary phase relationships proposed by Aksay and Pask[12] in the present system, (Fig. 1) several species can be considered as candidates for the solution mixing process. For instance, if the metastable SiO_2 - stoichiometric (3:2) mullite binary system is considered, the liquid phase separation process could be visualized in terms of the following reaction:

$$x\ SiO_2 \cdot y\ Al_2O_3\ (1) \rightleftharpoons X\ SiO_2\ (1) + Y\ \left[Al_{1.6}\ Si_{0.42}\ O_{2.58}\ (1)\right] \quad (5)$$

Where, x and y are the mole fractions of SiO_2 and Al_2O_3 in the starting composition and X and Y are the mole fractions of the unmixed liquids. Similarly, if the metastable SiO_2 - 2:1 mullite (~66.7 mole% Al_2O_3) system is considered the phase separation reaction can be written as:

$$x\ SiO_2 \cdot y\ Al_2O_3\ (1) \rightleftharpoons X\ SiO_2\ (1) + Y\ \left[Al_{1.34}\ Si_{0.33}\ O_{2.67}\ (1)\right] \quad (6)$$

Calculated thermodynamic data for the metastable SiO_2 - mullite system with the stable mullite liquidus (Fig. 1) extended to ~58.0 mole% Al_2O_3 was first obtained. The species that undergo regular solution mixing in such a system were assumed to follow reaction (5) above. Table I lists the cryoscopic data obtained from the SiO_2 liquidus curve using equation 1 with a heat of fusion of 1835 cals/mole for SiO_2[49] and

a melting temperature of 1726°C.[49] The partial molal heat of solution $\overline{\Delta H} = RT\ell n\gamma_{SiO_2}$ (assuming the excess entropy to be zero) is also included in Table I. The data shows an extremely small positive deviation from ideal mixing and thus immiscibility sufficiently above glass transition temperatures (1100°C for SiO_2)[50] will not be expected in the range of compositions under the SiO_2 liquidus curve.

Activities along the mullite liquidus curve of the metastable SiO_2-3:2 mullite (58.0 mole% Al_2O_3) system using the mullite compositions in equilibrium with liquid, can be obtained from equation 1. No experimentally reported value for the heat of fusion of mullite was available. An estimate of the heat of fusion can, however, be made by two approaches. In the first procedure the isothermal activities of SiO_2 obtained in the composition range spanned by the mullite liquidus (using equations 1 to 3) can be matched with the activities obtained from the SiO_2 liquidus when extended metastably to higher mullite mole fractions. Since a correspondence must exist for SiO_2 activities at a fixed composition and temperature, the above procedure yields an estimate of the heat of fusion of mullite of ~27,000 cals/mole. The second method for estimating the heat of fusion is based on the weighted averages of the heats of fusion of the constituents Al_2O_3 and SiO_2. Using the experimentally reported heats of fusion of Al_2O_3 and SiO_2 of 25,700 cals/mole[51] and ~1835 cals/mole,[49] respectively, the heat of fusion of mullite ($0.58\ Al_2O_3\ 0.42\ SiO_2$) can be estimated to be

$$0.58(25,700) + 0.42\ (1835) \approx 16,000 \text{ cals/mole.}$$

In view of the uncertainty associated with the heat of fusion of mullite and because calculated activities (equation 1) are greatly

dependent on the value chosen, data were calculated for a range of values of the heat of fusion from 16,000 to 54,000 cals/mole. The critical points for immiscibility were estimated for each set of data. Similar considerations were used in the analysis of the metastable SiO_2 - 3:1 mullite (0.75 Al_2O_3 0.25 SiO_2) systems.

A representative set of thermodynamic data for the metastable SiO_2 - 3:2 mullite (0.58 Al_2O_3 0.42 SiO_2) system using an estimated heat of fusion for mullite of 16,000 cals/mole is now presented. Table II lists the cryoscopic data from the mullite liquidus metastably extended to ~58 mole% Al_2O_3. Isothermal data at chosen subliquidus temperatures can then be obtained based on the previously stated assumptions regarding the constancy of the partial molal heat of solution (equation 2). This assumption has been reported to show good agreement[52] with calorimetric results for the PbO-SiO_2 system in the temperature range 900°-1700°C. As shown in Fig. 8 the activity coefficients of mullite indicate a strong positive deviation from ideal mixing. The data of Fig. 8 can now be used in equation 3 to obtain isothermal data for SiO_2 (l) (Fig. 9); considerable non-ideality is also apparent from these data.

An analysis of the Al_2O_3 liquidus curve (Fig. 1) over the range 40 to 100 mole% Al_2O_3 is now presented. The activities of Al_2O_3 were calculated from equation 1 using experimentally reported values of the heat of fusion (25,700 cals/mole)[51] and melting temperature[51] (2323°K) of Al_2O_3. In order to obtain the data on activity coefficients for the reacting components a choice of the species involved in the solution mixing is necessary. Since no information on the exact nature of the mixing species is available to warrant a specific choice, two

possibilities can be considered. On the one extreme one can choose SiO_2 and Al_2O_3 as the end components of the pseudobinary system and on the other mullite ($\sim 0.6Al_2O_3 \cdot 0.4SiO_2$) and Al_2O_3 could be considered as the components. Activity coefficients and partial molal heats of solution of Al_2O_3 in these two cases are listed in Tables III and IV. The positive values of $\log \gamma_{Al_2O_3}$ and the partial molal heats of solution of Al_2O_3 indicate a strong positive departure from an ideal solution. Isothermal data for $\log \gamma_{Al_2O_3}$ using SiO_2 and Al_2O_3 as the components is presented in Fig. 10. The activities of Al_2O_3 at various subliquidus temperatures are shown in Fig. 11. Imminent unmixing is indicated below ~1100°C. The data of Fig. 10 can also be used in equation (3) to obtain isothermal values of $\log \gamma_{SiO_2}$ (Fig. 12). The activity coefficients of SiO_2, Al_2O_3 and mullite obtained above are such that the integral molal heat of mixing $\Delta H^M = (X_1 \overline{\Delta H}_1 + X_2 \overline{\Delta H}_2)$ has a positive value. A marked tendency toward liquid immiscibility is, therefore, implied in these data.

The parabolic nature of the variation of the isothermal activity coefficients of SiO_2 (logarithmic) as shown in Figs. 9 and 12 suggests that SiO_2-Al_2O_3 solutions may behave in a "regular" manner. Such behavior may be tested by plotting the α-function suggested by Hildebrand and Scott;[53] the constancy of α with composition indicates a regular solution with a constant heat of mixing and ideal entropy of mixing. For equal molar volumes, the α- function in the present system can be defined as:

$$\alpha = \frac{\log \gamma_{SiO_2}}{\left(X_{Al_2O_3}\right)^2} = \frac{\log \gamma_{Al_2O_3}}{\left(X_{SiO_2}\right)^2} \qquad (7)$$

Isothermal values of $\log\gamma_{SiO_2}$ are shown in Fig. 12 in the composition range 40 to 100 mole% Al_2O_3(assuming SiO_2 and Al_2O_3 as components). The $\log\gamma_{SiO_2}$ data in Fig. 9 was obtained by treating SiO_2 and mullite as components in the composition range 0 to 100 mole% mullite (i.e. 0 to ~58 mole% Al_2O_3). Since the activity of SiO_2 in the solution at a fixed composition must be the same regardless of the components chosen the $\log\gamma_{SiO_2}$ data of Fig. 9 can be converted to a new set of $\log\gamma_{SiO_2}$ values referred to SiO_2 and Al_2O_3 as components. Thus:

$$\log\gamma^{M}_{SiO_2} + \log\chi^{M}_{SiO_2} = \log\gamma^{A}_{SiO_2} + \log\chi^{A}_{SiO_2}$$

$$\log(\text{Activity of } SiO_2) = \log(\text{Activity of } SiO_2)$$

where $\gamma^{M}_{SiO_2}$, $\chi^{M}_{SiO_2}$ and $\gamma^{A}_{SiO_2}$, $\chi^{A}_{SiO_2}$ are activity coefficients and mole fractions of SiO_2 with mullite and Al_2O_3 as components respectively. The α values for each temperature can now be calculated from equation (7). As shown in Fig. 13 α stays essentially constant in the composition range ~15 to 95 mole% Al_2O_3 and thus a reasonable approximation to regular behavior is expected in this range.

2. Calculated Metastable Liquid-Liquid Immiscibility

The thermodynamic data obtained in the previous section can be assembled in the expression $\Delta G_m = RT\,[X_1 \ln a_1 + X_2 \ln a_2]$ (equation 4), to obtain the isothermal free energy of mixing values referred to pure liquid standard states. The variation of the free energy of mixing with composition can then be used to locate the width of the miscibility gap at each temperature. For example the data shown in Figs. 9 and 10 can be assembled to obtain the isothermal free energy of mixing values for the metastable SiO_2-3:2 mullite (0.58 Al_2O_3 0.42 SiO_2) system. Common

tangents to the resulting plot of ΔG_m vs. composition (Fig. 14) represent the compositions at the boundary of the miscibility gap at each temperature.

As stated in the previous section, the thermodynamic data obtained is dependent on the estimate of the heat of fusion of mullite and the end components chosen in the mixing model. Consequently, the effect of the heat of fusion value on the calculated immiscibility was evaluated by obtaining thermodynamic data for a range of values of mullite heat of fusion. As shown in Table V the upper consolute temperature of the miscibility gap is lowered with an increasing value for the heat of fusion. The critical composition is, however, not significantly affected. Figure 15 shows the calculated miscibility gaps for the 16,000 and 27,000 cals/mole values of the heat of fusion of mullite superimposed on the stable and metastable phase diagrams determined by Aksay and Pask.[12] The calculated miscibility gap obtained using SiO_2-2:1 mullite (0.67 Al_2O_3 0.33 SiO_2) as components is also plotted in Fig. 15 using an estimated heat of fusion of 18,000 cals/mole for 2:1 mullite. The upper consolute temperature of the miscibility gap is raised when a higher Al_2O_3 mullite is chosen as a component in the calculation.

The calculated miscibility gap obtained using a heat of fusion of 16,000 cals/mole and SiO_2 and ≈3:2 mullite as components represents a good fit to the experimental data of MacDowell and Beall[15] who proposed a gap between ~7 and 55 mole % Al_2O_3 (at 1100°C). However, the SiO_2-rich phase boundary of the calculated miscibility gap in the present work intersects the estimated curve for glass transformation temperatures ($\eta \approx 10^{14.6}$ poises) at a composition of ~3 mole % Al_2O_3 and

~6.3 mole % Al_2O_3 for calculations based on heats of fusion of 16,000 and 27,000 cals/mole respectively. In their light scattering studies on Al_2O_3 containing high SiO_2 glasses Nassau et al.[54] observed phase separation in the 6.44 mole % Al_2O_3 composition but not in the 6.13 mole % composition. They also estimated the glass transition temperature for the 6.13 mole % Glass to be ~780 ± 30°C. The limiting composition of the miscibility gap at the SiO_2 end can thus be reasonably assumed to lie at ~6.3 mole % Al_2O_3 at ≈800°C. This result suggests that the calculated gap with a mullite heat of fusion of ~27,000 cals/mole (Fig. 15) is the accurate one. On the Al_2O_3 end the limiting compositions for immiscibility are calculated to be ~58 mole % Al_2O_3 (Heat of fusion = 16,000 cals/mole) and ~56 mole % Al_2O_3 (Heat of fusion = 27,000 cals/mole). The phase boundary in Al_2O_3 rich compositions thus appears close to that suggested by MacDowell and Beall.[15]

The thermodynamic data obtained by analyzing the Al_2O_3 liquidus curve (Tables III, IV and Figs. 11, 12) can similarly be assembled in equation (4) to obtain the values of the free energy of mixing as a function of composition. When such data are obtained using SiO_2 and Al_2O_3 as the components (Table II, Figs. 11, 12) a miscibility gap is predicted with a consolute temperature of ≈1120°C at a critical composition of ~78 mole % Al_2O_3. On the other hand if mullite (0.6 Al_2O_3 0.4 SiO_2) and Al_2O_3 are considered as components the upper consolute temperature of the calculated miscibility gap is greater than 2100°C at a critical composition of ~78 mole % Al_2O_3. The large difference in the consolute temperature of the miscibility gaps calculated from the Al_2O_3 liquidus curve underscores the necessity of choosing proper

species for use in the solution model. The choice of SiO_2-Al_2O_3 and mullite (0.6 Al_2O_3 0.4 SiO_2) - Al_2O_3 as components in the analysis presented above represent, perhaps, two extreme cases between which immiscibility in Al_2O_3-rich compositions could be expected. While the location of such a miscibility gap cannot be accurately predicted because of the limitations of the present model and inadequate data on mixing species in the melt, the positive deviations from ideality in the calculated thermodynamic data point to a very strong tendency toward liquid immiscibility in the Al_2O_3-rich compositions.

Since the isothermal values of the α-function $= \frac{\log \gamma_{SiO_2}}{X^2_{Al_2O_3}}$ plotted in Fig. 13 are fairly constant over a broad composition range it is also possible to use a simple model based on assuming SiO_2 and Al_2O_3 as the components across the entire phase diagram to calculate a single miscibility gap which is symmetrical about a mole function of 0.5. The free energy of mixing expression for such a case takes the form:

$$\Delta G_m = 4.575T\ (\alpha . X_1 X_2 + X_1 \log X_1 + X_2 \log X_2)$$

where X_1 and X_2 = mole fractions of SiO_2 and Al_2O_3. The variation of ΔG_m with composition in such a calculation indicates a miscibility gap extending from ≈22 to 75 mole % Al_2O_3 at ≈1200°C. The estimated consolute temperature of the gap is 1350°C ± 50°C.

3. Experimental Evidence for Liquid Immiscibility

In order to seek experimental verification for glass-in-glass immiscibility some SiO_2-rich glass compositions prepared by the procedures described earlier (III.A.1) were examined by direct transmission electron microscopy.

Compositions containing 5wt% through 23wt% Al_2O_3 yielded X-ray amorphous glasses but the 42wt% Al_2O_3 compositions showed diffraction peaks of mullite. A representative polished section of the glass samples was analyzed by the electron microprobe. Glass compositions were found to be within 1wt% of the starting value (Fig. 16, 23wt% Al_2O_3 glass).

Sample preparation for electron microscopy by the commonly used ion-thinning methods was not possible because the samples were brittle. Consequently, the as-prepared glass samples were crushed into a fine powder and gently blown on to a copper grid prior to insertion in the electron microscope. In some samples the edges of the fractured glass fragments were found thin enough for beam transmission in a high voltage (650 kv) electron microscope. A direct transmission electron micrograph of a 23 wt% Al_2O_3-77 wt% SiO_2 glass in the as-quenched condition is shown in Fig. 17. The morphology of the structure is typical of phase separation observed in the nucleation and growth controlled regions of miscibility gaps in several glass-ceramic systems.[55] The selected area diffraction pattern obtained from the phase separated droplets (Fig. 16-B) indicates an essentially amorphous structure verifying the glass-in-glass immiscibility in this composition.

A direct transmission electron micrograph of a 42 wt % Al_2O_3-58 wt% SiO_2 glass is shown in Fig. 18. Considerable inhomogeneity is evident in the structure indicating phase separation. However, the selected area diffraction pattern from the dark droplet-like features reveals the commencement of crystalline order further confirming the tendency of melts greater than ≈25 mole% Al_2O_3 (≈35 wt % Al_2O_3) to crystallize very readily.[15] In view of this rapid crystallization tendency,

experimental verification of the phase boundaries of the calculated miscibility gaps (IV.A.2.) in quenched glass samples is not likely to be obtained by electron microscopy methods. Furthermore, even the glasses prepared by ultra-fast quenching methods,[16,56] either crystallize during the quench or at ≈1000°C during subsequent reheating. Hence, the traditional methods of observing opalascence and clearing upon traversing the boundary of the miscibility gap are not applicable for verifying the calculated liquid-liquid metastable immiscibility in the present system. The experimental verification of the phase boundary in Al_2O_3-rich compositions can, however, be obtained by conducting crystallization studies on selected melts and inferring the temperature of the onset of phase separation from the analysis of the microstructure. (Sec. IV.B).

4. Metastable SiO_2-Al_2O_3 Phase Diagram

The possibility of the existence of a metastable silica-alumina phase diagram in the absence of mullite has been raised by several previous studies. Davis and Pask[11] suggested that mullite nucleation may be preceded by the formation of a metastable glassy phase and proposed a single eutectic metastable phase diagram. Aksay and Pask[12] reported the precipitation of an alumina plus glass assemblage when a 80 wt% alumina melt was slowly cooled to below the peritectic temperature (1828°C). The compositions of the glass phase in metastable equilibrium with the alumina precipitates at a temperature of 1750°C was found to be 48 wt% alumina. Since this composition was close to the alumina liquidus curve as it was metastably extended to lower temperatures, Aksay and Pask[12] suggested that it was evidence for the existence of a

metastable silica-alumina phase diagram.

The formation of non-crystalline phases in subsolidus reactions between cristobalite and corundum has been reported by Staley and Brindley.[57] The compositions of the presumably glassy component of the reaction at 1500°C was estimated by these authors; an average value of 27 wt% Al_2O_3 was reported. The formation of a glassy phase in similar mixtures at 1600°C was reported by de Keyser.[58] The composition of the glass was reported to be 8.4 wt% alumina. Wahl et al.[59] observed reactions in cristobalite-alumina mixtures at temperatures as low as 1200°C with no mullite formation.

The experimental data on subsolidus reactions in the cristobalite-alumina mixtures reported by various investigators above strongly suggest that a metastable glassy phase forms which acts as a precursor for nucleation of the mullite phase. Furthermore, only the Al_2O_3 phase precipitates in high alumina melts (80wt%) cooled slowly from above the liquidus suggesting metastable system in the absence of mullite. Kennard et al.[60] observed a microstructure containing only alumina plus glass in directionally solidified ingots of starting composition equal to 78 wt% alumina. The glass phase was reported to have a composition of 23 wt% alumina.

In order to determine the subsolidus eutectic temperature of the possible metastable alumina-silica phase diagram, several cristobalite-alumina pellets were fired in the temperature range 1100 to 1300°C at intervals of 50°C. If a metastable glassy phase indeed forms as a precursor product, then it is reasonable to expect a sharp increase in the shrinkage of the compacts at and above the eutectic temperature,

since sintering will be accelerated in the presence of the glassy phase. Table VI shows the shrinkage and sintering characteristics of compacts containing 27 wt% alumina and 73 wt% cristobalite. No sintering was observed on firing at 1100, 1150, and 1200°C even after long times. Some sintering was observed in the 1200°C compact but at 1280°C a dramatic change in the shrinkage was found (12.8% linear shrinkage). This rapid change in shrinkage over the temperature interval 1200 to 1280°C suggests that sintering near 1280°C is assisted by liquid phase formation. In light of these data the eutectic temperature of the metastable silica-alumina system can be estimated to be 1265°C (±15).

The metastable extensions of the SiO_2 and Al_2O_3 liquidi to the eutectic temperature of 1275°C were obtained partly by experimental methods and partly by utilizing the thermodynamic data calculated in Section IV.A.1.

The extension of the Al_2O_3 liquidus to lower temperatures was calculated from the data on activity coefficients of Al_2O_3 derived in section IV.A.1. Figure 10 shows the isothermal values of $\log^{\gamma}Al_2O_3$ as a function of composition (between Al_2O_3 mole fractions of 0.4 to 1.0) assuming SiO_2 and Al_2O_3 as components. A least squares fit of the $\log^{\gamma}Al_2O_3$ values at some temperature T yields the expression:

$$\log\gamma^{T}_{Al_2O_3} = A + BX + CX^2 + DX^3$$

where X = mole fraction of Al_2O_3 and A, B, C and D are constants. If the activity coefficients of Al_2O_3 can be assumed to obey the above expression at Al_2O_3 mole fraction less than 0.4 then it is possible to obtain $\log\gamma_{Al_2O_3}$ values at temperature T for Al_2O_3 mole fractions less than 0.4.

The $\log\gamma Al_2O_3$ values at temperature T were transposed to the $\log\gamma Al_2O_3$ value at the liquidus temperature T_L for each composition by using the equation:

$$RT\ \log\gamma^{T}_{Al_2O_3} = RT_L\ \log\gamma^{L}_{Al_2O_3}.$$

The activity of Al_2O_3 along the liquidus is expressed by (equation (1) section IV.A.1) the equation:

$$\log_{10} a^{L}_{Al_2O_3} = \frac{\Delta H_m}{4.575}\left(\frac{1}{T_m} - \frac{1}{T_L}\right)$$

$$\log\gamma^{L}_{Al_2O_3} + \log X_{Al_2O_3} = \frac{\Delta H_m}{4.575}\left(\frac{1}{T_m} - \frac{1}{T_L}\right)$$

Since the heat of melting ΔH_m and the melting point T_m for Al_2O_3 are known[51] the values of $\log\gamma^{L}_{Al_2O_3}$ were used in the above expression to obtain the liquidus temperature at a chosen mole fraction of Al_2O_3. Similar calculations were also made to determine the metastable extension of the SiO_2 liquidus.

The metastable extensions of the SiO_2 and Al_2O_3 liquidi obtained by the above procedures are shown in Fig. 19 superimposed on the stable and metastable equilibria in the system.[12] The extended Al_2O_3 liquidus has a composition of ~28 wt% (17 mole%) Al_2O_3 at 1500°C which is very close to the estimated average composition of $Al_2O_3.5\ SiO_2$ reported by

Staley and Brindley[58] for the non-crystalline metastable phase formed in reactions between cristobalite and corundum at 1500°C. The glass composition of 23 wt% Al_2O_3 (≈15 mole% Al_2O_3) reported by Kennard et al.[57] in solidified ingots of overall composition equal to 78 wt% Al_2O_3 lies at a temperature of ≈1450°C on the extended Al_2O_3 liquidus. This observation suggests that the slowly cooled melt follows the metastable SiO_2-Al_2O_3 diagram proposed in Fig. 19 with the supercooled liquid composition following the extension of Al_2O_3 liquidus and the structure consisting of Al_2O_3 plus liquid with no mullite phase.

B. Crystallization

Considerable tendency toward metastability was demonstrated in the previous section. The relationship between metastability, especially liquid immiscibility, and crystallization of SiO_2-Al_2O_3 melts is now explored.

1. Crystallization Behavior as a Function of Melt Undercooling

Two melt compositions, containing 42 and 60 wt% Al_2O_3, were selected for crystallization studies because the former lies near the center and the latter at the Al_2O_3-rich phase boundary of the miscibility gap (Fig. 19). All heat treatments were conducted in sealed molybdenum crucibles. The melts were homogenized at 2090°C (±10°) for 50 to 60 minutes after which the temperature was rapidly lowered (in 1 to 3 minutes) to a chosen subliquidus temperature T_u. The undercooled melt was held at temperature T_u for a fixed length of time (typically $1\frac{1}{2}$ hours) and then quenched to room temperature by introducing a flow of helium into the furnace chamber.

The microstructure obtained after the homogenized melt (60 wt% Al_2O_3) was held at an undercooled temperature T_u equal to 1862°C for $1\frac{1}{2}$ hours and helium quenched to room temperature is shown in Fig. 20. The microstructure shows mullite needles (~200 to 250μ long) surrounded by a siliceous glass matrix. X-ray diffraction of the sample indicated mullite as the only crystalline phase. The mullite needles and the glass matrix in Fig. 20 were analyzed for chemical composition by the point beam electron microprobe. Composition profiles across the two phase structure were obtained by moving the point beam in 1μ steps.

The profile shows an Al_2O_3 content of ≈78 wt% in mullite and ≈18.5 wt% in the glass.

Microstructures similar to that shown in Fig. 20 were obtained when the homogenized 60 wt% Al_2O_3 melts were undercooled to temperatures of 1860, 1725, 1500 and room temperature (i.e. a direct quench to room temperature from 2090°C). The composition of the mullite needles in all the microstructures (Fig. 21) were ~78 to 78.5 wt% Al_2O_3 suggesting that they had all crystallized in an identical manner. In addition, no significant change in the length or thickness of the mullite needles was observed indicating that crystallization may have occurred not at the various temperatures T_u but possibly at some lower temperature during the quench to room temperature.

Figure 22 shows the microstructure typical of the 60 wt% Al_2O_3 composition heated at T_u = 1325, 1220, and 1025°C for $1\frac{1}{2}$ hours after the initial homogenization. No significant microstructural changes were observed although the size of the mullite crystals was slightly finer. The chemical composition of the mullite crystals in Fig. 22, however, is ~76 wt% Al_2O_3 and the glass composition is ~20.5 wt% Al_2O_3. Similar heat treatments on the 60 wt% Al_2O_3 composition at undercooling temperatures of 925 and 730°C show the mullite composition to be ~74.5 and 75 wt% Al_2O_3. Typical microstructures are shown in Fig. 23 for a representative composition. The composition of mullite obtained by holding the homogenized melt at 925°C prior to cooling to room temperature depended on time of holding at 925°C. As shown in Fig. 24 a holding time of 15 minutes gives a mullite of ~77.6 wt% Al_2O_3 composition. When the undercooled melt is held for longer times, however, the mullite

composition drops to lower Al_2O_3 contents reaching a value of ~73.2 wt% Al_2O_3 after 24 hours. The above observations suggest that mullite crystallization is initiated at some temperature below ~1550°C and the composition of the first mullite crystal to form is ~78.5 wt% Al_2O_3. This result is not surprising since formation of mullite with compositions greater than that indicated by the stable phase diagram (~70.5 wt% Al_2O_3) is well documented when the mullite precipitates from a liquid phase.[61,62] The present data also suggests that the initially formed mullite (~78.5 wt% Al_2O_3) upon continued heat treatment exsolves Al_2O_3 and approaches its equilibrium composition. The Al_2O_3 rejected by the mullite crystal during the reaction enriches the neighboring glass as indicated in Fig. 24.

The microstructure of the 60 wt% Al_2O_3 melt undercooled to 600°C (T_u) following homogenization at 2090°C, held at 600°C for 1 $\frac{1}{2}$ hours and quenched to room temperature is shown in Fig. 25. The morphology of the mullite crystals in a glass matrix is similar to the sample quenched to room temperature from 2090°C without any intermediate holding (Fig. 21). Furthermore, the composition of the mullite in both cases is ~78.5 wt% Al_2O_3 indicating identical crystallization history. The temperature of 600°C in the above treatment lies near the estimated glass transformation temperature ($\eta = 10^{14.6}$ poise) for the 60 wt% Al_2O_3 composition (Fig. 19). Thus, both the as quenched sample and the sample undercooled to 600°C must have crystallized at a temperature above 600°C but below 1550°C. The mullite composition of ~78.5 wt% Al_2O_3 in the structure of Fig. 25 also suggests that the initially

formed mullite did not lower its Al_2O_3 content as in the heat treatments corresponding to T_u = 1325, 1220, 1025, 925 and 730°C because of curtailed diffusion through the rigid high viscosity ($\eta \geq 10^{14.6}$) medium. When the viscosity is sufficiently low for diffusion, the initially formed ~78.5 wt% Al_2O_3 mullite lowers its Al_2O_3 content with continued holding as shown in Fig. 24. The mullite composition after a long hold at 925°C for 24 hrs. is ~73.5 wt% Al_2O_3. This value is very close to the solidus composition for the metastable SiO_2 - "disordered" (2:1)-mullite diagram proposed by Aksay and Pask (Fig. 19). It is, therefore, concluded that when mullite is formed by precipitation from the liquid phase the composition of the mullite corresponds to the metastable equilibrium value of ~73.5 wt% Al_2O_3.

Table VII summarizes the composition data for crystallization of the 60 wt% Al_2O_3 melt as a function of undercooling. The composition of mullite in samples 60=Q, 60-18, 60-17, 60-15 and 60-6 are ~78 to 78.5 wt% Al_2O_3 surrounded by a glass of ~18 wt% Al_2O_3. On the other hand, when the melt is held at lower temperatures (60-13, 60-12, 60-10, 60-9 and 60-7) the mullite composition is ~75 to 76 wt% Al_2O_3 surrounded by a glass of ~20 to 21 wt% Al_2O_3. These data then suggest that the melt is supercooled without crystallization through some temperature below 1550 but above 1325°C. At some temperature between 1325°C and 1550°C crystallization of mullite is initiated and the first mullite formed has a composition of ~78 to 78.5 wt% Al_2O_3 which is subsequently lowered on further heat treatment. The relationship of the observed crystallization behavior to metastable liquid-liquid immiscibility (Sec. IV.A.2,3) is treated in the following section.

2. Relationship Between Crystallization and Liquid Immiscibility

Since mullite crystallization appears to commence at a temperature between 1325°C and 1550°C (for the 60 wt% Al_2O_3 melt) and since the phase boundary of the metastable liquid immiscibility (Fig. 19) is within this temperature range, it is appealing to develop a reasoning for the observed crystallization behavior in relation to prior liquid immiscibility.

In general, a metastable glass phase forms because the more stable crystalline phase is kinetically unfavorable. If heat treated for a sufficient length of time, the metastable glass phase will separate into two glasses unless crystallization intervenes. This general view based on kinetics states that the crystalline phase cannot appear simply because the other reaction (either single phase or phase separated glass formation) is faster. There is, however, a possibility that the crystalline phase will be actually forbidden by thermodynamics to precipitate until after the precursor metastable reaction is complete, as suggested by Cahn.[73] Let us consider the free energy of mixing versus composition curves for the metastable liquid L and the stable solid S at a temperature T below the upper consolute temperature of the miscibility gap, as shown schematically in Fig. 26. If the mullite phase(solid)precipitates from the liquid of composition Co the free energy is increased corresponding to the segment F_L-F_M. However, after the liquid immiscibility step is complete the mixture of liquids L_1 and L_2 has a free energy corresponding to F_S. Transformation to the mullite phase now involves a decrease in free energy (F_S to F_M).

Applying the above principles to the observed crystallization behavior as a function of melt undercooling reported earlier, it can be argued that the 60 wt% Al_2O_3 melt is supercooled to near the immiscibility boundary because mullite formation is thermodynamically blocked until the precursor reaction (i.e. unmixing into two glasses) is complete. The crystallization of the melt can thus be visualized in terms of the following steps: (i) Supercooling of the liquid to the phase boundary of the miscibility gap, (ii) Commencement of liquid immiscibility at ~1325 ± 25°C, (iii) Crystallization of the Al_2O_3-rich phase separated glass to mullite of ~78.5 wt% Al_2O_3, and (iv) Reduction in Al_2O_3 content of mullite from ~78.5 to ~73.5 wt% Al_2O_3 on heat treatment above glass transformation temperatures. In support of the above crystallization process, glass compositions (Table VII) are very close to the SiO_2 rich phase boundary of the miscibility gap (~18 to 20 wt% Al_2O_3) at a temperature of ≈1350°C, for heat treatments involving very little or no time within the miscibility gap.

In contrast to the above view of liquid immiscibility as a precursor to crystallization, it is also possible to consider crystallization of a melt in terms of fluctuation theories.[64,65] According to these theories the melt, although macroscopically homogeneous, contains regions of fluctuational heterogenities varying in size from 200 to 5000Å. These heterogeneous compositional and structural fluctuations do not have sharp interfaces but resemble the "future" precipitating phase (stable or metastable). As the melt cools, heterogenieties due to the miscibility gap are added to the above fluctuations.

The experimental data on crystallization can then be explained on the basis of the fluctuation theories by assuming the possibility of compositional and structural fluctuations in the present SiO_2-Al_2O_3 melts at ~2090°C closely resembling the high Al_2O_3 (~78.5 wt%) metastable mullite phase. If such heterogeneous regions exist then the melt will be able to crystallize readily with a very slight structural rearrangement.

The fluctuations in the melt will correspond to high-Al_2O_3 and high-SiO_2 regions. During cooling of the melt, short range diffusion of the SiO_2 molecular species occurs. As the above molecular species deplete the Al_2O_3-rich composition fluctuations, crystallization of the mullite phase occurs by the rapid growth of these fluctuations. Since the crystallization to mullite involves no long range diffusion, but only a small structural rearrangement in the fluctuations in the melt, one can reasonably expect mullite precipitates of coarse size in the quenched melts.

The microstructures in the as-quenched melt (Fig. 21) show mullite precipitates of ≈15 to 20μ X 200 to 250μ dimensions. Since the melt was quenched to room temperature from 2090°C in 1 to 2 minutes the rapid crystallization observed may have occurred by the structural rearrangement and virtually diffusionless process discussed above.

The fluctuation model of crystallization is a possibility for high Al_2O_3 melts, but the experimental data on the 60 wt% Al_2O_3 melts reported earlier appears to support the view of liquid immiscibility as a precursor to crystallization.

3. Crystallization Behavior as a Function of Nucleation Conditions

The 42 and 60 wt% Al_2O_3 melts were subjected to chosen heat treatments within and outside the miscibility gap. Quenched melts which would have mullite precipitates as described, were then given heat treatments at 1725°C (±10) for various times. Several significant changes both in the morphology and the composition of the mullite crystals were observed.

Figure 27 shows a typical microstructure obtained when a 60 wt% Al_2O_3 containing melt was homogenized at 2090°C, held at 1500°C for 15 mins, reheated at 1725°C for 1 $\frac{1}{2}$ hours, and quenched. The morphology of the mullite needles is very similar to the melts shown in Fig. 21. Further, the chemical composition of the mullite and glass phases determined by the point beam electron microprobe was found to be 77.9 wt% Al_2O_3 and 19 wt% Al_2O_3 respectively. These compositions are the same as those for melts undercooled to 1860, 1725, 1500°C and quenched to room temperature. Thus, the heating at 1500°C for 15 minutes (Fig. 27) simply supercools the melt without nucleation and subsequent reheating to 1725°C did not result in any nucleation or crystallization. The mullite crystals observed in Fig. 27 must then have nucleated and grown during the quench to room temperature by a similar mechanism as the microstructures in Fig. 21.

The effect of nucleating a homogenized 60 wt% Al_2O_3 melt at a temperature well within the miscibility gap (925°C, 15 minutes) and recrystallizing at 1725°C for 1 $\frac{1}{2}$ hours, however, is shown in Fig. 28. The finer crystal size of mullite observed here (Fig. 27) in comparison to the previous example is suggestive of the appearance of crystals due

to the hold at 925°C. Subsequent reheating to 1725°C causes crystal growth of mullite around the nuclei established at 925°C. The composition profile across the two phase structure of Fig. 28 shows a mullite with an Al_2O_3 content of ~75 wt% Al_2O_3 and a glass of ~16 wt% Al_2O_3 (Fig. 29).

In keeping with the steps in the crystallization process developed earlier, the melt of Fig. 28 on cooling to 925°C two glass phases which is followed immediately by precipitation of a high Al_2O_3 (~78.5 wt%) mullite, which in turn begins to exsolve Al_2O_3. During the reheating step (1725°C, 1 $\frac{1}{2}$ hours) recrystallization occurs with the mullite crystals approaching the metastable equilibrium value of ~73.5 wt% Al_2O_3

Figure 30 shows the microstructure obtained when the 42 wt% Al_2O_3 melt was quenched to room temperature and reheated at 1725°C for 1 $\frac{1}{2}$ hours. The mullite morphology obtained is typical of the needlelike crystals growing in the presence of a liquid phase. The composition of mullite in this case corresponds to 74.5 wt% Al_2O_3. A 60 wt% Al_2O_3 composition heat treated at the same time under conditions identical to those for the sample in Fig. 30 resulted in the microstructure shown in Fig. 31. The composition of the mullite phase is ~75.5 wt% Al_2O_3 and the morphology of the needles shows bundles of well aligned crystals surrounded by the glass matrix. The differences in morphology in these two samples is probably related to the amount of mullite crystals.

In order to evaluate the rate at which the precipitated mullite crystals approach the metastable equilibrium composition of 73.5 wt% Al_2O_3, quenched melts were heated at 1725°C for various times. The schedule for both the 42 wt% Al_2O_3 and 60 wt% Al_2O_3 melts consisted of

homogenization at 2090°C for 50 to 60 minutes and cooling to room temperature by shutting off the furnace power. The as-cooled samples showed X-ray detectable mullite which was very fine (~0.02μ) in the 42 wt% composition and coarse (≈20x250μ) in the 60 wt% composition. The as-cooled melts with mullite crystals were recrystallized by heating to 1725°C and holding for various lengths of time prior to cooling to room temperature.

Figure 32 shows the microstructure obtained on heating of the as-quenched 60 wt% melt at 1725°C for 1 $\frac{1}{2}$ hours. The morphology of the mullite in this sample was the same as in Fig. 31, but the Al_2O_3 content of mullite is lowered to 75.5 wt%.

Figure 33 traces the microstructural and composition changes in the 60 wt% composition after heating for 1 $\frac{1}{2}$, 5 $\frac{1}{2}$, and 70 hours at 1725°C. The original needle-like structure of mullite in the as-quenched samples (Fig. 29) breaks up into finer mullite precipitates whose composition is reduced in Al_2O_3 with time. Table VIII summarizes the composition data for the 60 wt% Al_2O_3 series as a function of nucleation conditions.

The change in crystal size of mullite with time at 1725°C after quenching to room temperature is shown in Fig. 34 for the 42 wt% Al_2O_3 composition. The recrystallization of mullite is accompanied by a change in Al_2O_3 content from ~76 wt% Al_2O_3 to ~73.5 wt% Al_2O_3 after a hold at 1725°C for 1 $\frac{1}{2}$ hours, (Table IX). Subsequent crystal coarsening occurs with essentially no change in composition, suggesting some interface controlled mechanism as being the rate limiting step in the crystallization.

Figure 35 shows the coarsening steps in crystallization of the 42 wt% Al_2O_3 sample reheated to 1725°C (5 $\frac{1}{2}$ hours). (Fig. 34, 42QR - 5 $\frac{1}{2}$ hours). The microstructures shown in Fig. 35 indicate a coalescence of the fine mullite crystals during the recrystallization step at 1725°C. The coarsening of the fine mullite structure to long needles, whose thickness increases with time of holding, occurs by the formation of edge contacts between two needles. Subsequent mass transport results in the interface controlled crystal growth suggested by small composition changes.

4. Subliquidus Silica-Alumina Reactions

The product of solid state reactions between fused silica and alumina is believed to be a mullite phase (3:2 type) of composition corresponding to the stable equilibrium value of 70.5 wt% alumina.[12] The morphology of the mullite of the solid state type is typically globular[61] while even the slightest amount of liquid phase promotes the needlelike morphology.[62]

In the previous section on crystallization, the needlelike mullite morphology was consistently observed since precipitation had always occurred from the melt. Furthermore, this morphology persisted even upon reheating at subliquidus temperatures for long times. The mullite composition, in this case of the 2:1 type, was 78.5 wt% alumina in the first formed mullite and decreased to 73 wt% alumina after reheating at 1725°C for up to 100 hours. Since the mullite grown at temperature in solid state reaction is expected to be lower in Al_2O_3 content, reactions between silica and alumina at subliquidus temperatures were studied to

determine the validity of the hypothesis regarding the compositions of mullite.

A 60 wt% Al_2O_3 - 40 wt% SiO_2 mixture was pressed into pellets and fired in air at ≈1700°C for 96 hours. The microstructure of the specimen is shown in Fig. 36. The white areas in the optical micrograph of Fig. 36 show sintered Al_2O_3 particles which are surrounded by a light gray layer of mullite that formed at 1700°C by a diffusion controlled reaction with the siliceous liquid. The thickness of the mullite layer adjacent to the sintered Al_2O_3 particles is ≈6μ after 96 hours of reaction. The diffusion controlled nature of the reaction through the mullite layer is indicated in the slow rate observed. The composition of the mullite layer was determined by the electron beam microprobe to be ≈70.6 wt% Al_2O_3 which corresponds to the stable equilibrium composition. The liquid phase next to the mullite layer has a composition of 11 wt% Al_2O_3

Precipitation of mullite needles in the liquid phase was also observed as shown in Fig. 36(c). These needles formed during the quench from 1700°C after holding at temperature for 96 hours. The microstructure shown in Fig. 36 is unique in that two different mullite morphologies can be seen in the same sample. The scanning electron micrographs of Fig. 36(b) show the sintered Al_2O_3 particles with fragments of the mullite layer. The mullite growing out of the liquid phase as isolated needlelike islands is shown in Fig. 36(c). The relative ratios of Al/Si in the two mullites was determined by the EDAX (Energy Dispersive Analysis of X-rays) attachment to the scanning electron microscope.

The Al/Si intensity ratios are shown in Fig. 37 by focusing the beam (~1μdiameter) on the sintered Al_2O_3 area (Fig. 36(a)) and on the mullite needles in the liquid phase matrix (Fig. 36 (c)). The higher Al/Si ratio in Fig. 36(c) is direct evidence of a higher Al_2O_3 mullite precipitating from a liquid phase.

Additional subliquidus experiments were performed between SiO_2 and Al_2O_3 mixtures of 60 wt% Al_2O_3 composition to provide evidence for the stable phase diagram (Fig. 19). Conflicting phase equilibria studies by static quenching methods reported in literature have relied on examination of phases obtained in quenched samples, after homogenization just above the liquidus. For example, Aramaki and Roy homogenized a 50 mole% Al_2O_3 (~63 wt% Al_2O_3) composition at 1852±10 for 9 minutes and reported mullite and glass as the only phases present. The temperature of 1852°C is within the stable phase field of Al_2O_3 plus liquid as shown in the phase diagram of Fig. 19. Consequently, Al_2O_3 must be observed in such mixtures upon quenching unless no nucleation sites are available for the nucleation of the alumina phase; the difficulties in nucleating the stable phase (Al_2O_3) at small undercooling have been discussed by Aksay and Pask.[12]

It was hypothesized that if the particle size of Al_2O_3 in reaction with SiO_2 was fine enough for complete reaction to form mullite below the peritectic temperature then no Al_2O_3 sites would be available for nucleation when the mixture was held above the peritectic temperature (Fig. 19). Thus, even though temperatures between 1828°C and 1900°C (for the 60 wt% Al_2O_3 mixture) lie in the stable Al_2O_3 phase field, the starting mixtures containing fine Al_2O_3 particles will show mullite plus

glass as the phases after quenching to room temperature from above 1828°C. However, if the Al_2O_3 particle size in the starting mixture is coarse the mullite formation reaction will be incomplete (as in Fig. 36) and Al_2O_3 nuclei would be present at the higher temperature (>1828°C).

To test the above hypothesis mixtures of overall composition equal to 60 wt% Al_2O_3 and 40 wt% SiO_2 were prepared by using Al_2O_3 particles of size ≈0.03μ, (Linde-Al_2O_3)8μ(A-16, α-Al_2O_3) and 45μ(A-14, α-Al_2O_3 agglomerates). Well blended mixtures were sealed in molybdenum crucibles and heated to 1725°C in 1 hour. The mixtures were held at 1725°C for 4 days. The temperature was then raised to 1855°C and maintained for 36 hours, before rapidly cooling the mixtures to room temperature. X-ray diffraction patterns obtained from the three mixtures using Si as an internal standard revealed the presence of Al_2O_3 only in the mixture containing the coarse A-14 alumina particles (Fig. 38). The long hold at 1725°C resulted in complete reaction of the finer Al_2O_3 in the Linde and A-16 mixtures to form mullite but residual Al_2O_3 was present in the A-14 mixture when the temperature was raised to 1855°C. Since the Al_2O_3 in this case found itself in the stable phase field of Al_2O_3 plus liquid (see Fig. 19) it did not go into solution even though the diffusivity of $\approx 10^{-6}$ cm^2/sec at 1850°C would require the complete dissolution of a 50μ Al_2O_3 particle in about 100 seconds. The fact that Al_2O_3 still persisted in this mixture indicates that at 1855°C the mixture was in the stable phase field. It is of interest to note that presence of Al_2O_3 in the 60 wt% Al_2O_3 mixture held at 1855°C for 36 hours and quenched to room temperature is inconceivable on the basis of

the SiO_2-Al_2O_3 system showing a congruently melting mullite proposed by previous authors.[8-10]

V. SUMMARY AND CONCLUSIONS

The regions of metastable liquid immiscibility has been calculated from the thermodynamic data derived from the phase diagram of the SiO_2-Al_2O_3 system. Positive deviations from an ideal solution were indicated both in SiO_2-rich and Al_2O_3-rich compositions. Miscibility gaps were calculated for various combinations of components in the system based on regular solution approximations.

Glasses high in SiO_2 were examined by transmission electron microscopy for evidence of liquid phase separation. Liquid-liquid immiscibility was demonstrated in glasses containing between ≈7.5 and 20 mole% Al_2O_3. The fine scale of phase separated glassy droplets (≈400Å) dispersed in a glass matrix results from the existence of the subliquidus (metastable) liquid miscibility gap.

Crystallization of SiO_2-Al_2O_3 melts homogenized at ≈2090°C was studied. Melts containing greater than ≈30 mole% Al_2O_3 crystallized very readily to form a metastable mullite phase plus a residual siliceous glass. Extensive crystallization studies on selected melt compositions provided experimental evidence for the relationship between liquid immiscibility and crystallization.

The microstructures obtained by crystallization of the melts were analyzed for chemical composition by the electron beam microprobe. The data for the 60 wt% Al_2O_3 melt crystallized by progressive undercooling after homogenization at 2090°C suggests that the melt supercools to ≈1350°C prior to crystallization. Since the temperature of 1350°C is near the phase boundary of the liquid miscibility gap for the 60 wt% composition calculated earlier, it is concluded that phase separation

may be an essential precursor to crystallization of the melt. The extremely rapid crystallization tendency of Al_2O_3-rich melts to coarse (≈250μ long) mullite needles and the diffuse interface between the mullite and glass phases may also be due to the existence of fluctuational heterogenieties in the melt structure itself.

Mullite with an Al_2O_3 content of ≈78.5 wt% precipitates from the melt upon crystallization. The composition of this metastable mullite phase was shown to change with heat treatment to ≈73.5 wt% Al_2O_3. This value corresponds to the solidus composition of the metastable SiO_2 - "disordered" or 2:1 mullite diagram.[12] The morphology of the mullite precipitating from the liquid phase was needle-like and persisted during the transformation of the high-alumina mullite to lower Al_2O_3 compositions upon heat treatment.

Mullite with compositions (≈70.6 wt% Al_2O_3) close to the stable equilibrium diagram[12] formed at subliquidus temperature in reactions between SiO_2 and Al_2O_3 mixtures. Needle-like mullite crystals with an Al_2O_3 content higher than the equilibrium value formed in the residual liquid phase during cooling. Subliquidus reactions in SiO_2-Al_2O_3 powders containing different particle sizes of Al_2O_3 provided verification of stable phase equilibria in the system.

A single eutectic metastable SiO_2-Al_2O_3 phase diagram in the absence of mullite was proposed. Extensions of the stable SiO_2 and Al_2O_3 liquidi to lower temperatures was based on experimental data on phase compositions in crystallized melts high in Al_2O_3;calculations based on thermodynamic data were also used to position the liquidi. The eutectic temperature of the proposed metastable phase diagram

determined from subsolidus reactions in cristobalite-corundum pellets is ≈1275°C; the eutectic composition is estimated to be ≈12 mole % Al_2O_3.

ACKNOWLEDGMENTS

Professor Joseph A. Pask graciously encouraged my efforts through many uncertain times. The benefit of learning from his wisdom and well-known excellence has been significant education and a highly satisfying experience. It is a pleasure to acknowledge the many hours of eminent thermodynamic advice from Professors Alan Searcy, Leo Brewer and Dr. Alexandra Navrotsky.

Pleasant interactions with my colleagues, Ilhan Aksay, Carl Hoge and Victor Draper greatly assisted the completion of this work. Conversations with numerous friends in Berkeley helped me keep my perspective.

My wife, Smita, cheerfully put up with the difficulties of student life and kindled my interest at critical junctures. I am also very appreciative of the understanding of my parents throughout my educational years.

The support staff of the Materials and Molecular Research Division, Lawrence Berkeley Laboratory provided expert technical assistance. I would specially like to thank Gay Brazil for efficient manuscript preparation, Rich Lindberg for assistance with the electron microprobe, and Gloria Pelatowski for making the superb technical drawings.

This work was performed under the auspices of the U.S. Energy Research and Development Administration through the Materials and Molecular Research Division of the Lawrence Berkeley Laboratory.

REFERENCES

1. S. D. Stookey, Ind. Eng. Chem. 51, 805 (1959).

2. J. F. MacDowell, Proc. Brit. Ceramic Soc. 3, 229 (1965).

3. S. M. Ohlberg et al., "Symposium on Nucleation and Crystallization in Glasses", pp 55-62, M. K. Reser et al. (Editors), American Ceramic Society, Ohio, (1962).

4. W. B. Hillig, ibid, pp 77-89.

5. (a) N. L. Bowen and J. W. Greig, J. Amer. Ceramic Soc., 7, 238 (1924).

   (b) ibid, 7, 410 (1924).

6. G. Trömel, The Physical Chemistry of Steel-Making, J. F. Elliot, Editor, MIT Press, New York (1958).

7. J. H. Welch, Nature, 186, 545 (1960).

8. S. Aramaki and R. Roy, J. Amer. Ceramic Soc., 42, 644 (1959).

9. S. Aramaki and R. Roy, ibid, 45, 229 (1962).

10. S. Aramaki and R. Roy, Nature, 184, 631 (1959).

11. R. F. Davis and J. A. Pask, J. Amer. Ceramic Soc., 55, 525 (1972).

12. I. A. Aksay and J. A. Pask, ibid, 58, 507 (1975).

13. (a) F. Ya. Galakhov and S. F. Konovalova, Izv. Akad. Nauk SSSR, Ser. Khim, 8, 1373-77 (1964).

    (b) ibid, pp 1377-1383

14. D. Ganguli and P. Saha, Mater. Res. Bull., 2, 24 (1967).

15. J. F. MacDowell and G. H. Beall, J. Amer. Ceramic Soc., 52, 17 (1969).

16. T. Takamori and R. Roy, ibid, 56, 639 (1973).

17. P. Duwez, et al., J. App. Physics, 31, 1136 (1960).

18. L. E. Topol, et al., J. Non-Cryst. Solids, 12, 377 (1973).

19. (a) W. Haller, J. Chem. Physics, 42, 686 (1965)

(b) W. Haller and P. Macedo, Phys. Chem. of Glasses, 9, 153 (1968).

20. J. W. Cahn, J. Chem. Physics, 42, 93 (1965).

21. B. E. Warren and A. G. Pincus, J. Amer. Ceramic Soc., 23, 301 (1940).

22. F. D. Richardson, Disc. Faraday Soc., 4, 244 (1968).

23. C. R. Masson, Proc. Royal Soc. A287, 201 (1965).

24. R. J. Charles, Phys. Chem. of Glasses, 10, 169 (1969).

25. F. D. Richardson, in "Physical Chemistry of Melts in Metallurgy", vol. 1, p 87-92, Academic Press, New York (1974).

26. P. B. Macedo and J. H. Simmons, J. Res. of NBS, Sec. A, 78, 53 (1974).

27. J. W. Gibbs, Collected Works, vol. 2, p 105, Yale Univ. Press, Conn. (1948).

28. J. W. Cahn and R. J. Charles, Phys. and Chem. of Glasses, 6, 181 (1965).

29. D. Turnbull and J. C. Fisher, J. Chem. Physics, 17, 71 (1949).

30. K. A. Jackson, et al., J. Crystal Growth, 1, 1 (1967).

31. D. R. Uhlmann in "Advances in Nucleation and Crystallization of Glasses, pp 91, M. Reser, et al. Editors, American Ceramic Soc. (1971).

32. K. A. Jackson, in "Crystal Growth", Proc. of IVth Int. Conf. on Cryst. Growth, pp 130-136, North Holland Publ. Co. Amsterdam (1974).

33. F. D. Rossini, J. Chem. Thermodyn., 2, 447 (1970).

34. S. J. Schneider and C. L. McDaniel, J. Res. NBS, 71A, 317 (1967).

35. R. Theisen, Quantitative Electron Microprobe Analysis, Springer Verlag, Inc., New York (1965).

36. K. F. J. Henrich, Ed., Quantitative Electron Probe Microanalysis, NBS Special Publ. 298, U.S. Govt. Printing Office, Washington, DC, (1968).

37. J. Z. Frazer, et al., Computer Programs EMX and EMX2 for Electron Microprobe Data Processing, Scripps Institute of Oceanography, University of California, San Diego, California.

38. A. F. Prebus and J. W. Michener, Ind. Eng. Chem. 46, 147 (1954).

39. F. D. Richardson in "Physical Chemistry of Melts in Metallurgy", pp 140, Acad. Press, New York (1974).

40. J. M. Prausnitz, Molecular Thermodyn. of Fluid Phase Equilibria, Prentice-Hall (1969).

41. J. H. Hildebrand, J. Amer. Chem. Soc. 51, 66 (1929).

42. H. K. Hardy, Acta. Met., 1, 202 (1953).

43. J. Chipman, Disc. of Faraday Soc., No. 4, 23, (1948).

44. T. Forland in "Fused Salts", p 63, B. R. Sundheim, Editor, McGraw-Hill Book Co. (1964).

45. M. Rey, Disc. of Faraday Soc., No. 4, 257 (1948).

46. R. J. Charles, J. Amer. Ceramic Soc., 50, 631 (1967).

47. R. J. Charles and F. E. Wagstaff, ibid, 51, 16 (1968).

48. W. Haller, et al., ibid, 57, 120 (1974).

49. M. A. Moseman and K. S. Pitzer, J. Amer. Chem. Soc., 63, 2348 (1941).

50. E. H. Fontana and W. A. Plummer, Phys. Chem. of Glasses, 7, 139 (1966).

51. E. E. Shpil'rain, et al., High Temperatures – High Pressures, 4, 605 (1972).

52. P. C. Hess, Geochimica et Cosmochimica Acta, 39, 671 (1975).

53. J. H. Hildebrand and R. L. Scott, Solubility of Non-Electrolytes, p 35, Dover Publications, New York (1964).

54. K. Nassau, et al., J. Amer. Ceramic Soc., 58, 461, (1975).

55. J. J. Hammel, J. Chem. Physics, 46, 2234 (1967).

56. R. Krepski, et al., J. Materials Science, 10, 1452 (1975).

57. W. G. Staley and G. W. Brindley, J. Amer. Ceramic Soc., 52, 616 (1969).

58. W. L. de Keyser in "Science of Ceramics", vol 2, pp 243, G. H. Stewart, Editor, Academic Press (1965).

59. F. M. Wahl, et al., Amer. Mineralogist, 46, 1064 (1961).

60. F. L. Kennard, et al., in "Reactivity of Solids:, J. S. Anderson, Editor, p 580 (1972).

61. B. B. Ghate, et al., Amer. Ceramic Soc. Bulletin, 52, 670 (1973).

62. W. Lohre and H. Urban, Ber. Deut. Keram. Ges., 37, 249 (1960).

63. J. W. Cahn, J. Amer. Ceramic Soc., 52, 118 (1969).

64. V. N. Filipovich, in "Structural Transformation in Glasses at High Temperatures", Edited by N. A. Toropov and E. A. Porai-Koshits, Vol. 5, p 11, Consultants Bureau Translation, New York (1965).

65. E. A. Porai-Koshits, ibid, p 1.

Table I. Thermodynamic Data From the Silica Liquidus.

Liquidus Composition	Liquidus Temp. (°K)	Activity of SiO_2	Log Activity Coefficient of SiO_2	Partial Molal Heat of Solution
Mole Fraction of Mullite				
.0167	1973	0.994	+0.0047	42.4
.043	1927	0.983	+0.0116	102
.067	1903	0.977	+0.020	174
0.086	1860	0.966	+0.024	204

Table II. Thermodynamic Data from Mullite Liquidus (Heat of Fusion ≈16,000) of mullite.

Mole Fraction Mullite (Liquidus) Compositions)	Liquidus Temperature (°K)	$\text{Log}_{10}\ \gamma^{L}_{\text{Mullite}}$	Partial Molal Heat of Solution ΔH (Mullite) Cals/mole
0.086	1860	.803	6870
0.129	1953	0.719	6459
0.172	1998	0.635	5836
0.215	2013	0.552	5111
0.258	2025	0.483	4499
0.344	2048	0.378	3561
0.430	2059	0.291	2756
0.515	2079	0.229	2190
0.601	2090	0.171	1644
0.687	2101	0.122	1179
0.773	2115	0.082	798
0.945	2133	.009	88

Table III. Thermodynamic Data from Al_2O_3 Liquidus with SiO_2 and Al_2O_3 as Components.

Mole Fraction Al_2O_3 (Liquidus Composition)	Liquidus Temperature (°K)	$Log_{10}\gamma^{L}_{Al_2O_3}$	Partial Molal Heat of Solution ΔH (Al_2O_3) Cals/mole
0.40	2105	0.14441	1390.7
0.45	2148	0.14779	1452.4
0.50	2195	0.15895	1596.2
0.55	2205	0.12933	1304.7
0.60	2226	0.11586	1179.9
0.65	2243	0.10042	1030.5
0.70	2254	0.08057	830.8
0.75	2266	0.06390	662.4
0.80	2280	0.05118	533.9
0.85	2288	0.03351	350.8
0.90	2301	0.02261	238.0
0.95	2310	0.00866	91.5
1.00	2323	0.0000	≈0

Table IV. Thermodynamic Data from Al_2O_3 Liquidus with Mullite (0.6 Al_2O_3 0.4 SiO_2) and Al_2O_3 as Components.

Mole Fraction Al_2O_3 (Liquidus Composition)	Liquidus Temperature (°K)	$\text{Log}_{10}{}^{L}\gamma Al_2O_3$	Partial Molal Heat of Solution $\Delta H(Al_2O_3)$ Cals/mole
0.010	2226	1.894	19394
0.125	2243	0.816	8420
0.188	2253	0.650	6737
0.250	2257	0.528	5481
0.312	2261	0.439	4566
0.375	2266	0.365	3805
0.438	2273	0.305	3189
0.500	2280	0.255	2675
0.625	2288	0.167	1758
0.750	2301	0.102	1080
0.812	2306	0.071	753
0.938	2316	0.021	224
1.000	2323	0.000	0

Table V. Effect of Heat of Fusion of Mullite on Calculated Liquid Miscibility Gaps.

Heat of Fusion of Mullite (Cals/mole)	Upper Consolute Temperature(±10°C)	Critical Composition, Mole% Al_2O_3
16,000	1635	36.0
27,000	1540	35.5
36,000	1380	35.0
45,000	1230	34.5
53,000	1090	34.0
72,000	725	34.0

Table VI. Subsolidus Reactions in Cristobalite-Corundum Mixtures (≈27 wt% Al_2O_3-73 wt% Cristobalite).

Temperature (°C ± 20)	Time at Temperature	Size of Compacts		Percent Shrinkage (Linear)	Phases identified after firing (x-ray)
		before firing	after firing		
1130	40 days	0.25" dia. x 0.108" thick	0.2495 x ?	Pellet crumbled	α-Al_2O_3 Cristobalite
1200	150 hrs.	0.25" dia. x 0.110" thick	0.2492 x ?	Pellet crumbled	α-Al O Cristobalite
1230	120 hrs.	0.25" dia. x 0.103 thick	0.2486 x 0.102"	<1%	α-Al_2O_3 Cristobalite
1250	120 hrs.	0.25" dia. 0.072" thick	0.2480 x 0.070"	≈3%	α-Al_2O_3 Cristobalite
1280	24 hrs.	0.25" dia. x 0.107" thick	0.218" x 0.100"	12.8% (dia) 6.5% (thickness)	α-Al_2O_3 Cristobalite

Table VII. Summary of Phase Compositions in Undercooled 60 wt% Al_2O_3- 40 wt% SiO_2 Melts.

Sample #	T_H(°C±10)	T_U(°C±10)	Composition	
			Mullite wt% Al_2O_3	Glass wt% Al_2O_3
60-Q	2090°C	Room Temp.	78.4	18.5
60-18	2090°C	1862(1-1/2hrs)	77.8	18.5
60-17	2090°C	1725(1-1/2hrs)	78.4	17.8
60-15	2090°C	1500(1-1/2hrs)	78.0	18.0
60-13	2090°C	1325(1-1/2hrs)	76.1	20.7
60-12	2090°C	1220(1-1/2hrs)	76.0	19.5
60-10	2090°C	1025(1-1/2hrs)	75.9	20.0
60-9	2090°C	925(15mins)	77.6	18.0
60-9	2090°C	925(1-1/2hrs)	74.5	20.8
60-9	2090°C	925(5-1/2hrs)	73.7	22.5
60-9	2090°C	925(24hrs)	73.2	23.0
60-7	2090°C	730(1-1/2hrs)	74.9	20.9
60-6	2090°C	600(1-1/2hrs)	78.8	17.9

Table VIII. Summary of Phase Compositions in Pre-nucleated and Crystallized 60 wt% Al_2O_3-40 wt% SiO_2 Melts.

Sample #	Melt Homogenization Temp.(°C±10) (50-60mins)	Nucleation History	Time at Crystallization Temp. T_C = (1725°C±10)	Composition	
				Mullite wt% Al_2O_3	Glass wt% Al_2O_3
60-925	2090°C	925°C(15mins)	1-1/2hrs	76.0	16.0
60-17RR	2090°C	1725(1-1/2hrs) + Room Temp.	1-1/2hrs	75.5	16.0
60-15R	2090°C	1500°C(15mins)	1-1/2hrs	77.9	19.0
60QR	2090°C	Room Temp.	No Reheating	78.4	18.5
60QR-1	2090°C	Room Temp.	1-1/2hrs	76.5	18.9
60QR-5	2090°C	Room Temp.	5-1/2hrs	76.0	19.8
60QR-7	2090°C	Room Temp.	70 hrs	74.5	23.5

Table IX. Summary of Phase Compositions in Pre-nucleated and Crystallized 42 wt% Al_2O_3-58 wt% SiO_2 Melts.

Sample #	Melt Homogenization Temp. (°C±10) (50-60mins)	Nucleation History	Time at Crystallization Temp. T_C = (1725°C±10)	Composition	
				Mullite wt% Al_2O_3	Glass wt% Al_2O_3
42-15R	2090°C	1500(15min)	1-1/2hrs.	75.0	16.9
42-17RR	2090°C	1725(1-1/2hrs) + Room Temp.	1-1/2hrs.	74.5	19.6
42QR-1	2090°C	Room Temp.	1-1/2hrs.	73.5	16.0
42QR-5	2090°C	Room Temp.	5-1/2hrs.	73.2	15.6
42QR-18	2090°C	Room Temp.	18hrs.	73.8	16.2
42QR-110	2090°C	Room Temp.	110hrs.	73.5	16.4

FIGURE CAPTIONS

Fig. 1 Stable and metastable equilibria in the SiO_2-Al_2O_3 System (Ref. 12).

Fig. 2 Schematic free energy versus temperature plot illustrating the thermodynamic basis for stable and metastable phases.

Fig. 3 Relationship between free energy-composition plots and the phase diagram for a hypothetical binary system illustrating metastability.

Fig. 4 Construction of a liquid immiscibility region from free energy-composition plots in a hypothetical binary system.

Fig. 5 Temperature dependence of the nucleation and crystallization rates.

Fig. 6 Cell assembly for heat treatment experiments.

Fig. 7 Electron beam microprobe images showing distribution of molybdenum in heat treated crucible cross section.

Fig. 8 Activity coefficients (logarithmic) of 3:2 mullite plotted against mole fraction of mullite (Heat of fusion of mullite ≈16,000 cals/mole).

Fig. 9 Activity coefficients (logarithmic) of SiO_2 plotted against mole fraction of 3:2 mullite (Heat of fusion of mullite ≈16,000 cals/mole).

Fig. 10 Activity coefficients (logarithmic) of Al_2O_3 plotted against mole fraction of Al_2O_3 using SiO_2 and Al_2O_3 as components.

Fig. 11 Activity of Al_2O_3 versus mole fraction Al_2O_3; immiscibility is to be expected below 1100°C.

Fig. 12 Activity coefficients (logarithmic) of SiO_2 versus mole

fraction Al_2O_3.

Fig. 13 The α-test for SiO_2-Al_2O_3 supercooled liquids (see equation 7).

Fig. 14 Variation of free energy of mixing with composition in the metastable SiO_2-3:2 mullite system (Heat of fusion of mullite ≈16,000 cals/mole.)

Fig. 15 Calculated liquid miscibility gaps superinposed on the phase diagram[12] of the SiO_2-Al_2O_3 system.

Fig. 16 Computer plotted compositions for the 23 wt% Al_2O_3-77 wt% SiO_2 glass composition determined by the electron beam microprobe.

Fig. 17 Transmission electron micrograph of glass in Fig. 16.

Fig. 18 Transmission electron micrograph of 42 wt% Al_2O_3-58 wt% SiO_2 glass.

Fig. 19 Metastable SiO_2-Al_2O_3 phase diagram and calculated liquid miscibility gap (corresponding to heat of fusion of mullite ≈27,000 cals/mole superimposed on the stable phase diagram.[12]

Fig. 20 Microstructure of 60 wt% Al_2O_3 melt undercooled to 1862°C after homogenization at 2090°C.

Fig. 21 Microstructures obtained on undercooling a homogenized 60 wt% Al_2O_3 melt to room temperature (60-Q), 1725°C (60-17), and 1500°C (60-15).

Fig. 22 Microstructures obtained on undercooling a homogenized 60 wt% Al_2O_3 melt to 1325°C (60-13), 1220°C (60-12) and 1025°C (60-10).

Fig. 23 Microstructures obtained on undercooling a homogenized 60 wt% Al_2O_3 melt to 925°C (60-9) and 730°C (60-7).

Fig. 24 Changes in compositions of the mullite and glass phases with heat treatment.

Fig. 25 Microstructure of a 60 wt% Al_2O_3 melt undercooled to 600°C after homogenization at 2090°C.

Fig. 26 Thermodynamic barrier to precipitation of stable phase until precursor reaction has occurred.

Fig. 27 Microstructure of a homogenized 60 wt% Al_2O_3 melt nucleated at 1500°C (15 minutes) and crystallized at 1725°C (1 $\frac{1}{2}$ hours).

Fig. 28 Microstructure of a homogenized 60 wt% Al_2O_3 melt treated at 925°C (15 minutes) and crystallized at 1725°C (1 $\frac{1}{2}$ hours).

Fig. 29 Computer plotted composition profile across the two phase structure of Fig. 28 determined by point beam electronmicroprobe.

Fig. 30 Microstructures obtained on nucleating a 42 wt% Al_2O_3 melt by quenching to room temperature and reheating to 1725°C (1 $\frac{1}{2}$ hours).

Fig. 31 Two mullite orientations by scanning electron fractography of 60 wt% Al_2O_3 melt quenched to room temperature, reheated to 1725°C (1 $\frac{1}{2}$ hours), and quenched to room temperature.

Fig. 32 Microstructure of 60 wt% Al_2O_3 melt quenched to room temperature and reheated to 1725°C (5 $\frac{1}{2}$ hours). (Magnification 640X).

Fig. 33 Changes in microstructure with heat treatment at 1725°C for 60 wt% Al_2O_3 melt nucleated at room temperature.

Fig. 34 Crystal growth of mullite in 42 wt% Al_2O_3 melt heat treated at 1725°C after room temperature quench, for 1 $\frac{1}{2}$ hours (42QR-1 $\frac{1}{2}$) and 5 $\frac{1}{2}$ hours (42QR-5 $\frac{1}{2}$).

Fig. 35 Mullite crystal growth by coalescence of finer mullite crystallites. (Fig. 34, 42-Q).

Fig. 36 Microstructures of a 60 wt% Al_2O_3 composition fired at 1700°C for 96 hours.

Fig. 37 Energy dispersive analysis of X-rays -(EDAX) images of the phases in Fig. 36.

Fig. 38 X-ray diffraction data for phases obtained in three mixtures of 60 wt% Al_2O_3 composition containing Al_2O_3 particles of three different sizes.

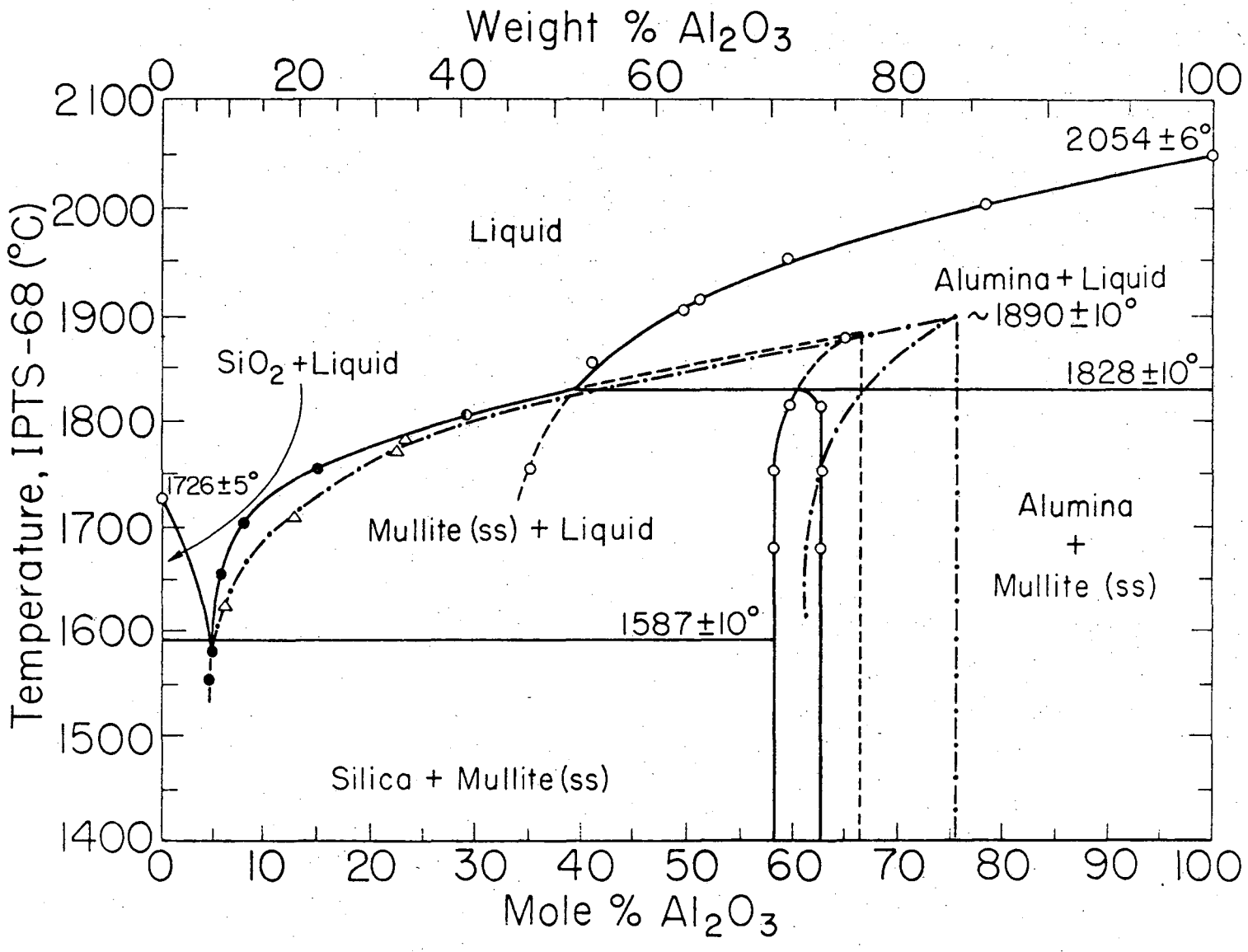

NBL 755-1377A
Fig. 1

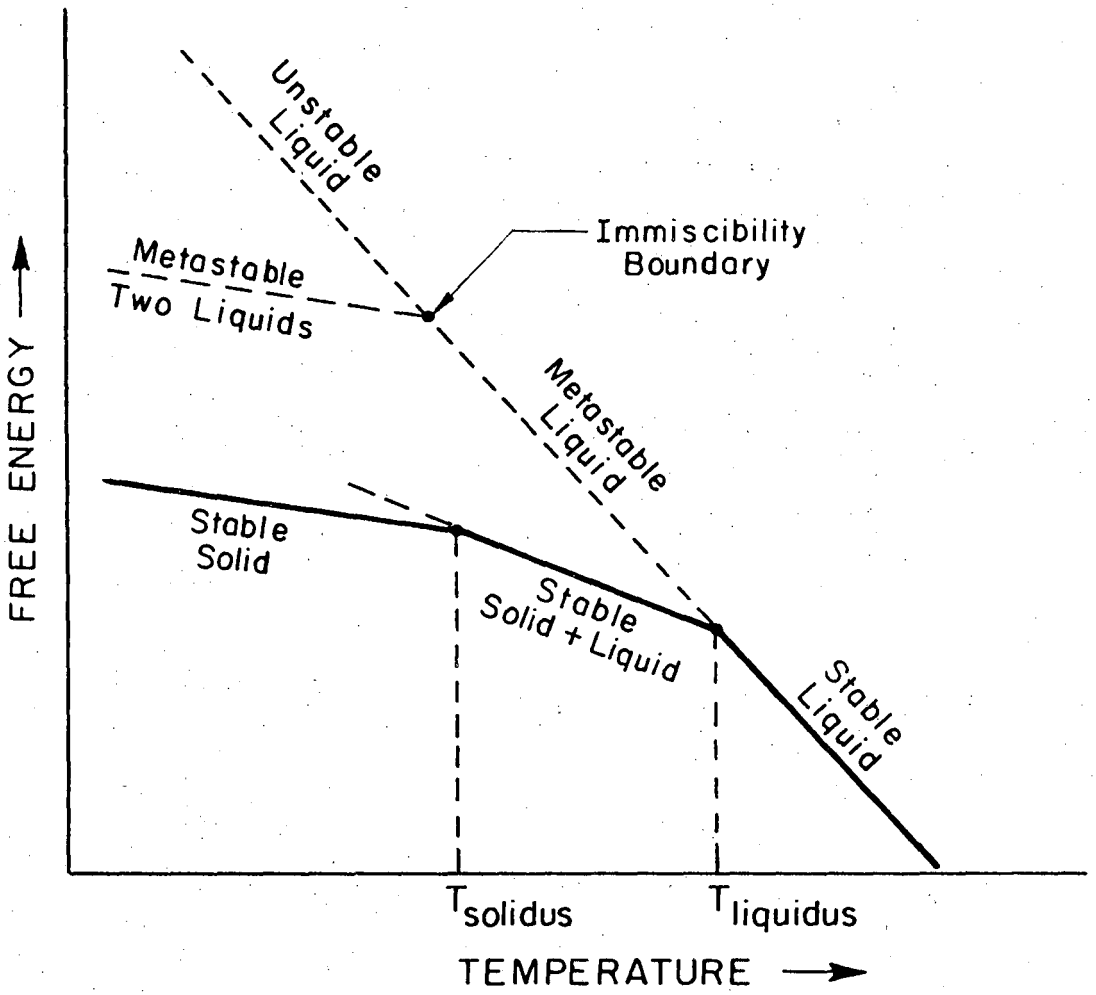

XBL 765-6811

Fig. 2

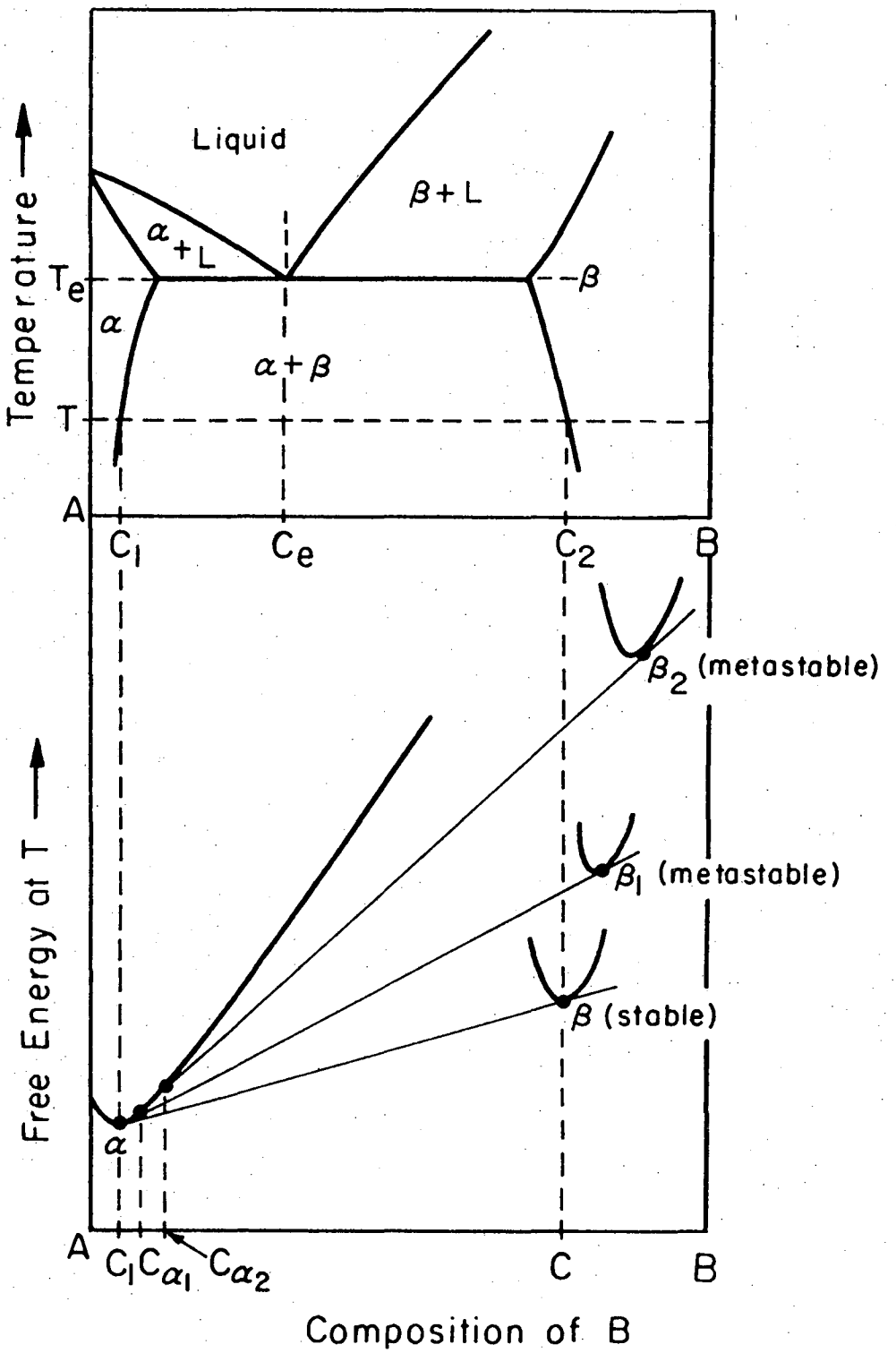

XBL 765-6812

Fig. 3

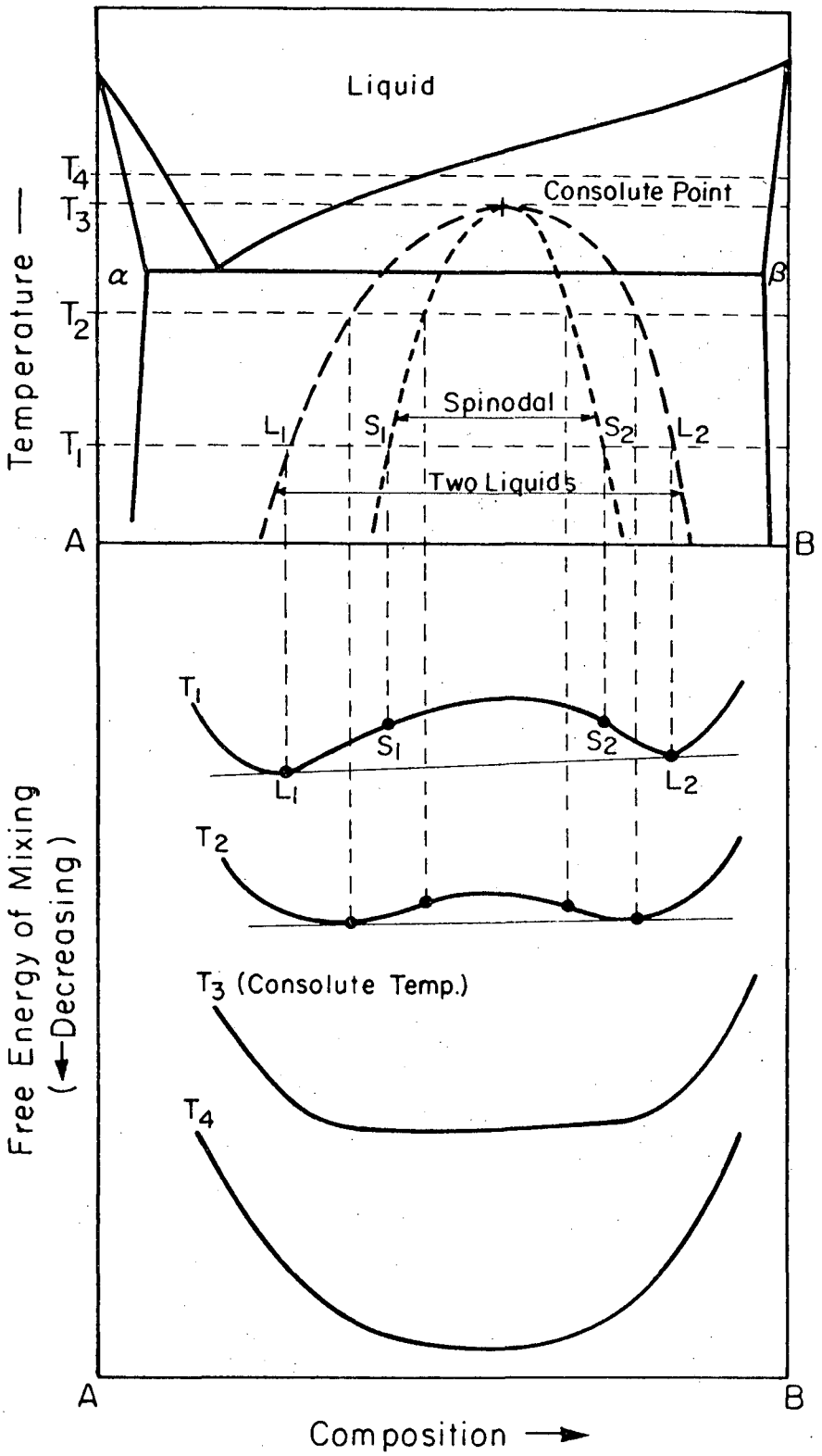

XBL765-6813

Fig. 4

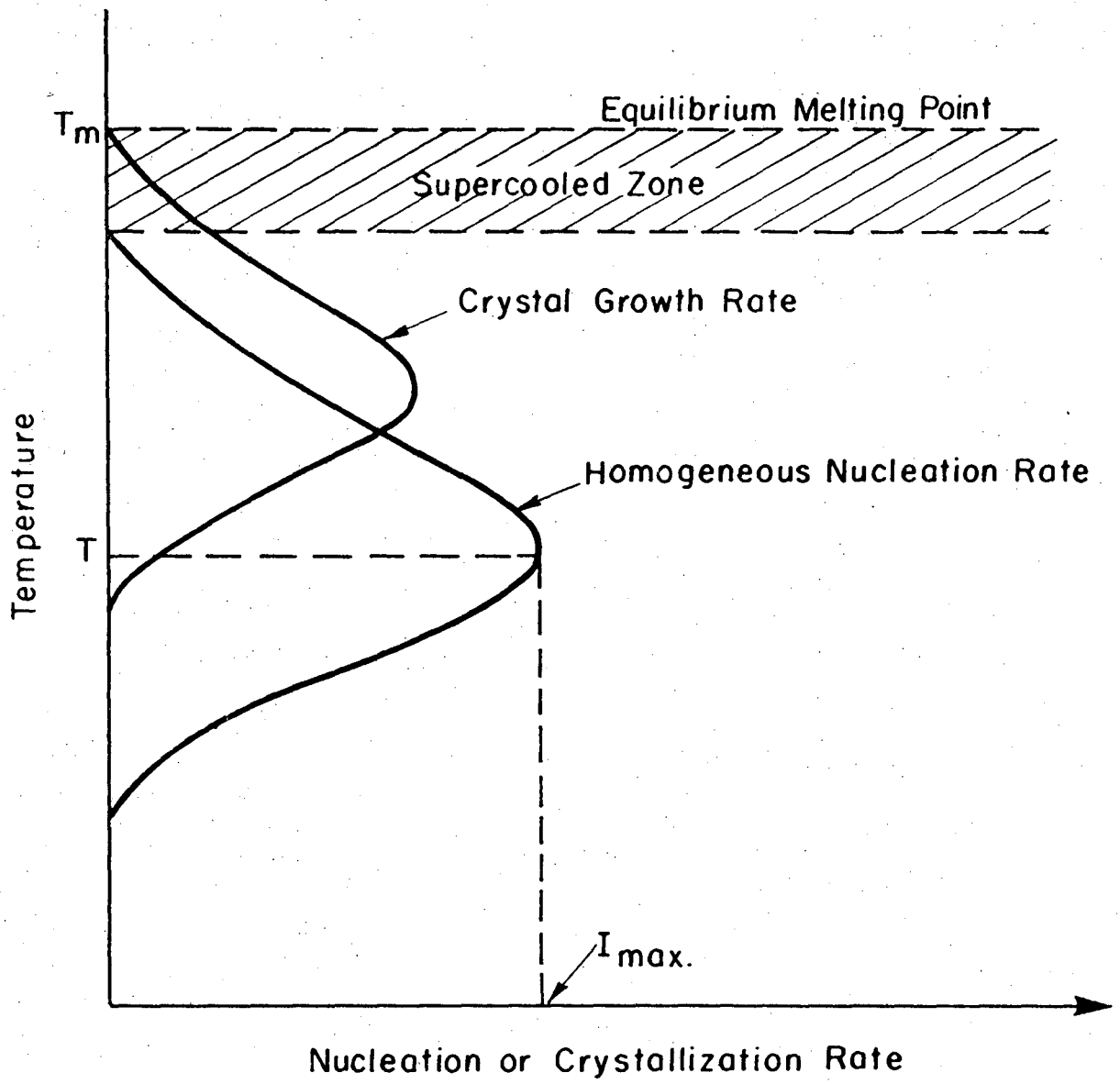

XBL 765-6885
Fig. 5

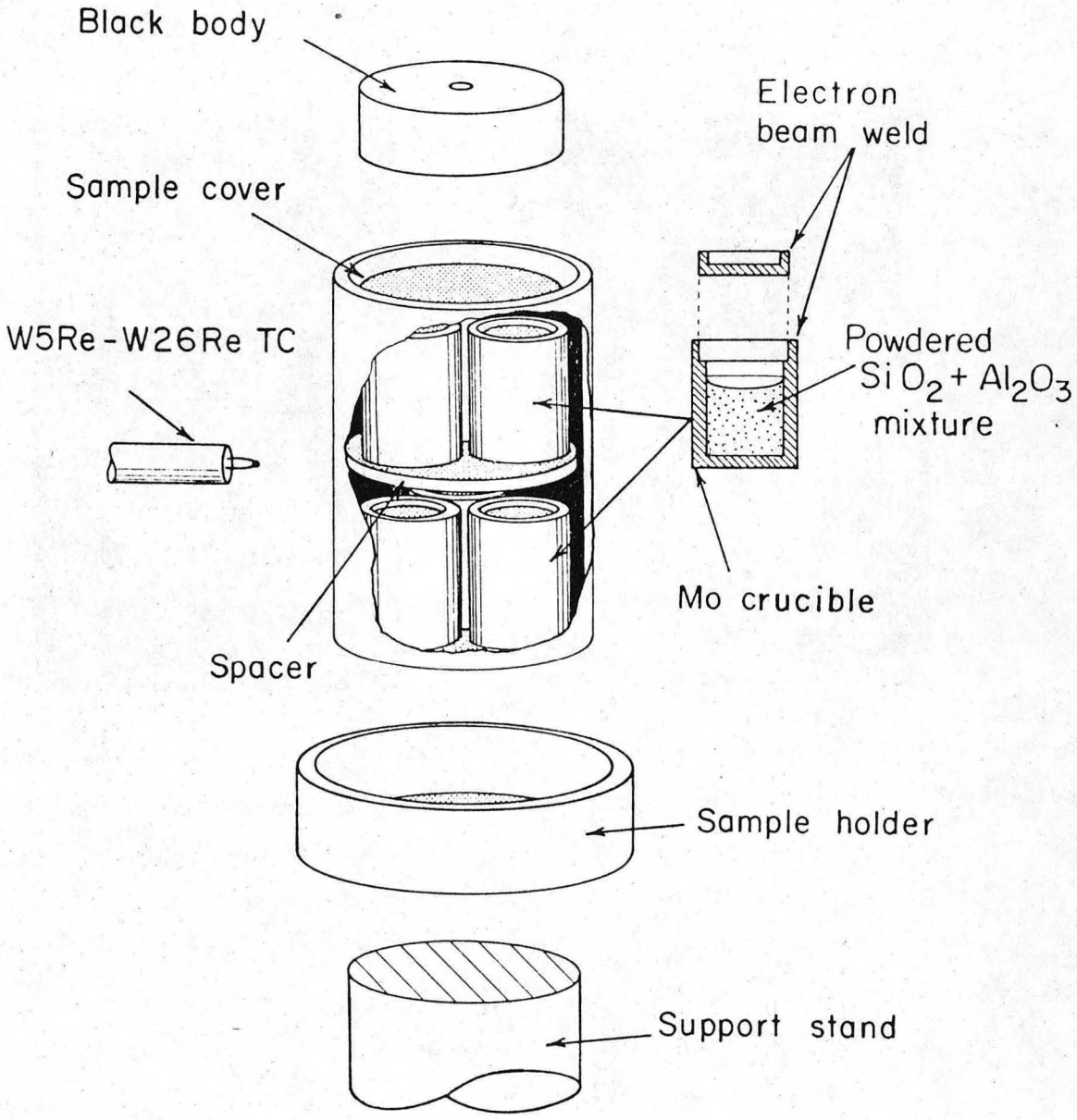

XBL 7210-4191B

Fig. 6

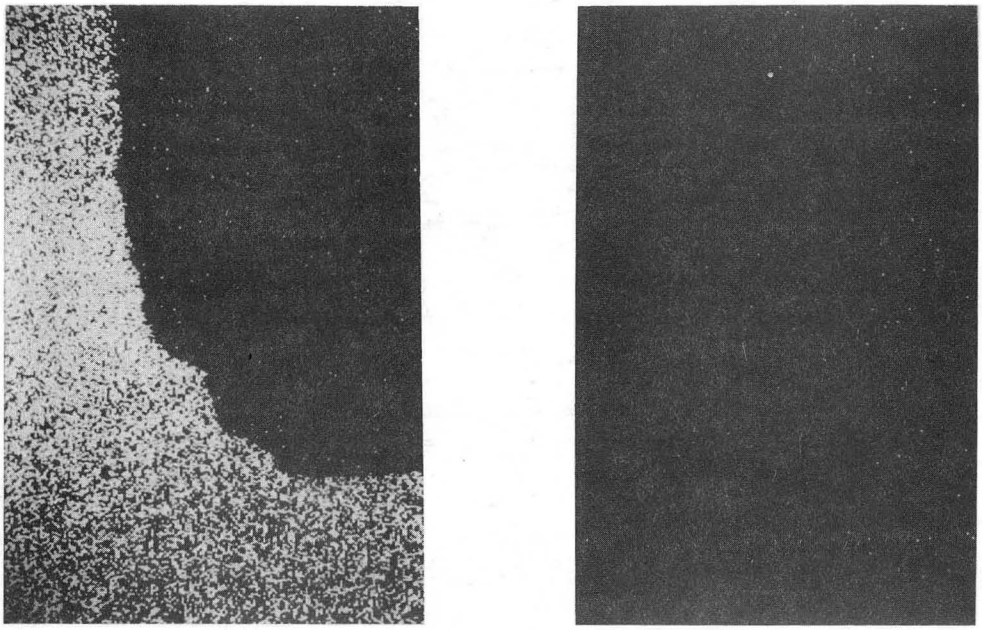

200 μm

XBB766-4827
Fig. 7

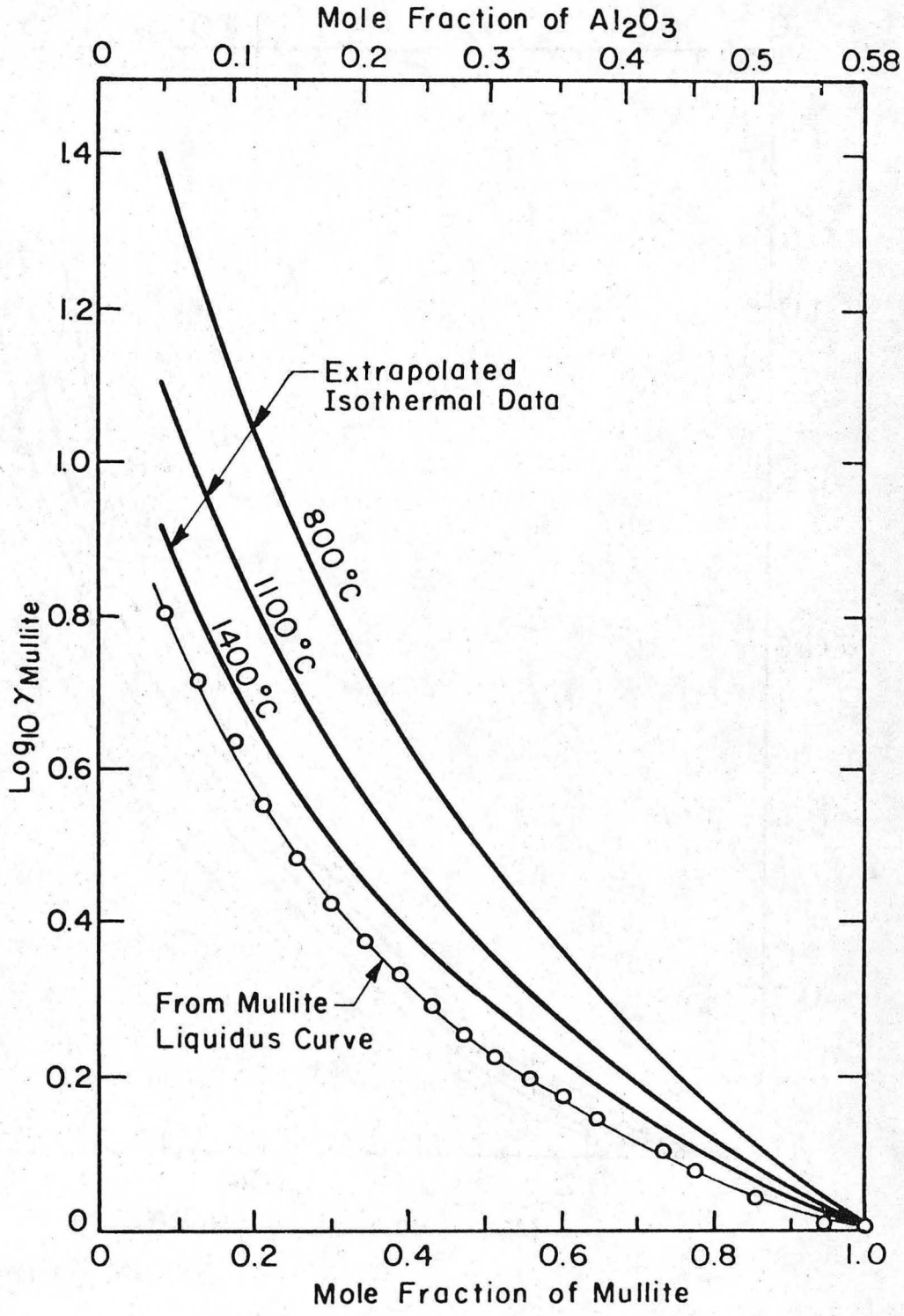

XBL 765-6814

Fig. 8

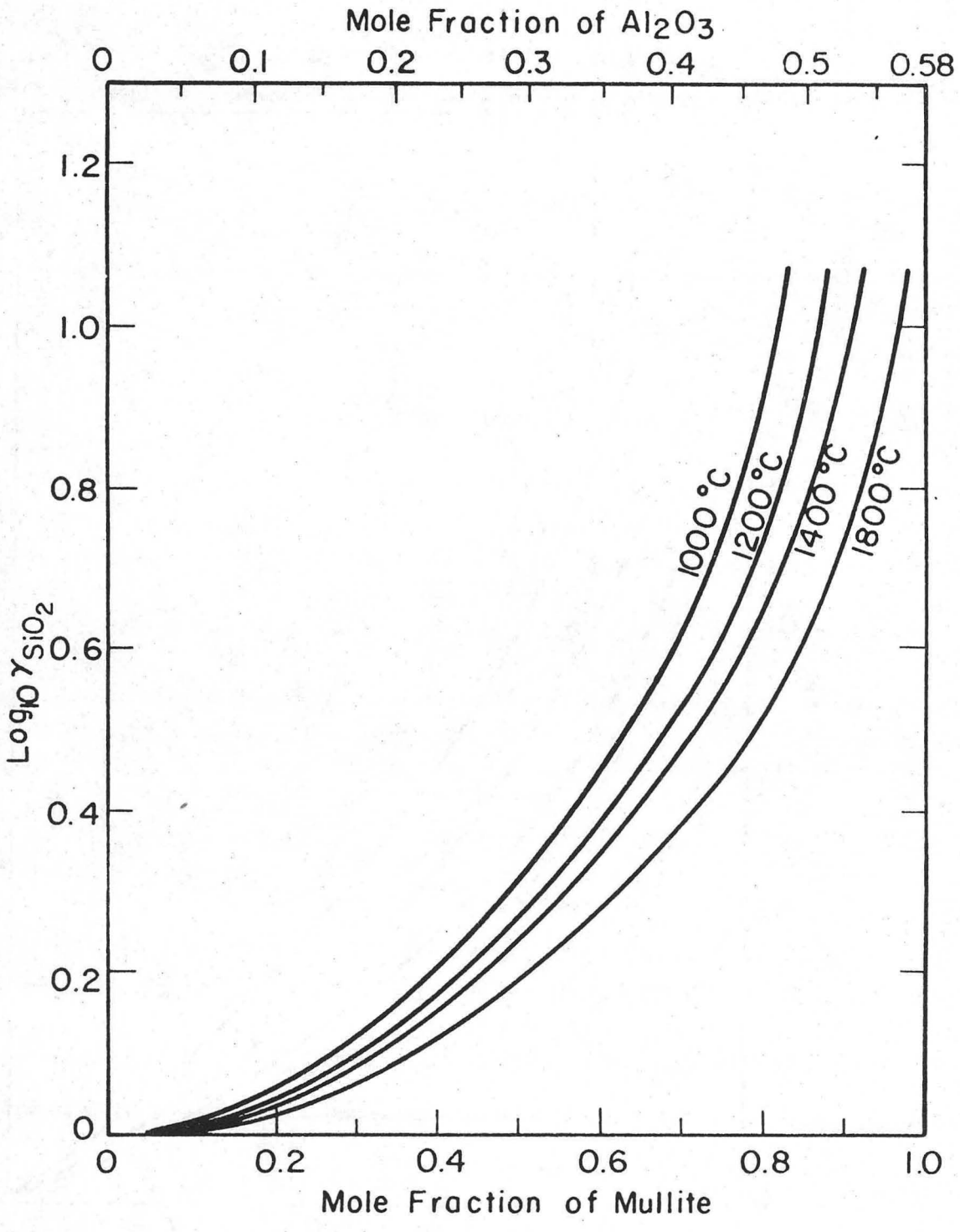

XBL 765-6815

Fig. 9

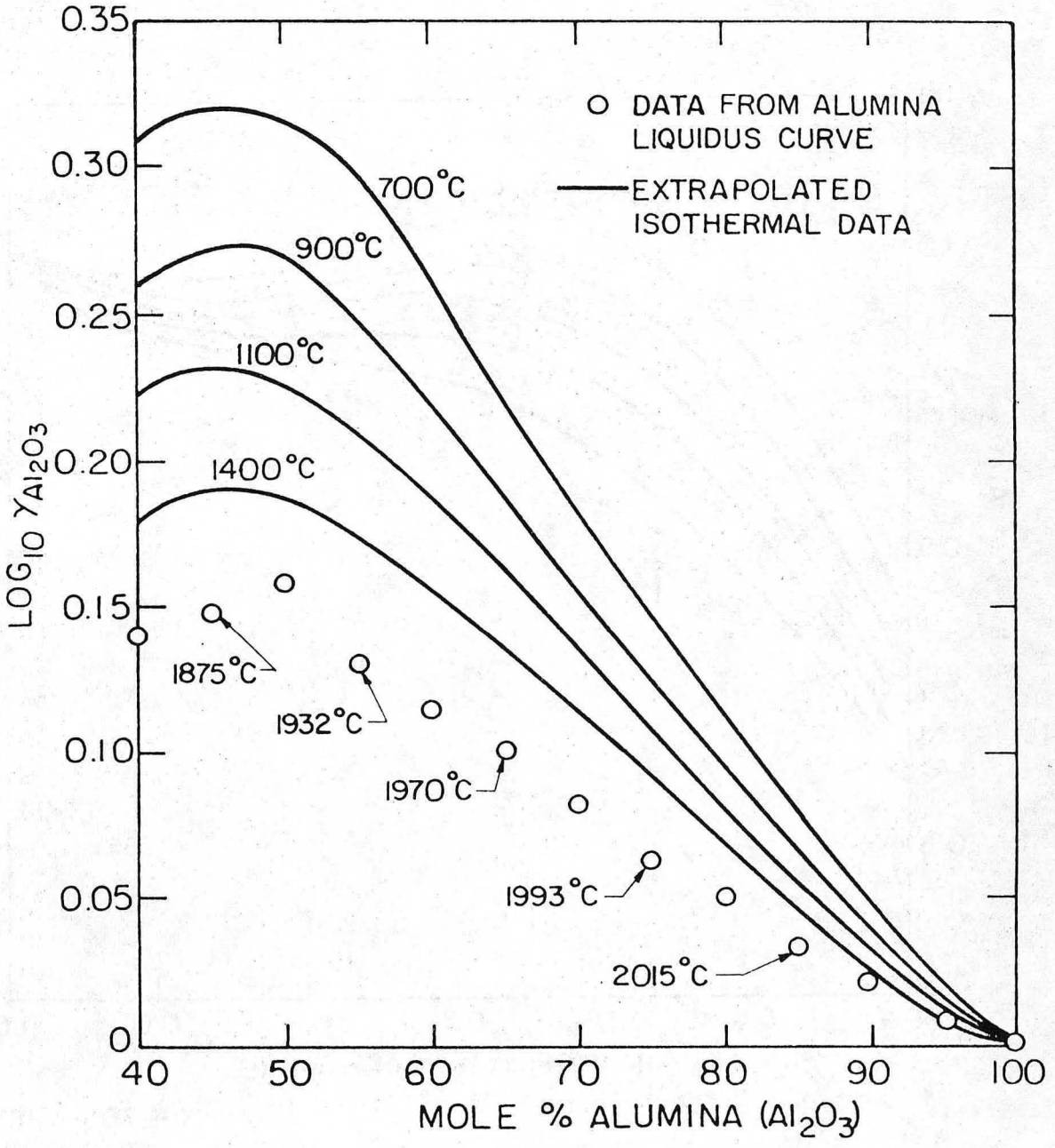

XBL 757-6822

Fig. 10

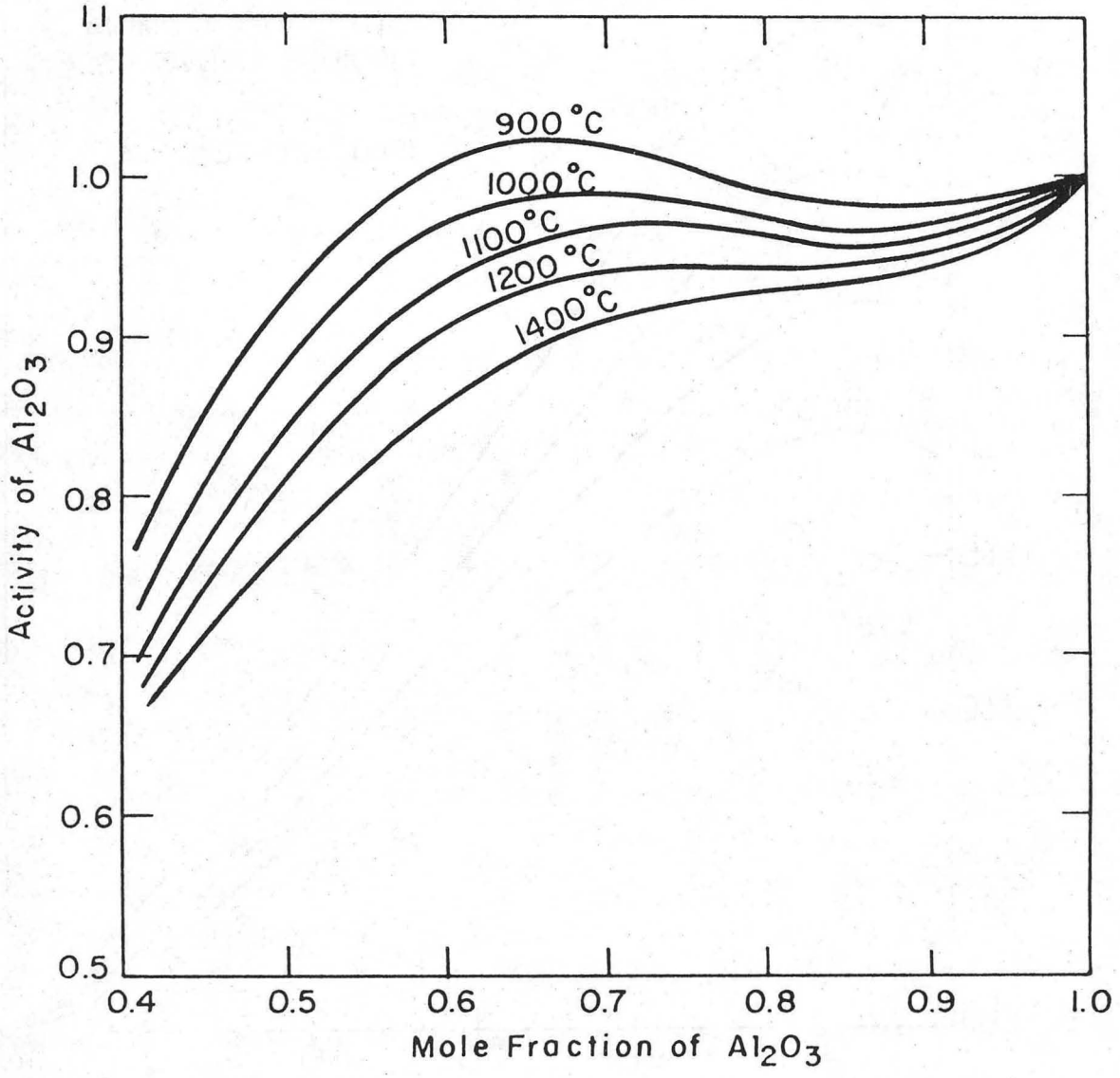

XBL 765-6888

Fig. 11

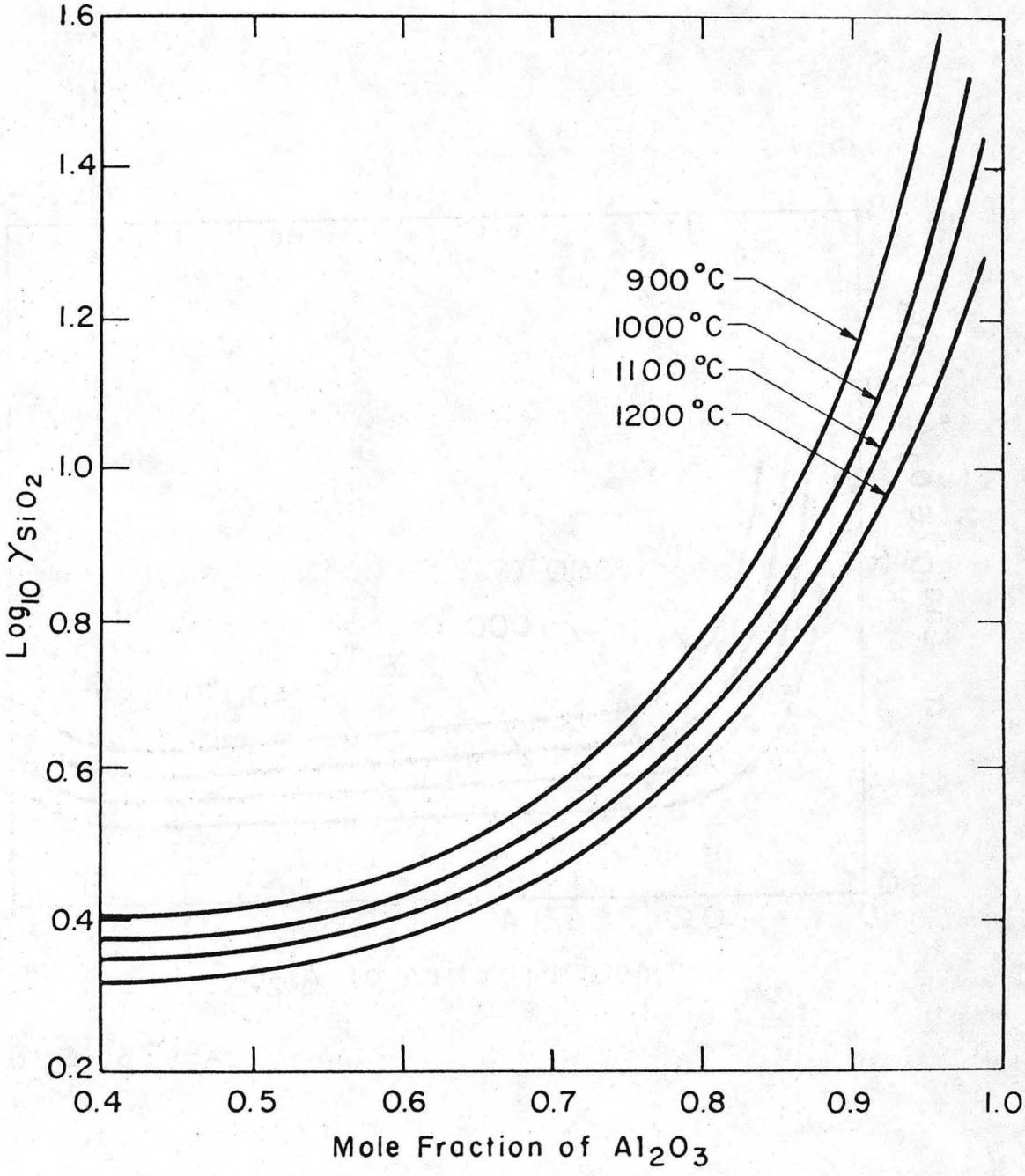

XBL 765-6886

Fig. 12

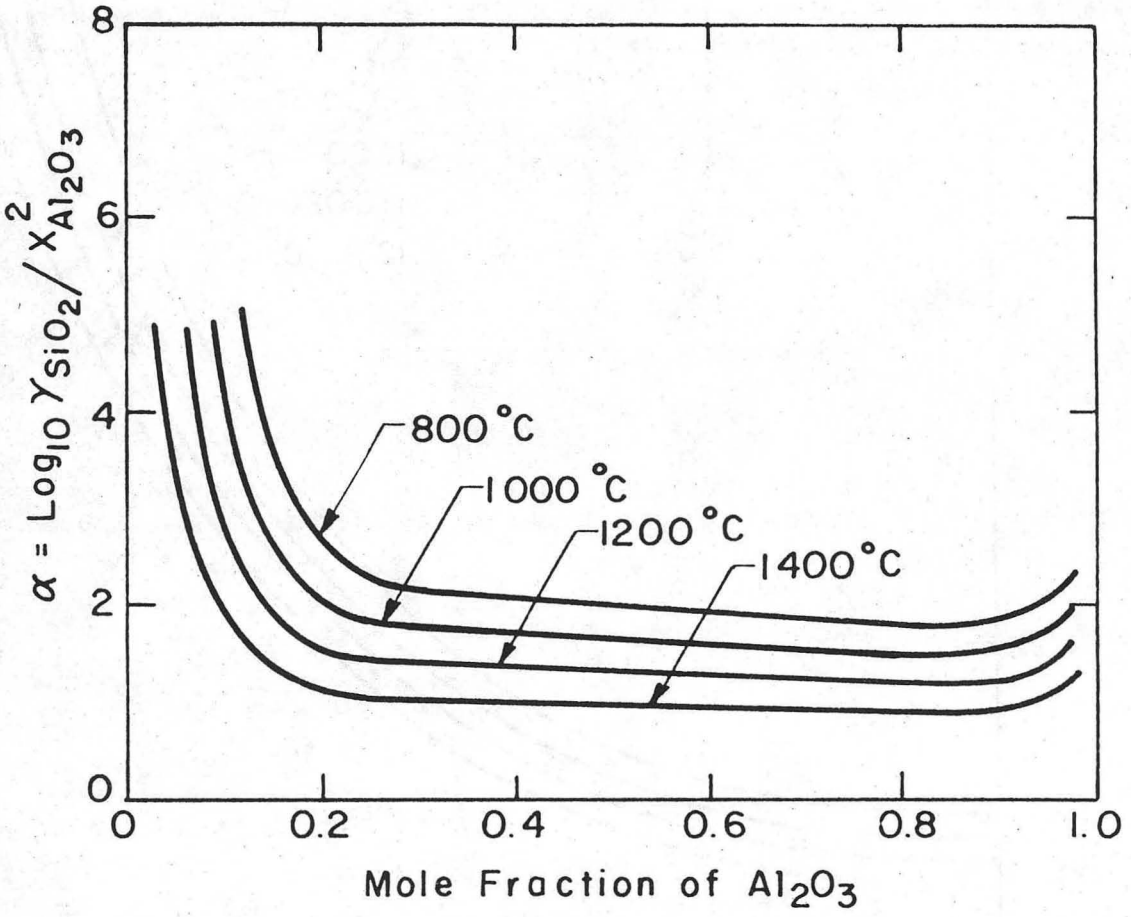

XBL765-6887

Fig. 13

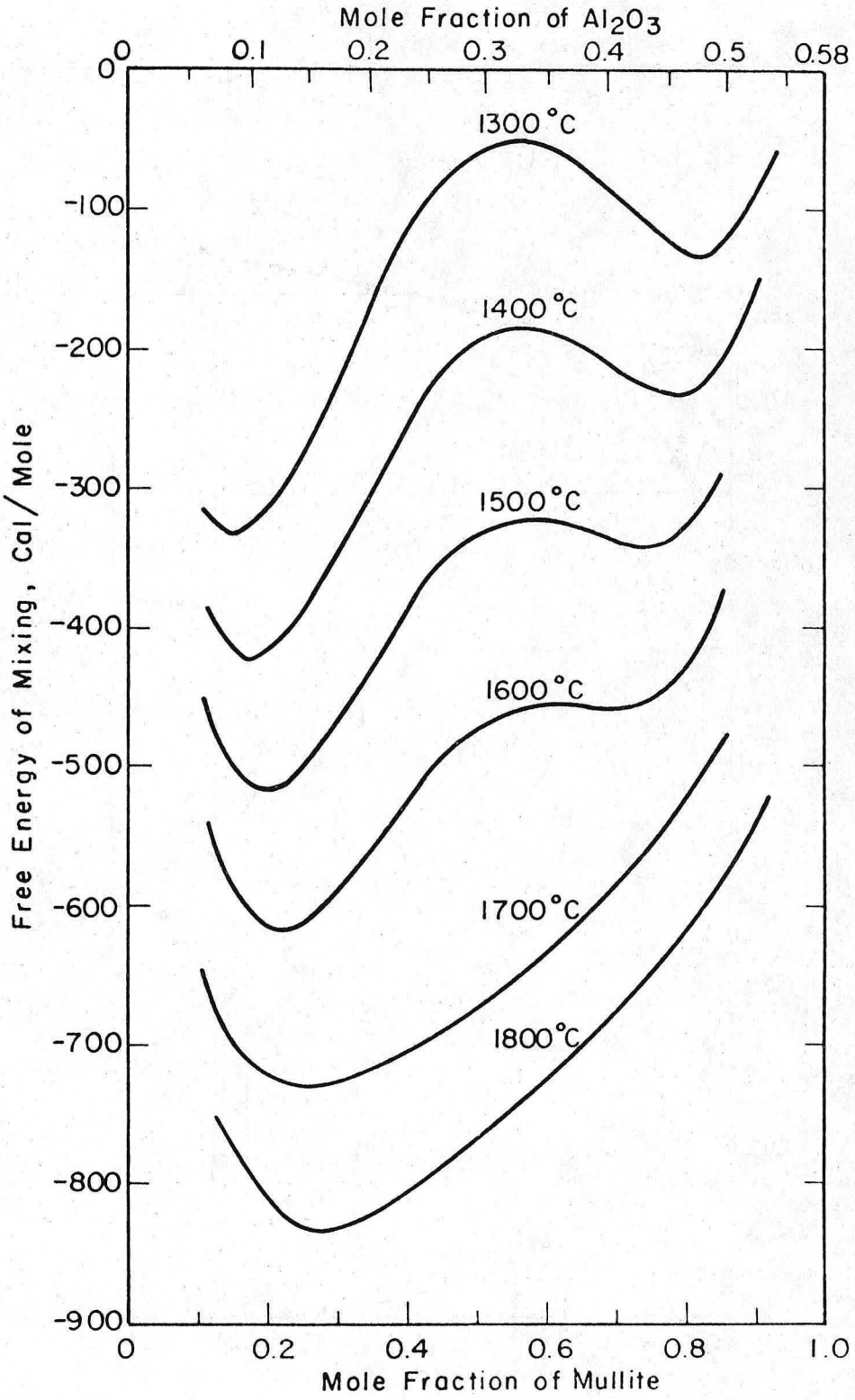

XBL 765-6816

Fig. 14

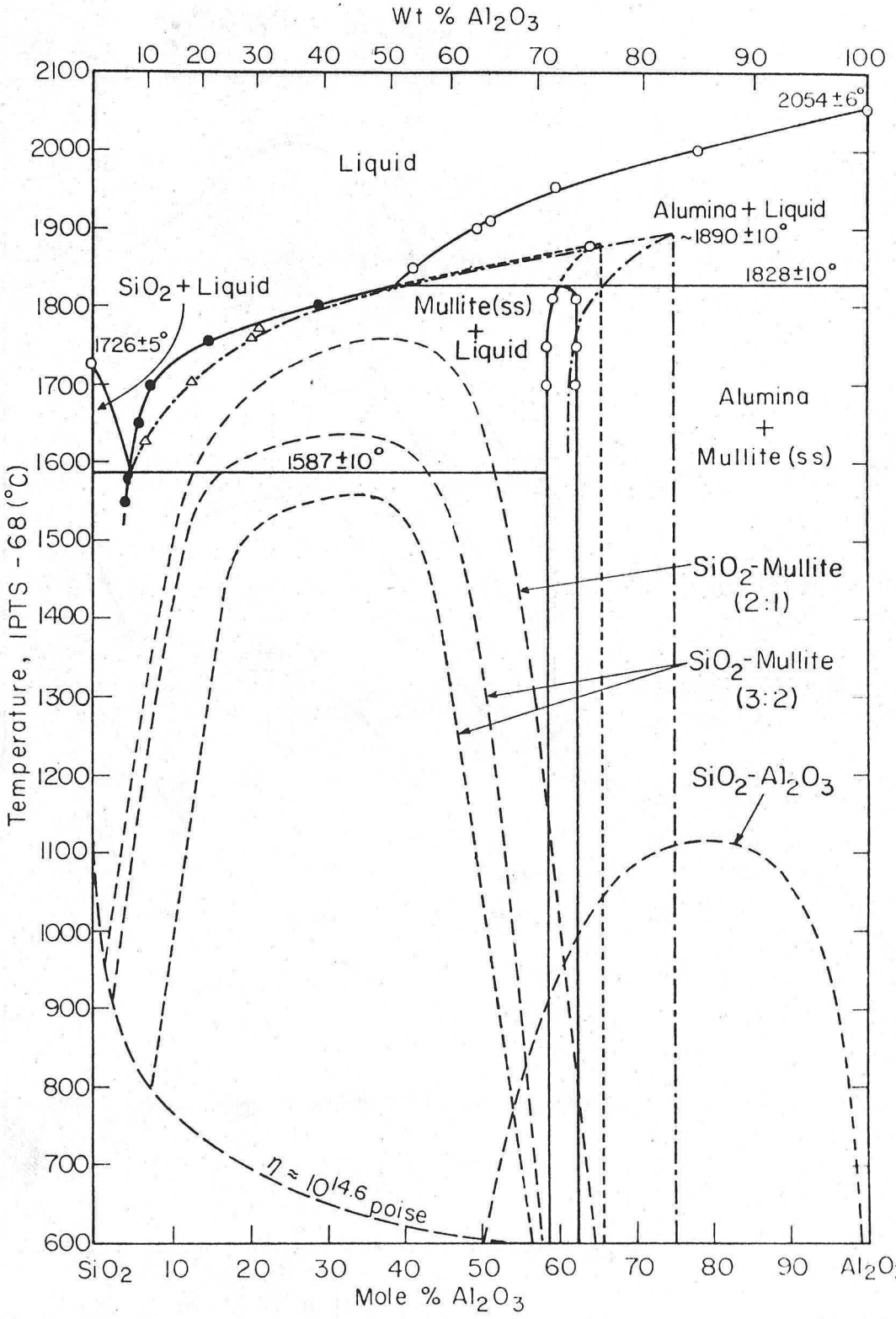

XBL 766-7008A

Fig. 15

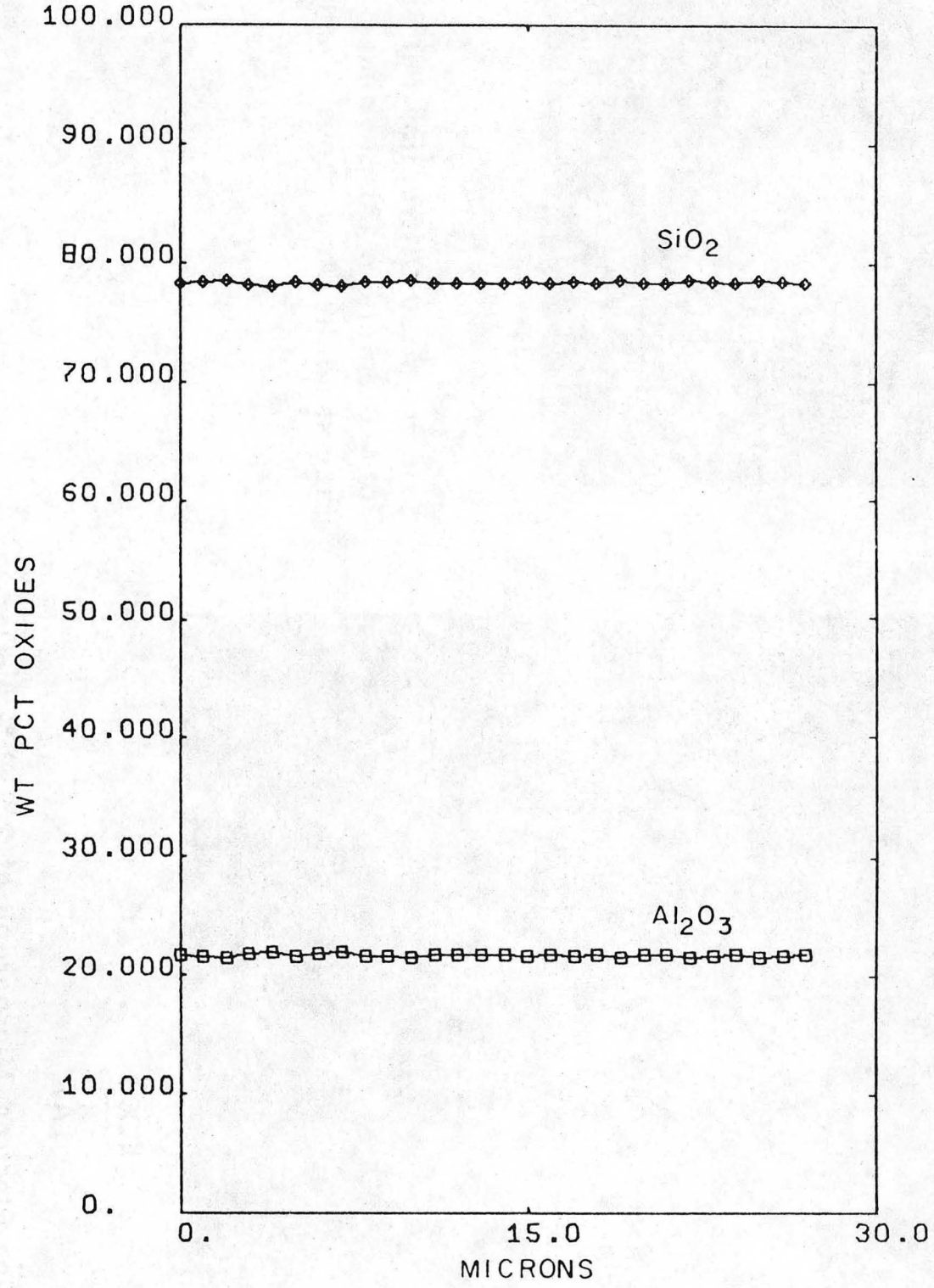

XBL 766 8075

Fig. 16

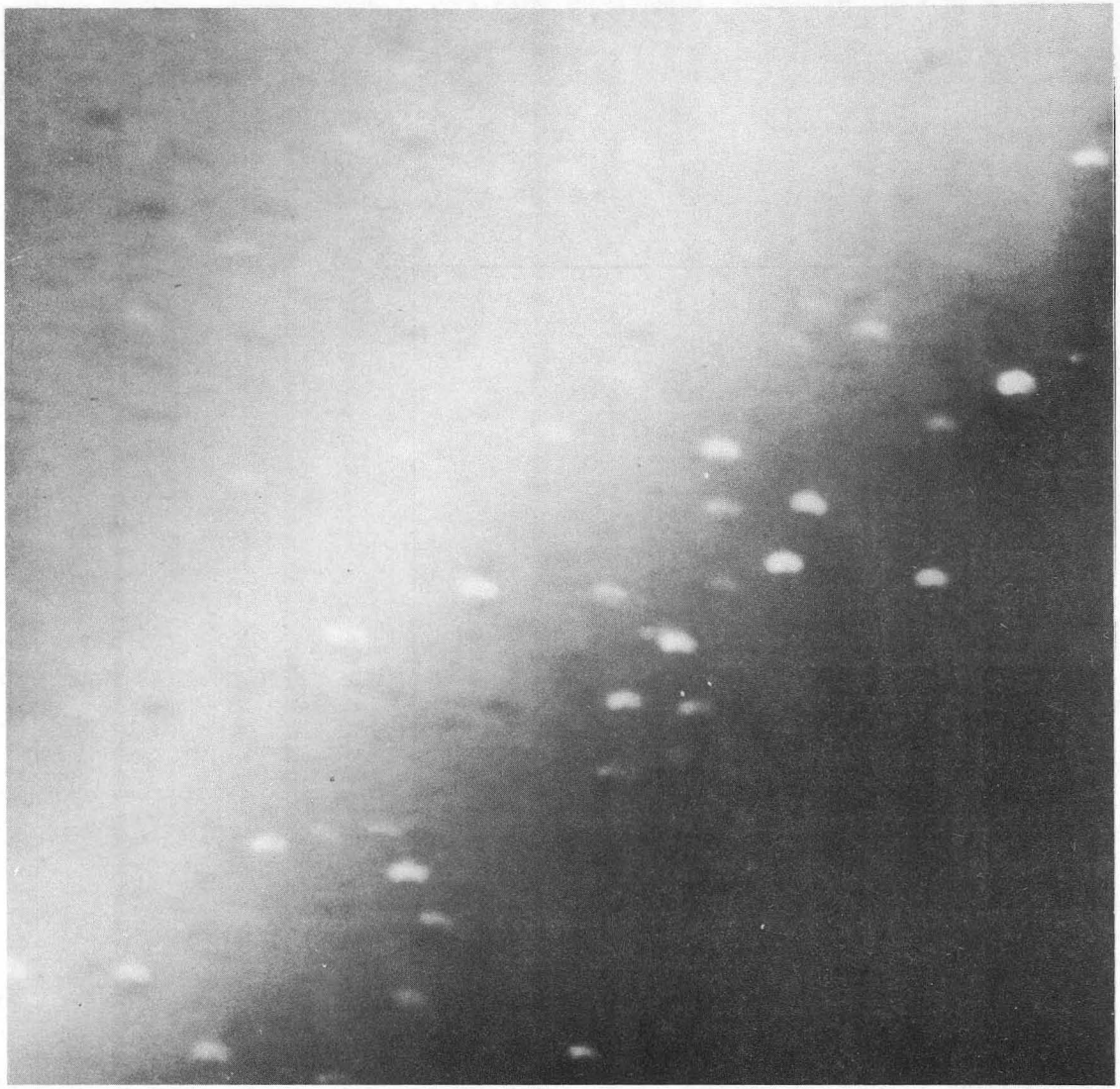

1000 Å

(A)

Direct Transmission Electron Micrograph of 23 wt. % Al_2O_3-77 wt. % SiO_2 Glass Showing Phase Separated Glassy Droplets ($\approx$ 400 Å) in a Glass Matrix.

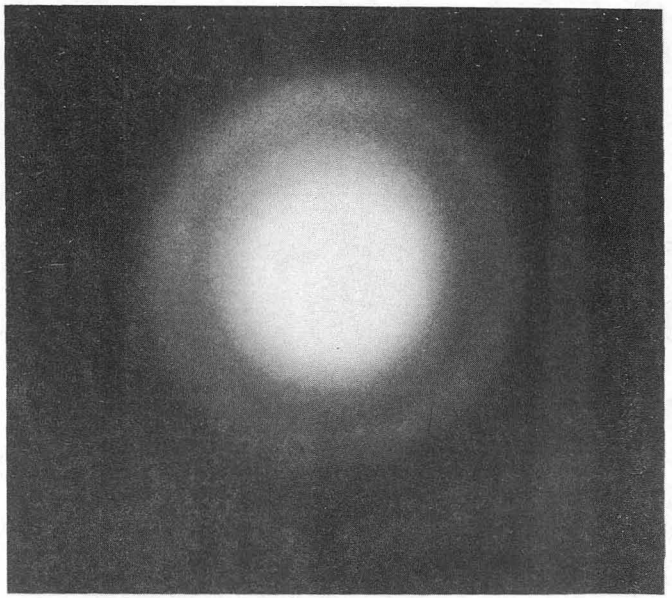

(B)

Selected Area Diffraction Pattern from Droplets in (A) Showing Predominantly Amorphous Structure.

XBB766-4825
Fig. 17

XBB7510-7484
Fig. 18

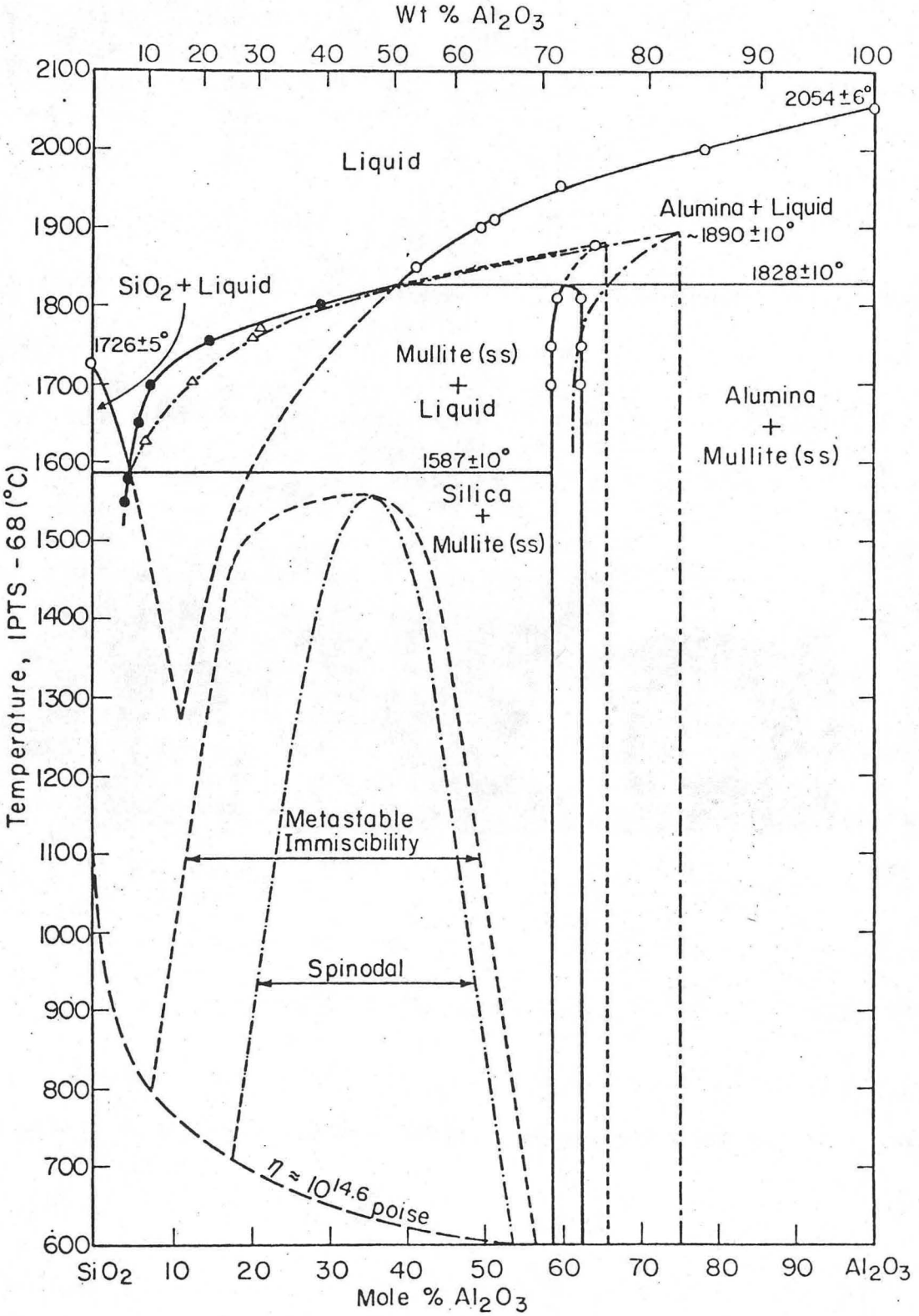

XBL 766-7008
Fig. 19

60 - 18

75 μm

MULLITE ≈ 78 WT. % Al_2O_3

GLASS ≈ 18.5 WT. % Al_2O_3

XBB766-5219
Fig. 20

60-Q

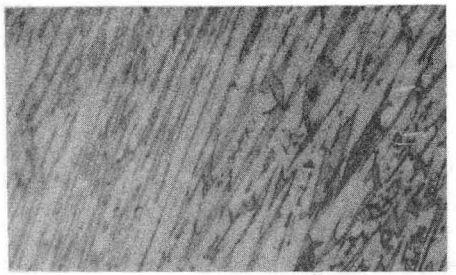

60-17

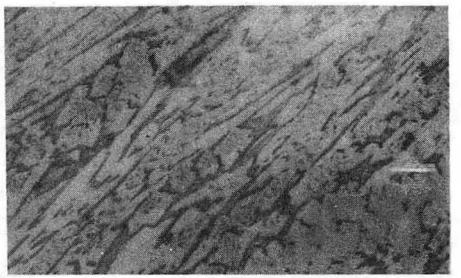

60-15

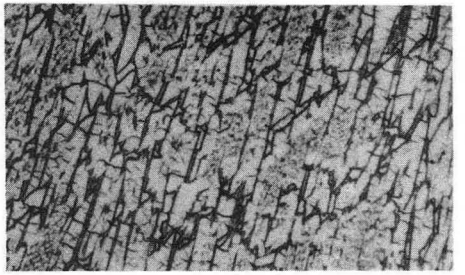

75 μm

MULLITE ≈ 78.5 WT. % Al_2O_3

GLASS ≈ 18.5 WT. % Al_2O_3

XBB766-5215
Fig. 21

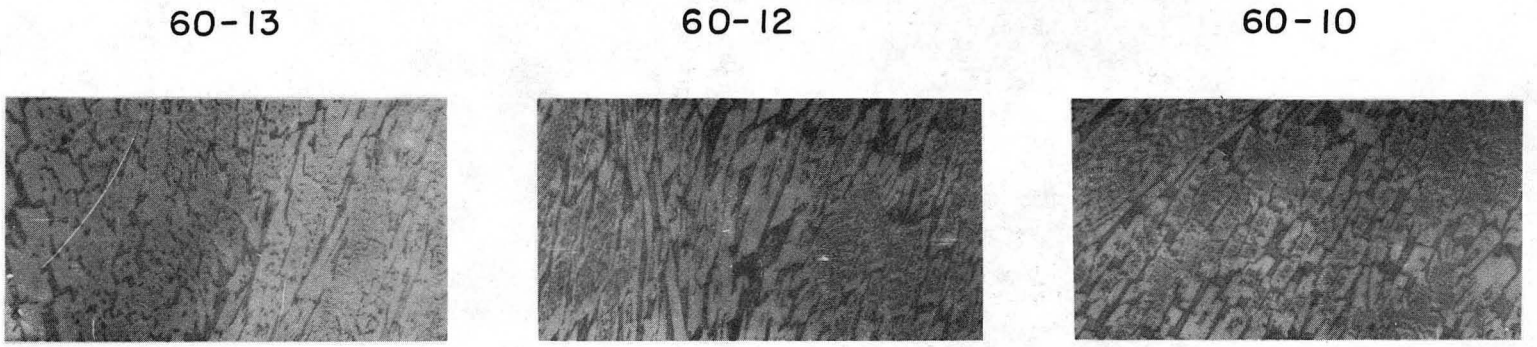

75 μm

MULLITE ≈ 76 WT.% Al_2O_3
GLASS ≈ 20 WT.% Al_2O_3

XBB766-5214
Fig. 22

60 - 9

60 - 7

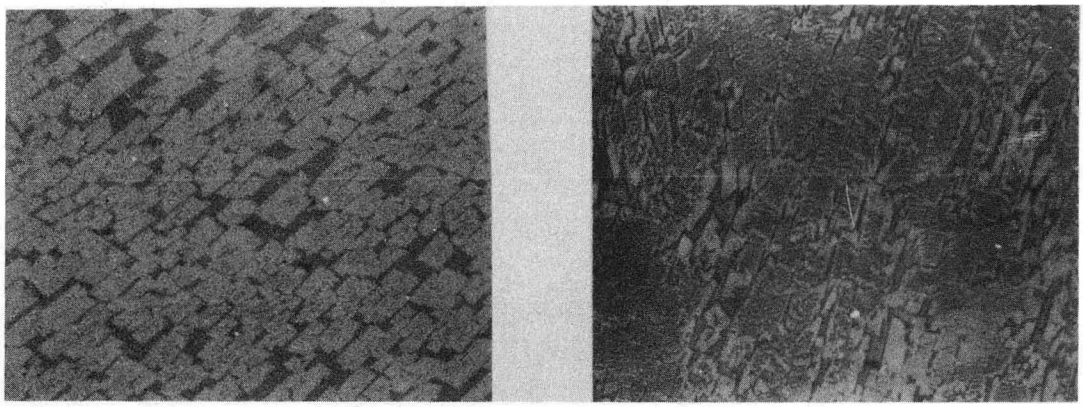

60 μm

MULLITE ≈ 74.5 WT. % Al_2O_3
GLASS ≈ 21 WT. % Al_2O_3

XBB766-5221
Fig. 23

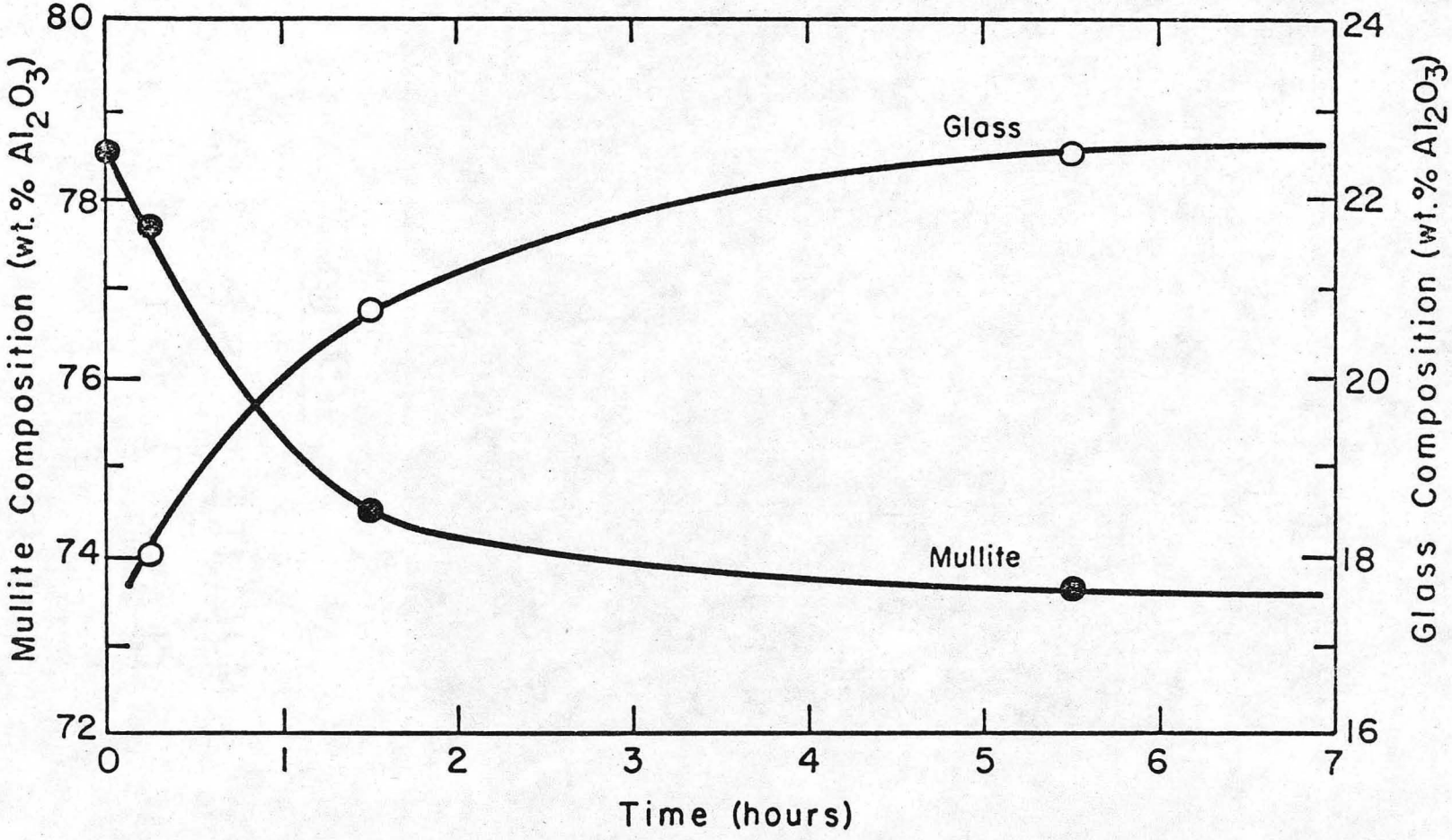

XBL 766-7009

Fig. 24

60 - 6

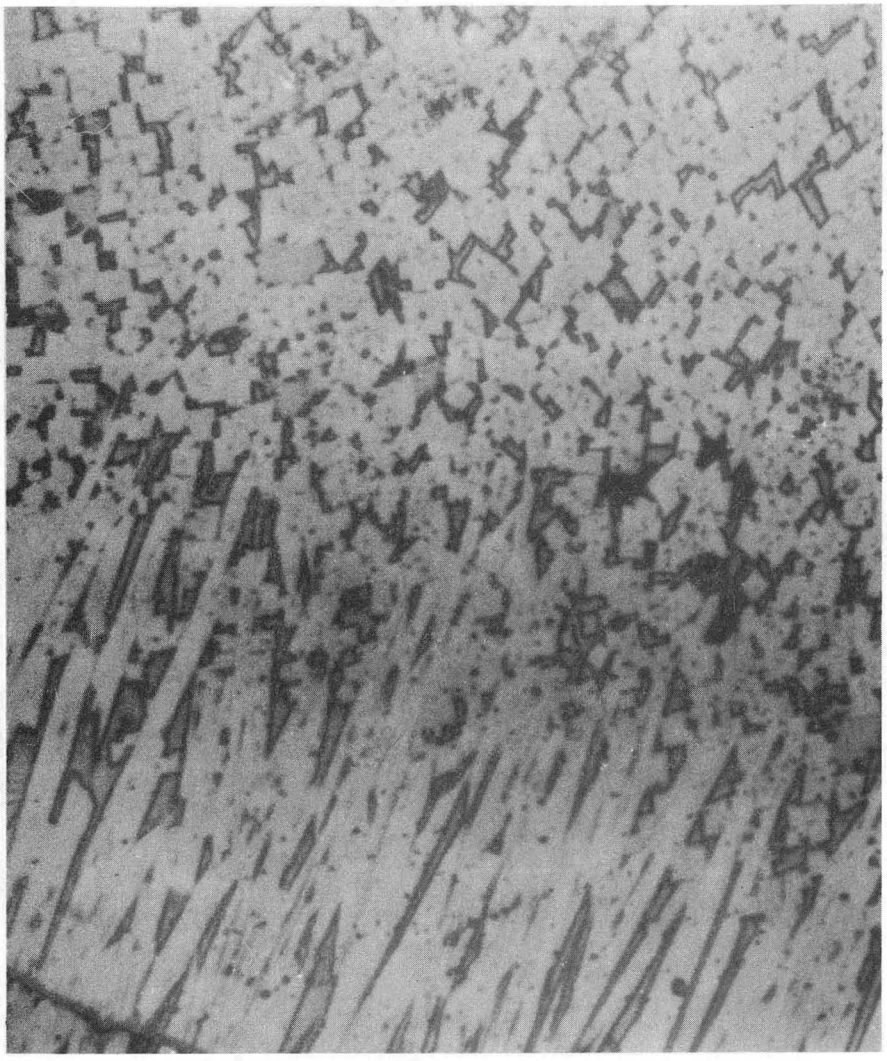

75 μm

MULLITE ≈ 78.8 WT. % Al_2O_3

GLASS ≈ 17.9 WT. % Al_2O_3

XBB766-5220
Fig. 25

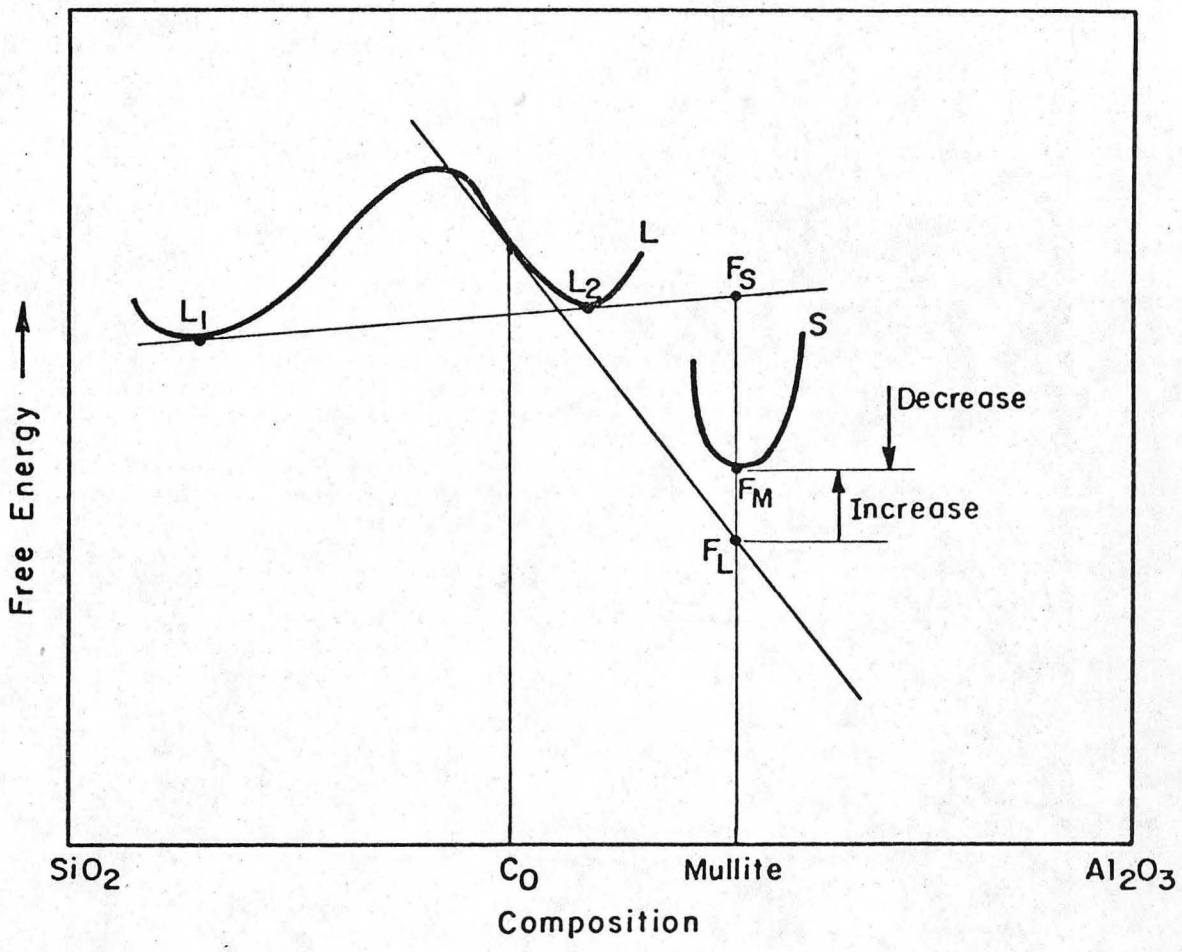

XBL 766-7010
Fig. 26

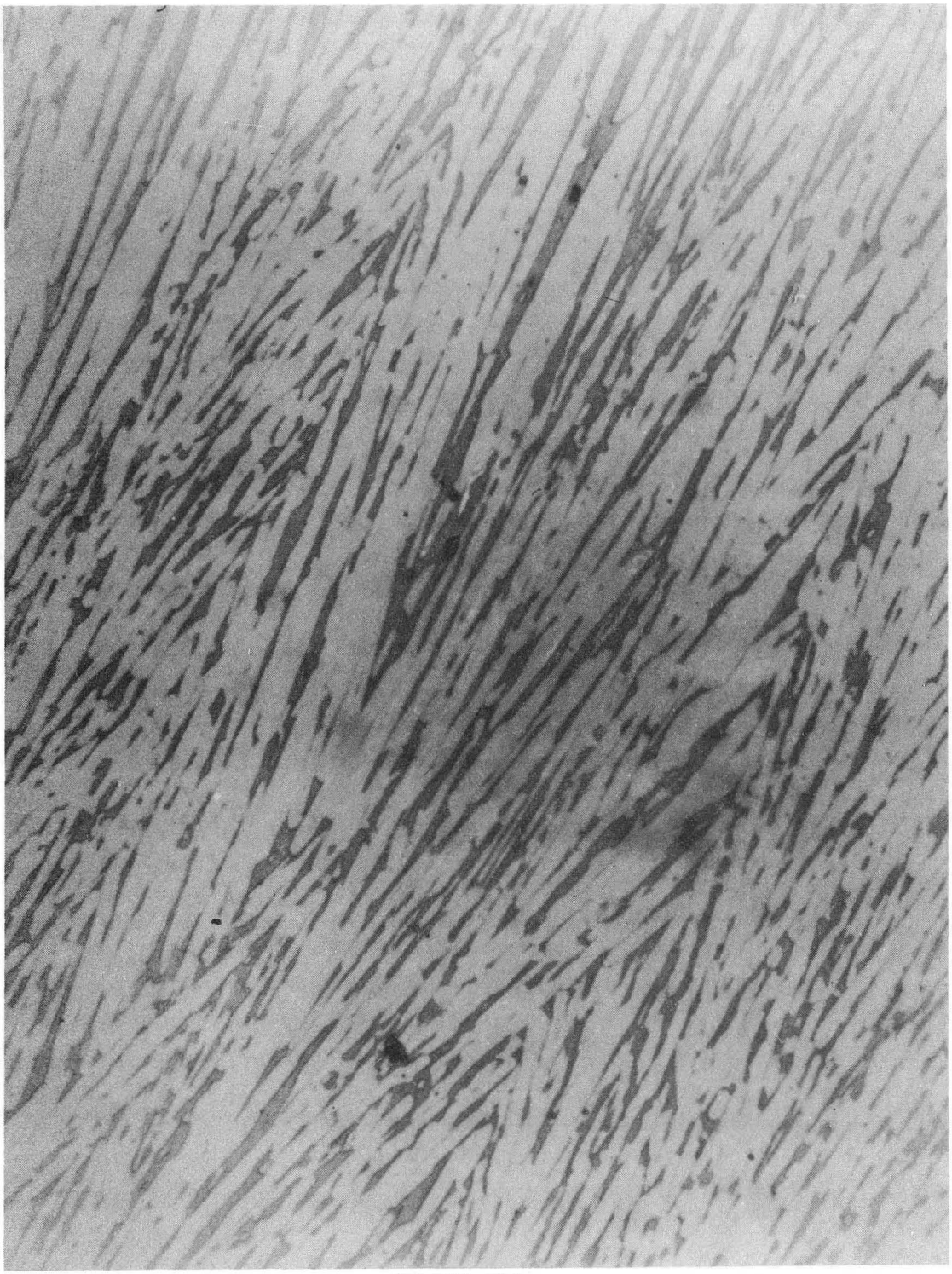

XBB766-5218
Fig. 27

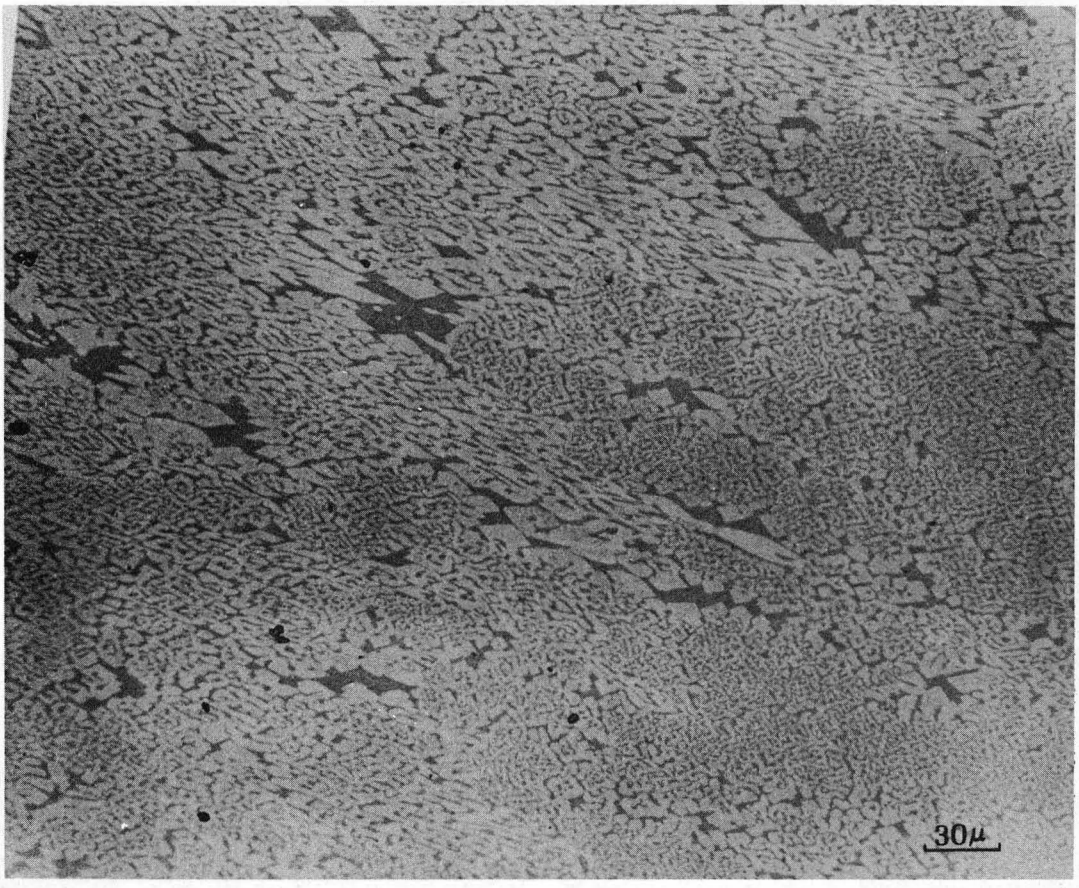

XBB7510-7486
Fig. 28

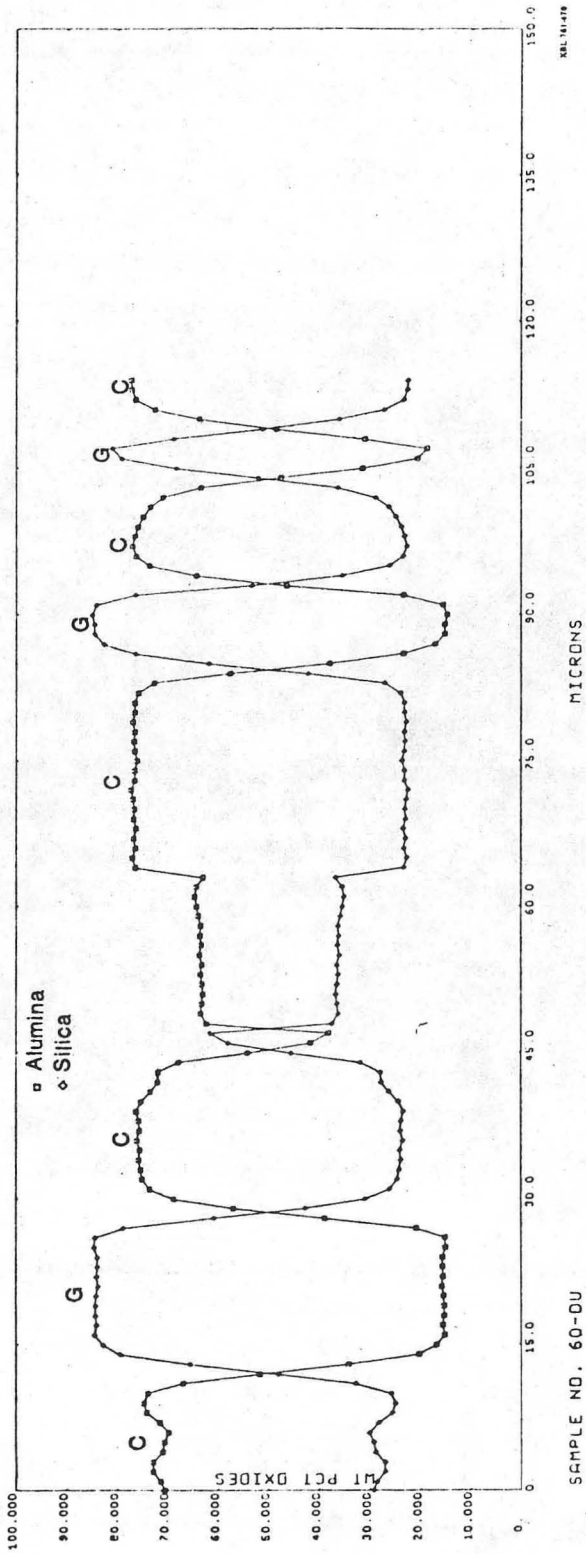

Fig. 29

42 wt% Al_2O_3 – 58 wt% SiO_2

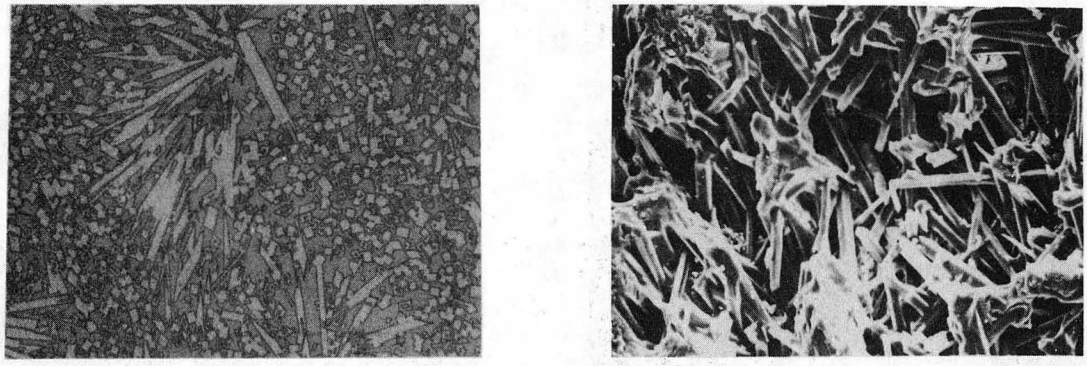

OPTICAL

S.E.M.

XBB762-1201
Fig. 30

60wt% Al_2O_3 + 40wt% SiO_2

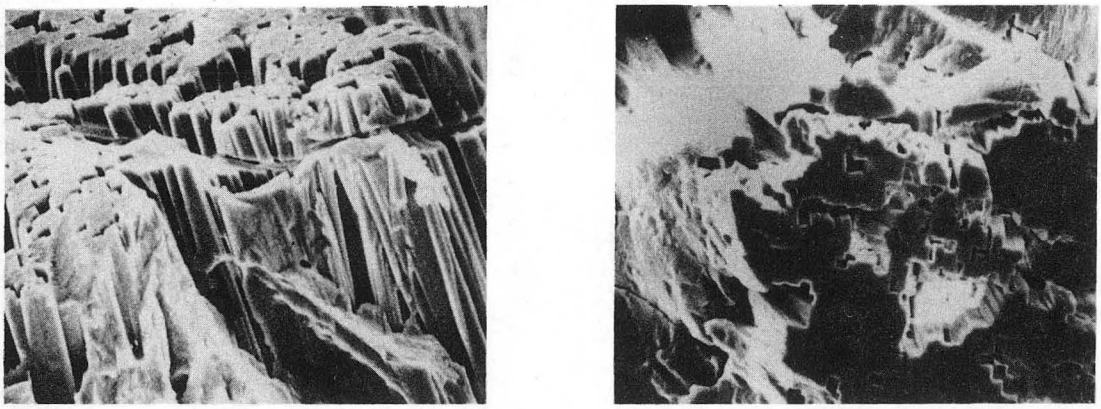

XBB762-1202
Fig. 31

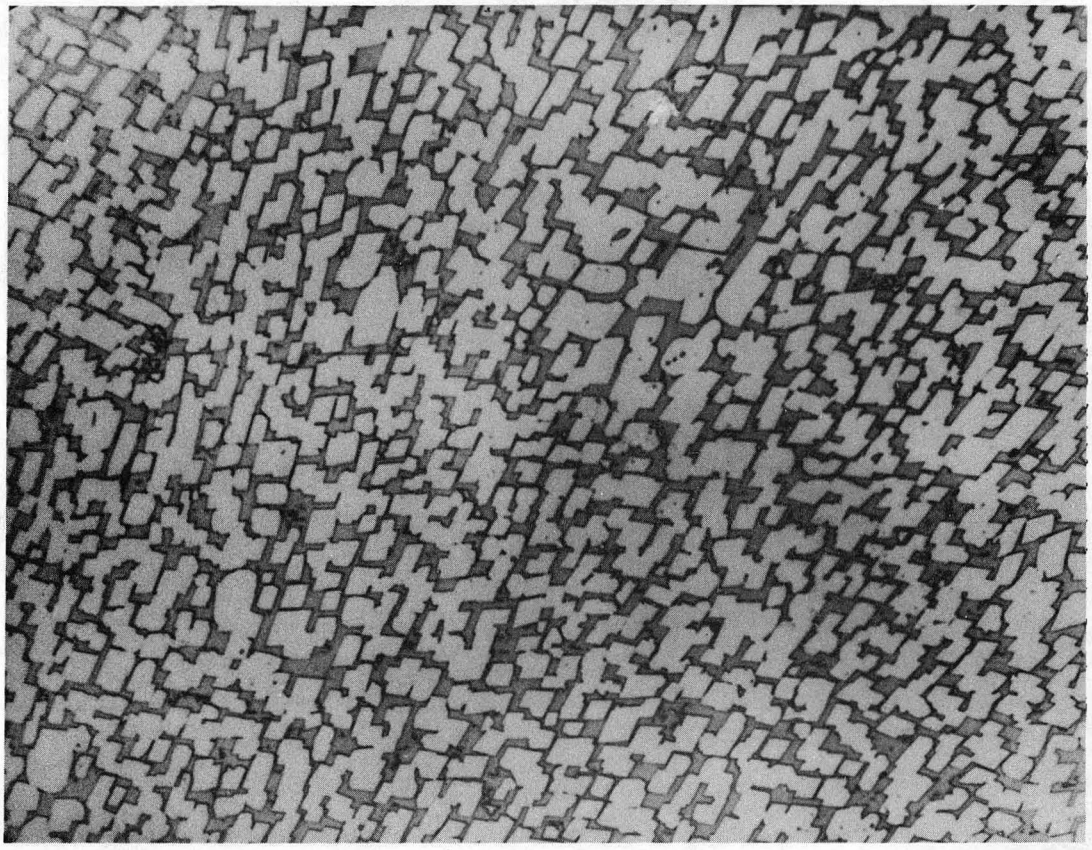

XBB766-4824
Fig. 32

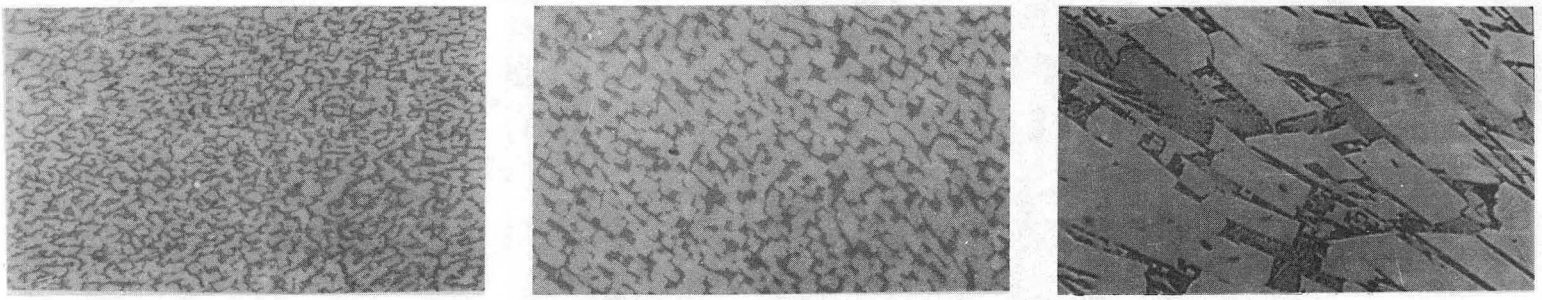

XBB766-5216
Fig. 33

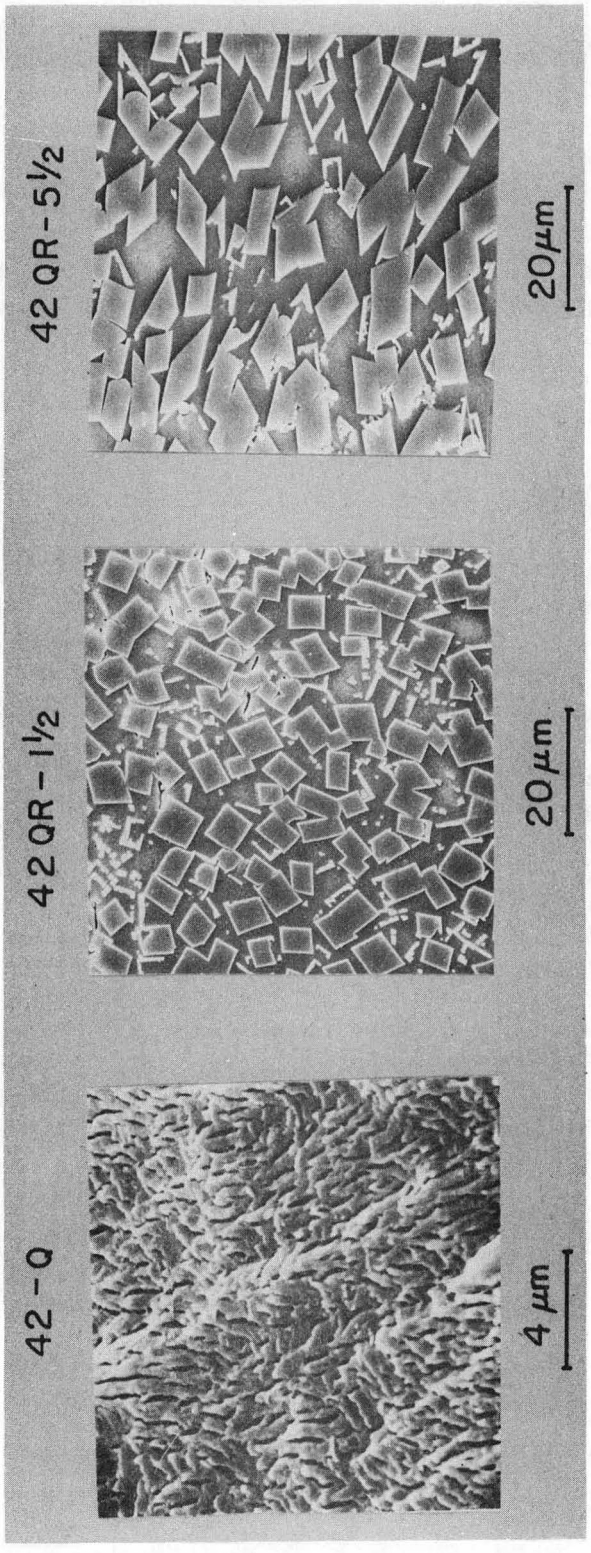

XBB766-5225
Fig. 34

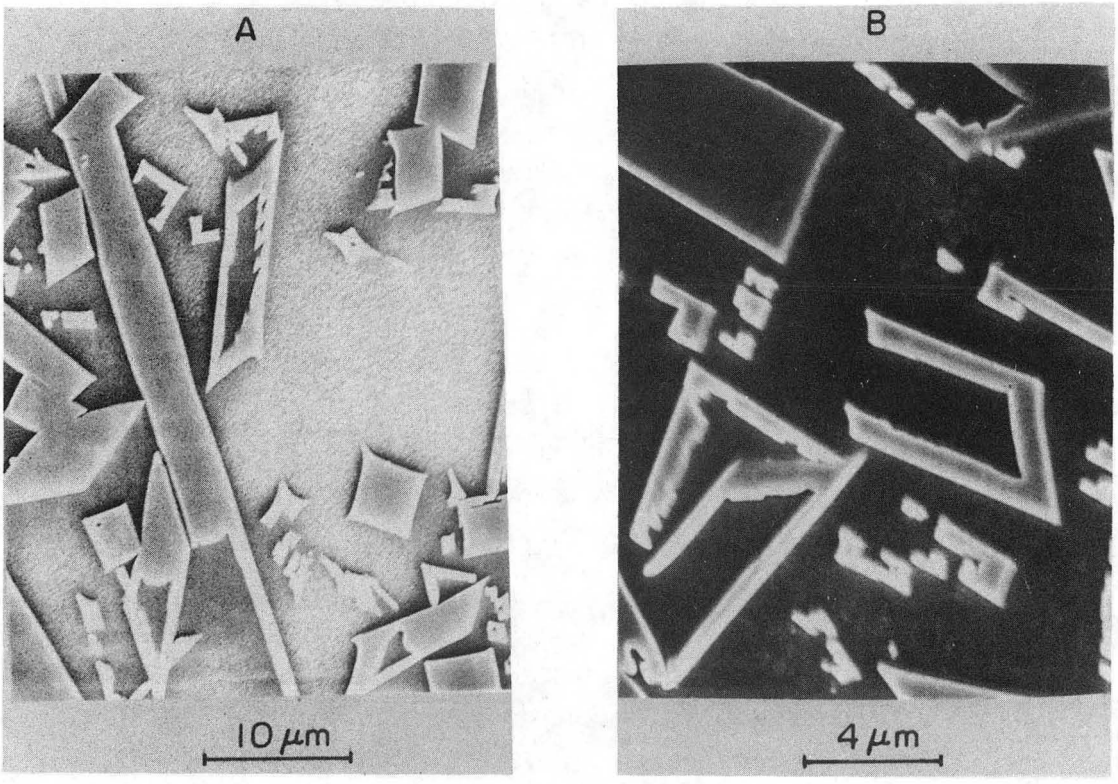

XBB766-5217
Fig. 35

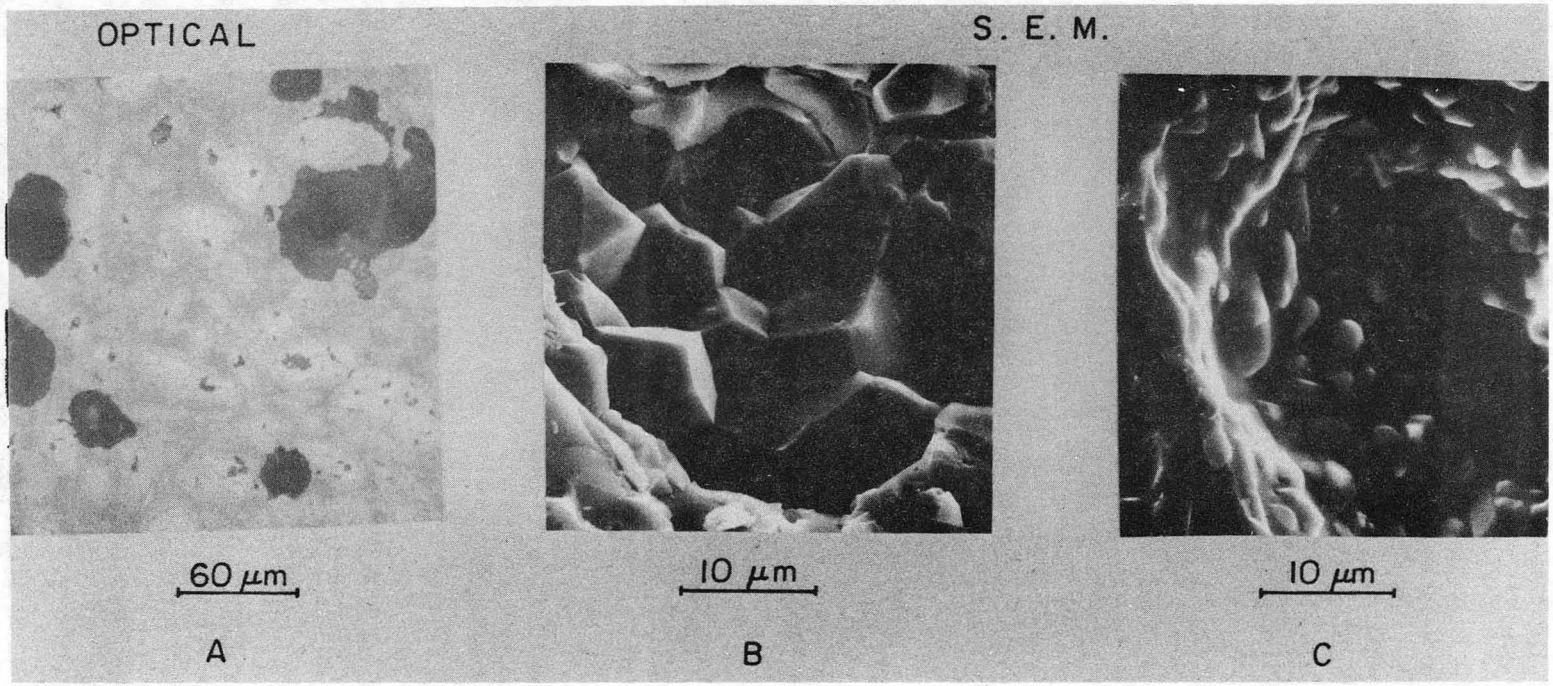

XBB766-5224
Fig. 36

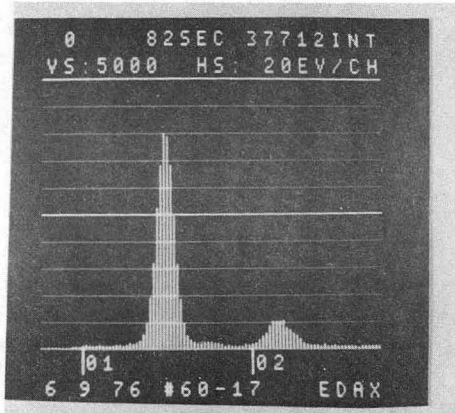

Al_2O_3

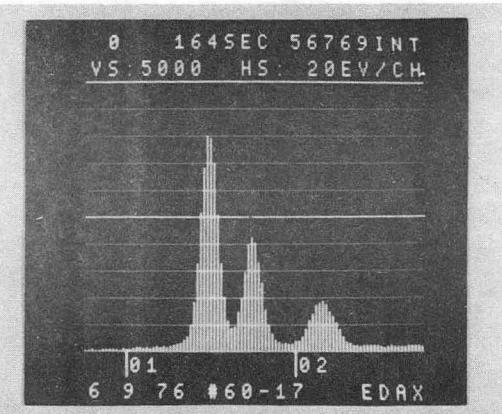

MULLITE
BY SOLID STATE REACTION:
$Al/Si \approx 1.96$

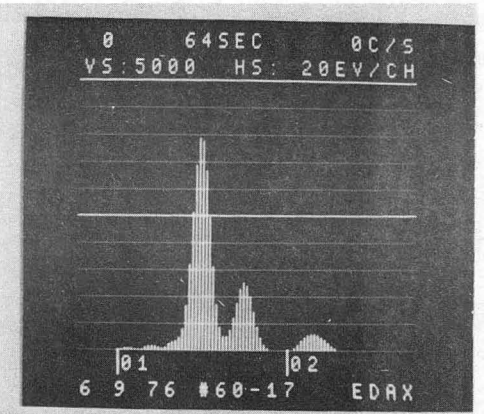

MULLITE
FROM LIQUID PHASE:
$Al/Si \approx 3.08$

XBB766-5223
Fig. 37

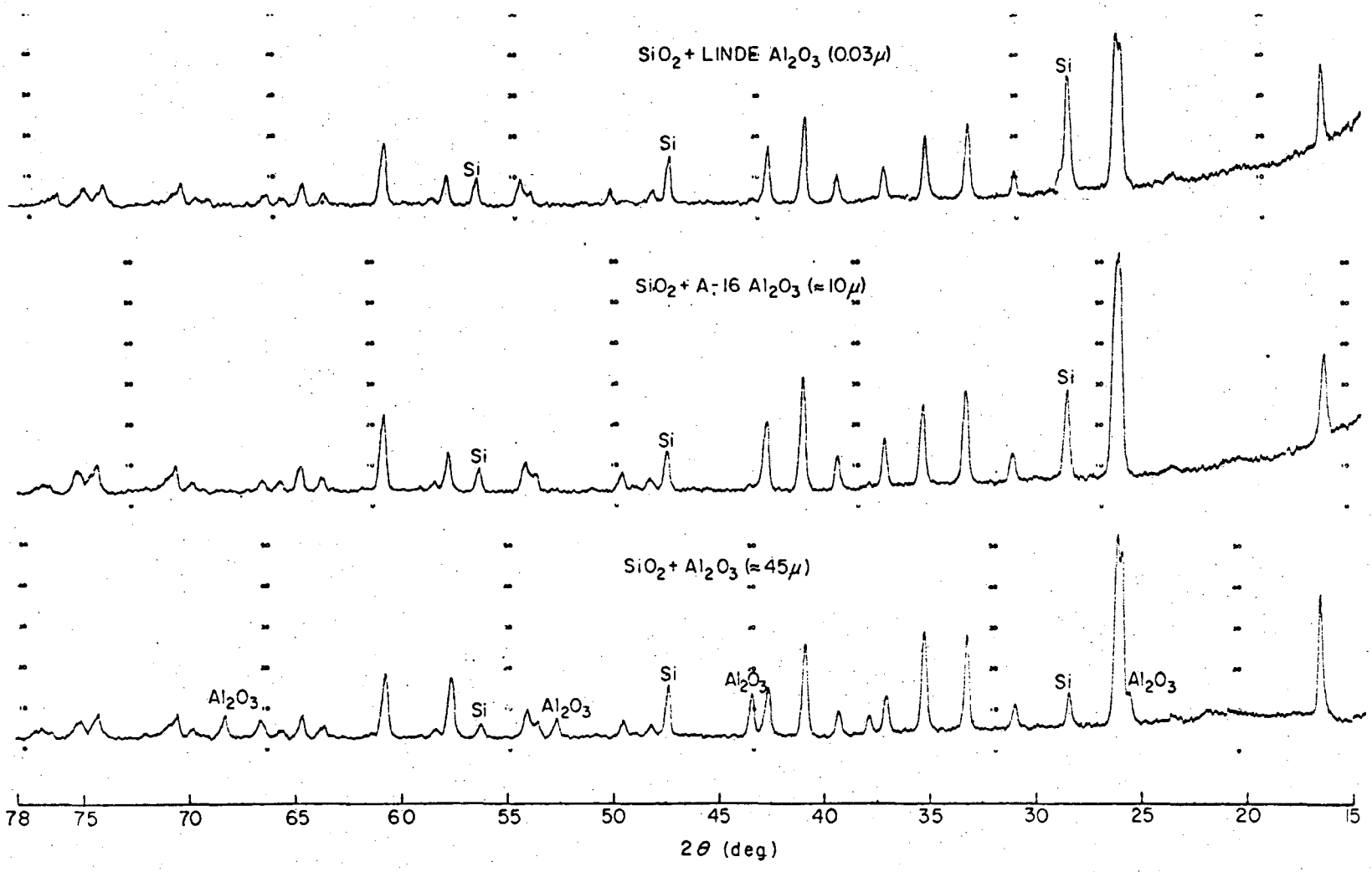

XBL766-7048
Fig. 38

APPENDIX I

Computer Programs for Immiscibility Calculations.

```
      PROGRAM RISBUD(INPUT,OUTPUT)
      DIMENSION TCRIT(20),XMOLE(20),A(10),Q(20,20),QQ(20),TEMP(20)
      DIMENSION SS(20),R(20,20),ACTSIL(100),FENERGY(100),AACTSIL(100)
      DIMENSION S(20,20),IARRAY(112)
      COMMON ISTAR,IBLANK
      READ 17,ISTAR,IBLANK
   17 FORMAT(2A1)
      READ 100,(TCRIT(I),XMOLE(I),I=1,20)
  100 FORMAT(F6.1,F7.4)
      NPTS=20
      NTERMS=4
      PRINT 1
    1 FORMAT(*POLYNOMIAL FIT FOR ACTIVITY COEFF IN THE ALUMINA
     1SILICA SYSTEM*//)
      MODE=-1
      KK=0
      DO 200 I=1,20
      K=0
      P=-4778.36*(1./TCRIT(I)-1./2323.)+1.5038*(ALOG(TCRIT(I)/2323.))
     1-0.0004796*(TCRIT(I)-2323.)+79442.6*(1./TCRIT(I)**2-1./2323.**2)
     1-ALOG(XMOLE(I))/2.303
      PRINT 201,TCRIT(I)
  201 FORMAT(//28HTHE CRITICAL TEMPERATURE IS ,F6.1)
      PRINT 202, XMOLE(I)
  202 FORMAT(//21HTHE MOLE FRACTION IS ,F7.4)
      PRINT 203,P
  203 FORMAT(//55HLOG OF THE CRITICAL ACTIVITY COEFFICIENT OF ALUMINAIS
     1 ,F10.5)
      Z=P+(ALOG(XMOLE(I)))/2.303
      PRINT 204,Z
  204 FORMAT(//43HLOG OF THE CRITICAL ACTIVITY OF ALUMINA IS,F10.5)
      KK=KK+1
      PRINT 205
  205 FORMAT(//*      LOG ACTIVITY COEFFICIENT OF ALUMINA
     1TEMPERATURE     ACTIVITY ALUMINA      PARTIAL HEAT ALUMINA*//)
      DO 300 J=973,2373,100
      K=K+1
      TEMP(K)=J
      Q(K,KK)=TCRIT(I)*P/TEMP(K)
      R(K,KK)=Q(K,KK)+ALOG(ABS(XMOLE(I)))/2.303
      S(K,KK)=10.**R(K,KK)
      PRINT 301,Q(K,KK),TEMP(K),S(K,KK)
  301 FORMAT(33X,F7.5,15X,F6.1,25X,F10.7)
  300 CONTINUE
  200 CONTINUE
      DO 500 K=1,15
      PRINT 888,TEMP(K)
  888 FORMAT(///*THE TEMPERATURE IS *,F6.1//)
      PRINT 399
  399 FORMAT(//*ACTIVITY OF ALUMINA          MOLE FRACTION OF ALUMINA
     1/)
      DO 400 KK=1,20
      PRINT 401,S(K,KK),XMOLE(KK)
  401 FORMAT(13X,F10.7,21X,F10.7)
      SS(KK)=S(K,KK)
      QQ(KK)=Q(K,KK)
```

```
400 CONTINUE
    PRINT 402
402 FORMAT(//*A POLYNOMIAL FIT FOR ACTIVITY OF ALUMINA AS A FUNCTION
   1OF MOLE FRACTION*//)
    CALL POLFIT(XMOLE,SS,SIGMAY,NPTS,NTERMS,MODE,A,CHISQR)
    PRINT 499
499 FORMAT(/*      MOLE FRACTION ALUMINA          ACTIVITY ALUMINA
   1LOG OF THE ACTIVITY OF ALUMINA*//)
    DO 600 I=40,100
    X=I/100.
    ACT=A(1)+A(2)*X+A(3)*X**2.+A(4)*X**3.
    DIVACT=ALOG(ACT)/2.303
    PRINT 601,X,ACT,DIVACT
601 FORMAT(12X,F6.4,16X,F10.7,19X,F12.7)
600 CONTINUE
    PRINT 779
    PRINT 766
766 FORMAT(//*                              ACTIVITY OF ALUMINA*/)
    PRINT 767
767 FORMAT(*         .60                  .70                  .80
   1          .90                 1.00                 1.10*/)
    PRINT 768
768 FORMAT(*         +-------------------+-------------------+---------
   1----------+-------------------+-------------------+----------+*)
    PRINT 769
769 FORMAT(*  XMOLE*)
    DO 700 I=40,100
    H=.60
    G=200.
    GG=120.
    X=I/100.
    ACT=A(1)+A(2)*X+A(3)*X**2.+A(4)*X**3.
    CALL PPLOT(ACT,IARRAY,G,GG,H)
    PRINT 701,X,IARRAY
701 FORMAT(F7.4,1X,112A1)
700 CONTINUE
    PRINT 768
    PRINT 779
779 FORMAT(1H1)
    PRINT 801
801 FORMAT(//*A POLYNOMIAL FIT FOR ACTIVITY COEFFICIENT OF ALUMINA
   1AS A FUNCTION OF MOLE FRACTION *//)
    CALL POLFIT(XMOLE,QQ,SIGMAY,NPTS,NTERMS,MODE,A,CHISQR)
    B=A(2)
    C=A(3)*2.
    D=A(4)*3.
    X40=.40
    Y401=B*((1.-X40)-ALOG(1.-X40))
    Y402=-C*((1.-X40)**2./2.-2.*(1.-X40)+ALOG(1.-X40))
    Y403=D*((1.-X40)**3./3.-1.5*(1.-X40)**2.+3.*(1.-X40)-ALOG(1.-X40))
    SUM=(Y401+Y402+Y403)
    PRINT 899
899 FORMAT(//*MOLE FRACTION ALUMINA       ACTIVITY OF SILICA
   1ADJUSTED FREE ENERGY   PARAMETER B*//)
    DO 900 I=41,99
    X=I/100.
```

```
      Y1=3*((1.-X)-ALOG(1.-X))
      Y2=-C*((1.-X)**2./2.-2.*(1.-X)+ALOG(1.-X))
      Y3=D*((1.-X)**3./3.-1.5*(1.-X)**2.+3.*(1.-X)-ALOG(1.-X))
      GAMASIL=-(Y1+Y2+Y3-SUM)-0.30
      AACTSIL(I)=GAMASIL+ALOG(1.-X)/2.303
      ACTSIL(I)=10.**AACTSIL(I)
      FENERGY(I)=4.575*TEMP(K)*(X*R(K,KK)+(1.-X)*AACTSIL(I))
      BBB=-0.5125*973./TEMP(K)
      AFE=1000.*(FENERGY(I)/(4.575*TEMP(K))+BBB*X-BBB)
      PRINT 901,X,ACTSIL(I),AFE,BBB
  901 FORMAT(14X,F6.4,14X,F10.6,14X,F10.5,10X,F10.5)
  900 CONTINUE
      PRINT 779
      PRINT 902
  902 FORMAT(*                                   ACTIVITY OF SILICA*/)
      PRINT 903
  903 FORMAT(*          .05                    .15                    .25
     1          .35                    .45                    .55*/)
      PRINT 768
      PRINT 769
      DO 905 I=41,99
      TT=10.
      X=I/100.
      T=200.
      ACTSI=ACTSIL(I)
      U=.05
      CALL PPLOT(ACTSI,IARRAY,T,TT,U)
      PRINT 701,X,IARRAY
  905 CONTINUE
      PRINT 779
      PRINT 923
  923 FORMAT(/*MOLE FRACTION ALUMINA                FREE  ENERGY*//)
      DO 924 I=41,99
      X=I/100.
      PRINT 925,X,FENERGY(I)
  925 FORMAT(15X,F6.4,11X,F10.3)
  924 CONTINUE
      PRINT 779
      PRINT 926
  926 FORMAT(/*                                  FREE ENERGY*/)
      PRINT 927
  927 FORMAT(*         0.00                  -700                  -1400
     1       -2100                 -2800                 -3500*/)
      PRINT 768
      PRINT 769
      DO 950 I=41,99
      X=I/100.
      V=1.
      VV=0.
      UU=0.
      FEN=(ABS(FENERGY(I)))/35.
      CALL PPLOT(FEN,IARRAY,V,VV,UU)
      PRINT 701,X,IARRAY
  950 CONTINUE
      PRINT 779
      IF(TEMP(K).GE.1673.) GO TO 7

  500 CONTINUE
    7 CONTINUE
      END
```

```
      SUBROUTINE POLFIT (X,Y,SIGMAY,NPTS,NTERMS,MODE,A,CHISQR)
      DOUBLE PRECISION SUMX, SUMY, XTERM, YTERM, ARRAY, CHISQ
      DIMENSION X(500),Y(500),SIGMAY(1),A(10)
      DIMENSION SUMX(19), SUMY(10), ARRAY(10,10)
C     SUBROUTINE POLFIT
C
C     PURPOSE
C       MAKE A LEAST-SQUARES FIT TO DATA WITH A POLYNOMIAL CURVE
C          Y = A(1) + A(2)*X + A(3)*X**2 + A(4)*X**3 + . . .
C
C     USAGE
C       CALL POLFIT (X, Y, SIGMAY, NPTS, NTERMS, MODE, A, CHISQR)
C
C     DESCRIPTION OF PARAMETERS
C       X      - ARRAY OF DATA POINTS FOR INDEPENDENT VARIABLE
C       Y      - ARRAY OF DATA POINTS FOR DEPENDENT VARIABLE
C       SIGMAY - ARRAY OF STANDARD DEVIATIONS FOR Y DATA POINTS
C       NPTS   - NUMBER OF PAIRS OF DATA POINTS
C       NTERMS - NUMBER OF COEFFICIENTS (DEGREE OF POLYNOMIAL + 1)
C       MODE   - DETERMINES METHOD OF WEIGHTING LEAST-SQUARES FIT
C                +1 (INSTRUMENTAL) WEIGHT(I) = 1./SIGMAY(I)**2
C                 0 (NO WEIGHTING) WEIGHT(I) = 1.
C                -1 (STATISTICAL)  WEIGHT(I) = 1./Y(I)
C       A      - ARRAY OF COEFFICIENTS OF POLYNOMIAL
C       CHISQR - REDUCED CHI SQUARE FOR FIT
C
C     SUBROUTINES AND FUNCTION SUBPROGRAMS REQUIRED
C       DETERM (ARRAY, NORDER)
C          EVALUATES THE DETERMINANT OF A SYMMETRIC TWO-DIMENSIONAL
C          MATRIX OF ORDER NORDER
C
C     MODIFICATIONS FOR FORTRAN II
C       OMIT DOUBLE PRECISION SPECIFICATIONS
C
C     COMMENTS
C       DIMENSION STATEMENT VALID FOR NTERMS UP TO 10
C
C
C        ACCUMULATE WEIGHTED SUMS
C
   11 NMAX = 2*NTERMS - 1
      DO 13 N=1, NMAX
   13 SUMX(N) = 0.
      DO 15 J=1, NTERMS
   15 SUMY(J) = 0.
      CHISQ = 0.
   21 DO 50 I=1, NPTS
      XI = X(I)
      YI = Y(I)
   31 IF (MODE) 32, 37, 39
   32 IF (YI) 35, 37, 33
   33 WEIGHT = 1. / YI
      GO TO 41
   35 WEIGHT = 1. / (-YI)
      GO TO 41
   37 WEIGHT = 1.
```

```
      GO TO 41
   39 WEIGHT = 1. / SIGMAY(I)**2
   41 XTERM=WEIGHT
      DO 44 N=1, NMAX
      SUMX(N) = SUMX(N) + XTERM
   44 XTERM = XTERM * XI
   45 YTERM = WEIGHT*YI
      DO 48 N=1, NTERMS
      SUMY(N) = SUMY(N) + YTERM
   48 YTERM = YTERM * XI
   49 CHISQ = CHISQ + WEIGHT*YI**2
   50 CONTINUE
C
C        CONSTRUCT MATRICES AND CALCULATE COEFFICIENTS
C
   51 DO 54 J=1, NTERMS
      DO 54 K=1, NTERMS
      N = J + K - 1
   54 ARRAY(J,K) = SUMX(N)
      DELTA = DETERM (ARRAY, NTERMS)
      IF (DELTA) 61, 57, 61
   57 CHISQR = 0.
      DO 59 J=1, NTERMS
   59 A(J) = 0.
      GO TO 80
   61 DO 70 L=1, NTERMS
   62 DO 66 J=1, NTERMS
      DO 65 K=1, NTERMS
      N=J+K-1
   65 ARRAY(J,K) = SUMX(N)
   66 ARRAY(J,L) = SUMY(J)
      A(L)=DETERM(ARRAY,NTERMS)/DELTA
      LL=L-1
   70 PRINT 81,LL,A(L)
   81 FORMAT(/17H           DEGREE I2,20H COEFFICIENT OF X = E20.10)
C
C     CALCULATE CHI SQUARE
C
   71 DO 75 J=1,NTERMS
      CHISQ=CHISQ-2.*A(J)*SUMY(J)
      DO 75 K=1,NTERMS
      N=J+K-1
   75 CHISQ=CHISQ+A(J)*A(K)*SUMX(N)
   76 FREE=NPTS-NTERMS
   77 CHISQR=CHISQ/FREE
      PRINT 775,CHISQR,FREE
  775 FORMAT(/23H           CHI SQUARE = E12.6,8H  WITH  F5.0,20H  DEGRE
     1ES OF FREEDOM,////)
   80 RETURN
      END
```

```
      FUNCTION DETERM(ARRAY,NORDER)
      DOUBLE PRECISION ARRAY,SAVE
      DIMENSION ARRAY(10,10)
C     FUNCTION DETERM
C
C     PURPOSE
C       CALCULATE THE DETERMINANT OF A SQUARE MATRIX
C
C     USAGE
C       DET=DETERM(ARRAY,NORDER)
C
C     DESCRIPTION OF PARAMETERS
C       ARRAY  -  MATRIX
C       NORDER  -  ORDER OF DETERMINANT (DEGREE OF MATRIX)
C
C     SUBROUTINES AND FUNCTION SUBPROGRAMS REQUIRED
C       NONE
C
C     COMMENTS
C       THIS PROGRAM DESTROYS THE INPUT MATRIX ARRAY
C       DIMENSION STATEMENT VALED FOR NORDER UP TO 10
C
   10 DETERM=1.
   11 DO 50 K=1,NORDER
C
C        INTERCHANGE COLUMNS IF DIAGONAL ELEMENT IS ZERO
C
      IF(ARRAY(K,K))41,21,41
   21 DO 23 J=K,NORDER
      IF (ARRAY(K,J))31,23,31
   23 CONTINUE
      DETERM=0.
      GO TO 60
   31 DO 34 I=K,NORDER
      SAVE=ARRAY(I,J)
      ARRAY(I,J)=ARRAY(I,K)
   34 ARRAY(I,K)=SAVE
      DETERM=-DETERM
C
C        SUBRRACT ROW K FROM LOWER ROWS TO GET DIAGONAL MATRIX
C
   41 DETERM=DETERM*ARRAY(K,K)
      IF(K-NORDER)43,50,50
   43 K1=K+1
      DO 46 I=K1,NORDER
      DO 46 J=K1,NORDER
   46 ARRAY(I,J)=ARRAY(I,J)-ARRAY(I,K)*ARRAY(K,J)/ARRAY(K,K)
   50 CONTINUE
   60 RETURN
      END
      SUBROUTINE PPLOT(X1,IARRAYS,B,BB,C)
      DIMENSION IARRAYS(112)
      COMMON ISTAR,IBLANK
      DO 1 I=1,112
      IARRAYS(I)=IBLANK
    1 CONTINUE
      IF(X1 .LE. C)GO TO 2
      XX1=X1*B-BB
      IX1=XX1
      IARRAYS(IX1)=ISTAR
    2 CONTINUE
      RETURN
      END
```

APPENDIX II

Computer Programs for Electron Beam Microprobe Analysis.

MICROPROBE ANALYSIS A60-17

20 JAN 76

SUBMITTED BY= SUBBASH H. RISBUD

DESCRIPTION= 60-17R,60-17

MEAN CHEMICAL COMPOSITION AND TWO SIGMA LIMITS BASED ON 151 ANALYSES

ELEMENT	WEIGHT PERCENT	ATOMIC PERCENT
SI	14.17 +- .93	9.44 +- .61
AL	20.15 +- 1.46	14.11 +- 1.08
O *	65.68 +- 1.15	76.45 +- .92

* DETERMINED BY DIFFERENCE

MEAN INTENSITY RATIOS AND TWO SIGMA LIMITS

ELEMENT	K
SI KA	.2514 +- .0188
AL KA	.3568 +- .0270

ACCELERATING VOLTAGE	15.0 KEV
X-RAY EMERGENCE ANGLE	41.0 DEGREES

PEAK-TO-BACKGROUND RATIOS (P/B), SENSITIVITIES (SENS), AND MINIMUM DETECTABILITY LIMITS (MDL)

ELEMENT	P/B	SENS	MDL
SI	1134/1	.05 0/0	36 PPM
AL	1954/1	.07 0/0	30 PPM

XBL 766-8452

MICROPROBE ANALYSIS A60-17

20 JAN 76

ELEMENT	WEIGHT PERCENT	ATOMIC PERCENT	K-RATIO	INTENSITIES UNKN	INTENSITIES STD	BACKGROUNDS UNKN	BACKGROUNDS STD	ITER	OBS
SI KA	11.94	8.51	.1872	7531	40227	86	86		
AL KA	36.68	27.21	.6793	22158	32620	38	38		
O =	51.38	64.28							
								4	1
SI KA	11.89	8.47	.1863	7495	40227	86	86		
AL KA	36.75	27.26	.6806	22202	32620	38	38		
O =	51.36	64.26							
								4	2
SI KA	11.99	8.55	.1881	7565	40227	86	86		
AL KA	36.67	27.21	.6792	22155	32620	38	38		
O =	51.34	64.25							
								4	3
SI KA	12.71	9.04	.2008	8078	40227	86	86		
AL KA	35.56	26.34	.6576	21452	32620	38	38		
O =	51.73	64.62							
								4	4
SI KA	12.46	8.87	.1965	7903	40227	86	86		
AL KA	35.84	26.55	.6630	21627	32620	38	38		
O =	51.70	64.58							
								4	5
SI KA	8.55	6.13	.1298	5222	40227	86	86		
AL KA	41.29	30.79	.7690	25085	32620	38	38		
O =	50.16	63.08							
								4	6
SI KA	10.65	7.61	.1648	6628	40227	86	86		
AL KA	38.57	28.69	.7162	23361	32620	38	38		
O =	50.78	63.70							
								4	7
SI KA	11.93	8.50	.1872	7531	40227	86	86		
AL KA	36.56	27.11	.6768	22079	32620	38	38		
O =	51.50	64.39							
								4	8
SI KA	11.58	8.27	.1805	7260	40227	86	86		
AL KA	37.56	27.93	.6970	22736	32620	38	38		
O =	50.87	63.80							
								4	9
SI KA	11.24	8.02	.1751	7045	40227	86	86		
AL KA	37.57	27.89	.6965	22720	32620	38	38		
O =	51.19	64.09							
								4	10
SI KA	10.42	7.44	.1613	6488	40227	86	86		
AL KA	38.49	28.59	.7140	23291	32620	38	38		
O =	51.08	63.98							
								4	11
SI KA	11.71	8.36	.1828	7352	40227	86	86		
AL KA	37.35	27.77	.6929	22604	32620	38	38		
O =	50.94	63.87							
								4	12
SI KA	12.12	8.64	.1902	7652	40227	86	86		
AL KA	36.58	27.15	.6776	22103	32620	38	38		
O =	51.30	64.21							
								4	13

XBL 766-8468

DOOP

```
      PROGRAM DOOP (INPUT,OUTPUT,TAPE4,TAPE5,TAPE7)                          5
      DIMENSION DENSITY(500), SUM(500), AW(500), BW(500), CW(500)            10
      COMMON Z(500),AWPCT(500),BWPCT(500),CWPCT(500),ACONC(500),BCONC(50     15
     10),CCONC(500),COAP1(500),COAP2(500),AP1(500),WP1(500),AP2(500),WP2     20
     2(500),AP3(500),WP3(500),COAP3(500),ACMP(1),BCMP(1),CCMP(1),ELMA(1)     25
     3,ELMB(1),ELMC(1)                                                       30
      REWIND 4                                                               35
    4 REWIND 5                                                               40
    6 REWIND 7                                                               45
   10 READ 110, ATWTA,ATWTB,ATWTC,STEP,AWTP,BWTP,CWTP,CPLDENS
   34 READ 115, ACMP,BCMP,CCMP,ELMA,ELMB,ELMC                                55
   54 READ (5,120) NX,NA                                                     60
   64 PRINT 120, NX,NA                                                       65
   74 NPT=NX                                                                 70
   76 DO 10 I=1,NPT                                                          75
   77 READ (4,125) WP1(I),AP1(I),OBS                                         80
  112 READ (4,125) WP2(I),AP2(I),OBS                                         85
  126 IF (NA.EQ.3) 5,10                                                      90
  132  5 READ (4,125) WP3(I),AP3(I),OBS                                      95
  146 10 CONTINUE                                                           100
  151    IF (STEP.LT.1.0) 15,20                                             105
  155 15 READ 130, (Z(I),I=1,NPT)                                           110
  164    GO TO 30                                                           115
  165 20 DO 25 I=1,NPT                                                      120
  174    Z(I)=(FLOAT(I)-1.)*STEP                                            125
  176 25 CONTINUE                                                           130
  177 30 GO TO (35,35,45),NA                                                135
  206 35 DO 40 I=1,NPT                                                      140
  216    AW(I)=AP1(I)*ATWTA                                                 145
  217    BW(I)=AP2(I)*ATWTB                                                 150
  221    SUM(I)=AW(I)+BW(I)                                                 155
  222    BWPCT(I)=(BW(I)/SUM(I))*100.                                       160
  224    AWPCT(I)=(AW(I)/SUM(I))*100.                                       165
  225 40 CONTINUE                                                           170
  227    GO TO 55                                                           175
  227 45 DO 50 I=1,NPT                                                      180
  237    AW(I)=AP1(I)*ATWTA                                                 185
  240    BW(I)=AP2(I)*ATWTB                                                 190
  242    CW(I)=AP3(I)*ATWTC                                                 195
  244    SUM(I)=AW(I)+BW(I)+CW(I)                                           200
  246    AWPCT(I)=(AW(I)/SUM(I))*100.                                       205
  250    BWPCT(I)=(BW(I)/SUM(I))*100.                                       210
  251    CWPCT(I)=(CW(I)/SUM(I))*100.                                       215
  253 50 CONTINUE                                                           220
  255 55 DO 85 I=1,NPT                                                      225
  257    IF (BWPCT(I)-80.0) 60,65,65                                        230
  262 60 DENSITY(I)=.00806*BWPCT(I)+CPLDENS                                 235
  266    GO TO 75                                                           240
  266 65 IF (BWPCT(I)-130.0) 70,85,85                                       245
  271 70 DENSITY(I)=3.965                                                   250
  274 75 COAP1(I)=(DENSITY(I)*AWPCT(I))/100.                                255
  277    COAP2(I)=(DENSITY(I)*BWPCT(I))/100.                                260
  301    GO TO (85,85,80),NA                                                265
  310 80 COAP3(I)=(DENSITY(I)*CWPCT(I))/100.                                270
  314 85 CONTINUE                                                           275
  317    PRINT 135, ACMP,BCMP,CCMP,ACMP,BCMP,CCMP,ELMA,ELMB,ELMC            280
```

XBL 766-8447

```
DOOPY
                PROGRAM DOOPY (INPUT,OUTPUT,TAPE5,TAPE7,TAPE98,TAPE99)                    5
                DIMENSION Z(500), ACONC(500), BCONC(500), CCONC(500), IBCD(10)           10
                COMMON NO,ELMTA(1),ELMTB(1),ELMTC(1),NPLT,XMX,YMX                        20
                REWIND 5                                                                 25
          9     REWIND 7                                                                 30
          6     READ (5,40) NX,NA                                                        35
         16     NO=NX                                                                    40
         20     READ 45, SAMPLE,NPLOT,ELMTA,ELMTB,ELMT,XMX,YMX                           45
         41     ENCODE (30,50,IBCD) SAMPLE                                               50
         51     IBCD(10)=0                                                               55
         52     GO TO (5,5,10),NA                                                        60
         61   5 READ (7,55) (Z(I),ACONC(I),BCONC(I),I=1,NO)                              65
        103     GO TO 15                                                                 70
        104    10 READ (7,60) (Z(I),ACONC(I),BCONC(I),CCONC(I),I=1,NO)                   75
        131    15 CONTINUE                                                               80
        131     GO TO (20,25,30),NPLOT                                                   85
        140    20 CALL GRAPH (Z,BCONC,ACONC,NO,IBCD,7HMICRONS,16HCONCENTRATION AL)       90
        147     GO TO 35                                                                 95
        150    25 CALL GRAPH (Z,ACONC,BCONC,NO,IBCD,7HMICRONS,16HCONCENTRATION SI)      100
        157     CALL GRAPH (Z,BCONC,ACONC,NO,IBCD,7HMICRONS,16HCONCENTRATION AL)        105
        166     GO TO 35                                                                110
        167    30 CALL GRAPH (Z,ACONC,BCONC,NO,IBCD,7HMICRONS,16HCONCENTRATION SI)      115
        176     CALL GRAPH (Z,BCONC,ACONC,NO,IBCD,7HMICRONS,16HCONCENTRATION AL)        120
        205     CALL GRAPH (Z,CCONC,BCONC,NO,IBCD,7HMICRONS,16HCONCENTRATION CA)        125
        219    35 CALL CCEND                                                            130
        215     STOP                                                                    135
              C                                                                         140
             40 FORMAT (213)                                                            145
             45 FORMAT (1A10,15,3(A2),1X,F8.3,2X,F8.3)                                  150
             50 FORMAT (11HSAMPLE NO. ,1A10)                                            155
             55 FORMAT (3F10.5)                                                         160
             60 FORMAT (4F10.5)                                                         165
        217     END                                                                     170-


PROGRAM LENGTH INCLUDING I/O BUFFERS

07930

STATEMENT FUNCTION REFERENCES

        LOCATION  GEN TAG   SYM TAG   REFERENCES

STATEMENT NUMBER REFERENCES

        LOCATION  GEN TAG   SYM TAG   REFERENCES
        000062    L00029    5         000057    000060
        000105    L00032    10        000061
        000132    L00037    15        000104
        000141    L00041    20        000136
        000151    L00044    25        000137
        000170    L00051    30        000140
        000215    L00057    35        000150    000167
        000264    C00042    40        000007
        000266    C00044    45        000020
```

XBL 766-8443

```
CCLBL
                SUBROUTINE CCLBL (NX1,NY1)                                      LBL   5
                COMMON /CCPOOL/ XMIN,XMAX,YMIN,YMAX,CCXMIN,CCXMAX,CCYMIN,CCYMAX LBL  10
                COMMON /CCFACT/ FACTOR                                          LBL  15
                ISZERO=0                                                        LBL  20
      4         XD=XMAX-XMIN                                                    LBL  25
      6         YD=YMAX-YMIN                                                    LBL  30
     10         CCXD=CCXMAX-CCXMIN                                              LBL  35
     12         CCYD=CCYMAX-CCYMIN                                              LBL  40
     14         XI=XD/FLOAT(NX1)                                                LBL  45
     16         YI=YD/FLOAT(NY1)                                                LBL  50
     20         KSIZE=2                                                         LBL  55
     21         KORIENT=0                                                       LBL  60
          C     LABEL FROM RIGHT TO LEFT ALONG THE X-AXIS.                      LBL  65
     23         DO 5 NX=ISZERO,NX1                                              LBL  70
     25         CCX=CCXMAX-CCXD*FLOAT(NX)/FLOAT(NX1)                            LBL  75
     31         X=(CCX-CCXMIN)*XD/CCXD+XMIN                                     LBL  80
          C     SET X TO A TRUE ZERO IF X=0. TO WITHIN MACHINE ACCURACY.        LBL  85
     35         IF (ABS(X/XI).LT.1.0E-6) X=0.                                   LBL  90
     42         WRITE (98,15) X                                                 LBL  95
     52       5 CALL CCLTR (CCX-49.2*FLOAT(KSIZE)/FACTOR,CCYMIN-10.*FLOAT(KSIZE)/FLBL 100
               1ACTOR,KORIENT,KSIZE)                                            LBL 105
     70         KSIZE=2                                                         LBL 110
     70         KORIENT=0                                                       LBL 115
          C     LABEL UPWARD ALONG THE Y-AXIS.                                  LBL 120
     72         DO 10 NY=ISZERO,NY1                                             LBL 125
     74         CCY=CCYMIN+CCYD*FLOAT(NY)/FLOAT(NY1)                            LBL 130
    100         Y=(CCY-CCYMIN)*YD/CCYD+YMIN                                     LBL 135
          C     SET Y TO A TRUE ZERO IF Y=0. TO WITHIN MACHINE ACCURACY.        LBL 140
    103         IF (ABS(Y/YI).LT.1.0E-6) Y=0.                                   LBL 145
    111         WRITE (98,20) Y                                                 LBL 150
    121        10 CALL CCLTR (CCXMIN-70.*FLOAT(KSIZE)/FACTOR,CCY,KORIENT,KSIZE) LBL 155
    139         RETURN                                                          LBL 160
          C                                                                     LBL 165
             15 FORMAT (F10.1)                                                  LBL 170
             20 FORMAT (F10.3)                                                  LBL 175
    134         END                                                             LBL 180-


SUBPROGRAM LENGTH

00206

STATEMENT FUNCTION REFERENCES

         LOCATION  GEN TAG   SYM TAG   REFERENCES

STATEMENT NUMBER REFERENCES

         LOCATION  GEN TAG   SYM TAG   REFERENCES
         000145    C00006    15        000043
         000147    C00010    20        000112

BLOCK NAMES AND LENGTHS
CCPOOL - 000010/01  CCFACT - 000001/02
```

XBL 766-8439

GRAPH

```
                SUBROUTINE GRAPH (X,Y,Z,N,RG,RX,RY)                                    GPH   5
                COMMON /CCPOOL/ XMIN,XMAX,YMIN,YMAX,CCXMIN,CCXMAX,CCYMIN,CCYMAX        GPH  10
                COMMON NO,ELMTA(1),ELMTB(1),ELMTC(1),NPLT,XMX,YMX                      GPH  15
                DIMENSION ROUND(9), X(1), Y(1), Z(1)                                   GPH  20
                DIMENSION YSC(2)                                                       GPH  25
                DATA (ROUND(I),I=1,9)/1.,2.,2.5,5./                                    GPH  30
                DATA NROUND,PART/4,10./                                                GPH  35
                YSC(1)=Y(1)                                                            GPH  40
      12        YSC(2)=Z(1)                                                            GPH  45
      13        DO 5 I=1,N                                                             GPH  50
      15        IF (Y(I).GT.YSC(1)) YSC(1)=Y(I)                                        GPH  55
      21        IF (Z(I).GT.YSC(1)) YSC(1)=Z(I)                                        GPH  60
      25        IF (Y(I).LT.YSC(2)) YSC(2)=Y(I)                                        GPH  65
      31        IF (Z(I).LT.YSC(2)) YSC(2)=Z(I)                                        GPH  70
      35      5 CONTINUE                                                               GPH  75
      90        CCXMIN=100.                                                            GPH  80
      91        CCXMAX=2600.                                                           GPH  85
      92        CCYMIN=150.                                                            GPH  90
      94        CCYMAX=1000.                                                           GPH  95
      96        WRITE (99,25)                                                          GPH 100
      51        XMIN=0.0                                                               GPH 105
      52        IF (Z(NO)-500.) 10,10,15                                               GPH 110
      61     10 XMAX=XMX                                                               GPH 115
      63        GO TO 20                                                               GPH 120
      63     15 XMAX=Z(NO)+100.                                                        GPH 125
      66     20 YMIN=0.                                                                GPH 130
      67        YMAX=YMX                                                               GPH 135
      71        CALL CCGRID (1,IFIX(PART),6HNOLBLS,1,IFIX(PART))                       GPH 140
      76        CALL CCLBL (IFIX(PART),IFIX(PART))                                     GPH 145
     102        CALL CCLTR (110.,50.,0,3,RG,22)                                        GPH 150
     111        CALL CCLTR (1450.,50.,0,3,RX,7)                                        GPH 155
     121        CALL CCLTR (130.,400.,1,3,RY,16)                                       GPH 160
     126        CALL CCPLOT (X,Y,N,4HJOIN,1,1)                                         GPH 165
     135        CALL CCNEXT                                                            GPH 170
     136        RETURN                                                                 GPH 175
           C                                                                           GPH 180
          25 FORMAT (*+PLEASE POSITION PEN*/1H*)                                       GPH 185
     137        END                                                                    GPH 190-
```

SUBPROGRAM LENGTH

00214

STATEMENT FUNCTION REFERENCES

LOCATION	GEN TAG	SYM TAG	REFERENCES

STATEMENT NUMBER REFERENCES

LOCATION	GEN TAG	SYM TAG	REFERENCES
000036	L00034	5	000034
000062	L00047	10	000061
000069	L00051	15	000061
000067	L00052	20	000063

APPENDIX III

Computer Programs for X-ray Lattice Parameter Measurements

```
LCLSC
      PROGRAM LCLSC(INPUT,OUTPUT,TAPE2=INPUT,TAPE3=OUTPUT)                MAIN  10
C                          LCLSC (MARK IV)                               MAIN  20
C     CRYSTALLOGRAPHIC LATTICE CONSTANT LEAST-SQUARES REFINEMENT PROGRAMMAIN  30

 SAMPLE 600,PISSUD

INPUT DATA

   H   K   L   LAMBDA  OBSERVATION  THETA(OBS)     D(OBS)      Q(OBS)      SIGMA(Q)
   4   2   2     1        99.274       44.462      1.09967     .82694      1.68523
   8   4   0     1       130.497       65.248       .84817    1.39006      1.28174
   7   6   0     1       137.797       68.998       .82561    1.46706      1.13227

 CONTROL CARD
   3   0   0   0   0   1   0   0   0   0   0   0   0   0   0   0   0

 INITIAL DIRECT LATTICE CONSTANTS
        A =   7.56149          ALPHA =  90.00000
        B =   7.68746           BETA =  90.00000
        C =   2.89409          GAMMA =  90.00000

 INITIAL DIRECT LATTICE CONSTANTS
        A =    .13225          ALPHA =  90.00000
        B =    .13008           BETA =  90.00000
        C =    .34553          GAMMA =  90.00000

 WAVE LENGTHS
     1    1.54050

 SAMPLE 600,PISSUD

OBSERVED AND CALCULATED INTERPLANAR SPACINGS, D, BASED ON INPUT PARAMETERS TO CYCLE 1

                                                  RESIDUALS OF D              RESIDUALS OF Q
   H   K   L      D(OBS)      D(CALC)      (OBS-CALC)  (OBS-CALC)/SIGMA  (OBS-CALC)  (OBS-CALC)/SIGMA
   4   2   2     1.09967     1.10090       -.00123       -.00110          .00185        .00110
   8   4   0      .84817      .84816        .00001        .00002         -.00003       -.00002
   7   6   0      .82561      .82586       -.00025       -.00079          .00089        .00079

 SAMPLE 600,PISSUD

DISCREPANCY FACTORS BASED ON INPUT PARAMETERS TO CYCLE 1

 NUMBER OF OBSERVATIONS (M) =   3
 NUMBER OF VARIED PARAMETERS (N) =   1

 FACTORS FOR D
    SUM (W*(OBS-CALC)**2) = 1.827346E-06
    SQRT(SUM(W*(OBS-CALC)**2)/M-N) = 9.559626E-04

 FACTORS FOR Q
    SUM (W*(OBS-CALC)**2) = 1.827346E-06
    SQRT(SUM(W*(OBS-CALC)**2)/M-N) = 9.546565E-04
```

SAMPLE 600.PISBUD

OBSERVED AND CALCULATED INTERPLANAR SPACINGS, D, BASED ON REFINED PARAMETERS AFTER CYCLE 9

H	K	L	D(OBS)	D(CALC)	RESIDUALS OF D (OBS-CALC)	(OBS-CALC)/SIGMA	RESIDUALS OF Q (OBS-CALC)	(OBS-CALC)/SIGMA
4	2	2	1.09967	1.09967	-.00000	-.00000	.00000	.00000
8	4	0	.84817	.84794	.00023	.00059	-.00075	-.00059
7	6	0	.82561	.82566	-.00005	-.00016	.00018	.00016

DISCREPANCY FACTORS BASED ON REFINED PARAMETERS AFTER CYCLE 9

NUMBER OF OBSERVATIONS (M) = 3
NUMBER OF VARIED PARAMETERS (N) = 0

FACTORS FOR D
SUM (W*(OBS-CALC)**2) = 3.71001E-07
SQRT(SUM(W*(OBS-CALC)**2)/M-N) = 3.51663E-04

FACTORS FOR Q
SUM (W*(OBS-CALC)**2) = 3.71279E-07
SQRT(SUM(W*(OBS-CALC)**2)/M-N) = 3.51795E-04

DIRECT LATTICE CONSTANTS AFTER LEAST-SQUARES CYCLE 9

PARAMETER	OLD	CHANGE	NEW	ERROR
A (ANG.)	7.55938		7.55938	
B (ANG.)	7.68598		7.68598	
C (ANG.)	2.88906	.00000	2.88906	.00219
ALPHA (DEG.)	90.00000		90.00000	
BETA (DEG.)	90.00000		90.00000	
GAMMA (DEG.)	90.00000		90.00000	
UNIT CELL VOLUME (CUBIC ANG.)	167.8577	.0000	167.8577	.1272

DIRECT LATTICE CONSTANT VARIANCE-COVARIANCE MATRIX

	A(ANG.)	B(ANG.)	C(ANG.)	ALPHA(RAD.)	BETA(RAD.)	GAMMA(RAD.)
A	0.	0.	0.	0.	0.	0.
B		0.	0.	0.	0.	0.
C			4.7901111E-06	0.	0.	0.
ALPHA				0.	0.	0.
BETA					0.	0.
GAMMA						0.

DIRECT LATTICE CONSTANT CORRELATION MATRIX

	A	B	C	ALPHA	BETA	GAMMA
A	1.000000	0.000000	0.000000	0.000000	0.000000	0.000000
B		1.000000	0.000000	0.000000	0.000000	0.000000
C			1.000000	0.000000	0.000000	0.000000
ALPHA				1.000000	0.000000	0.000000
BETA					1.000000	0.000000
GAMMA						1.000000

PARAMETER SHIFTS, LEAST-SQUARES CYCLE 9

PARAMETER	OLD	CHANGE	NEW	ERROR
A *	.132286		.132286	
B *	.130107		.130107	
C *	.346134	-.000000	.346134	.000262
ALPHA *	90.00000		90.00000	
BETA *	90.00000		90.00000	
GAMMA *	90.00000		90.00000	

ESTIMATED STANDARD ERROR OF UNIT WEIGHT OBSERVATION OF 0, BASED ON REFINEMENT OF 1 PARAMETERS
SQRT(SUM(W*(OBS-CALC)**2)/M-N) = .00043

APPENDIX IV

X-ray Parameters of Mullite

Sample I.D.*	a(Å)	b(Å)	c(Å)	Cell Volume (a x b x c)
60-Q	7.5606	7.6867	2.8902	167.971
60-18	7.5320	7.7340	2.8930	168.5
60-17	7.5591	7.6854	2-8911	167.958
60-15	7.5730	7.6780	2.903	168.8
60-13	7.5550	7.6883	2.8870	167.692
60-12	7.5612	7.6890	2.8880	167.890
60-10	7.5581	7.6880	2.8894	167.894
60-9	7.5594	7.6860	2.8891	167.858
60-7	7.5765	7.7042	2.8814	168.188
60-6	7.5609	7.6871	2.8901	167.977
42-Q	7.5702	7.7071	2.8879	168.493
42QR-1	7.5628	7.6852	2.8872	167.808
42QR-5	7.5618	7.6846	2.8870	167.762
42QR-18	7.5591	7.6872	2.8857	167.682
4RQR-110	7.5592	7.6885	2.8838	167.605

*See Tables VII and IX.

TECHNICAL INFORMATION DIVISION
LAWRENCE BERKELEY LABORATORY
UNIVERSITY OF CALIFORNIA
BERKELEY, CALIFORNIA 94720